High-throughput experiments for process design of additively manufactured materials

By

Ankur Kumar Agrawal

A dissertation submitted for partial fulfillment

of the requirement for the degree of

Doctor of Philosophy

(Materials Science and Engineering)

at the

UNIVERSITY OF WISCONSIN-MADISON

2022

Date of Final oral examination: 12/12/2022

The dissertation is approved by the following members of the Final Oral Committee:
Dan Thoma, Professor, Material Science and Engineering
John Perepezko, Professor, Material Science and Engineering
Sindo Kou, Professor, Material Science and Engineering
Kumar Sridharan, Professor, Engineering Physics
Lianyi Chen, Assistant Professor, Mechanical Engineering

Acknowledgements

I am very grateful to the University of Wisconsin-Madison for granting me the opportunity to explore scientific research in the USA. UW-Madison offered an encouraging, supportive, and collaborative research environment that provided continuous learning opportunities. During my life in grad school, I met and interacted with many extraordinary people who helped in growing personally and professionally.

First of all, I would like to express my sincere gratitude to my advisor Prof. Dan Thoma for his extended support and guidance. Dan is the most humble, open-minded, and nicest person I have worked with, so far. He was always there to discuss the results or problems I had and gave useful suggestions. He was open to listening to my ideas and trusted my instincts. He remained extremely patient and had a quick turnaround time with my paper revisions, presentation edits, or answering queries over emails. His remarks like "nice work", "it's okay", and "let's figure it out" has boosted my confidence and kept me progressing during a tough time. With him, I learned how to remain calm, think positively, focus on priorities without panicking, and enjoy research. Thanks to Dan, I got opportunities to travel to conferences, present my research findings to a wider audience, and build a professional network. I will always be thankful to Dan for his constant support, for believing in me, for mentoring me, and for giving me these important lessons to become a successful leader.

I am very thankful to my PhD committee members: Prof. John Perepezko, Prof. Sindo Kou, Prof. Kumar Sridharan, and Prof. Lianyi Chen for their guidance throughout the process. Their expertise and experience brought new facets to the discussions. They gave invaluable feedback, suggestions, and critiques useful for the success of the thesis. Their class lectures, books, and study materials were stimulating and helped me broaden my knowledge.

I also had the privilege to collaborate and work with wonderful people at other research groups and organizations. My special thanks to Prof. Frank Pfefferkorn and Prof. Jiamian Hu at the University of Wisconsin-Madison, Dr. Saryu Fensin at Los Alamos National Laboratory, Prof. Jason Hattrick-Simpers at the University of Toronto, and Prof. Lin Shao at the University of Texas A&M. I also thank my previous supervisors and mentors who helped me make a career choice and supported throughout my professional career.

I would like to thank the current and past members of the Alloy Design and Development (ADD) laboratory. Dr. Gabriel Meric de Bellefon and Dr. Kaila Bertsch gave me training on various equipment and helped me get started during the initial stages of my thesis. Dr. Phalgun Nelaturu, Dr. Zahabul Islam, Dr. Behzad Rankouhi, and Mythili Thevamaran probably were the first person I talked to when I need help setting up new experiments, troubleshooting a problem, or simply bouncing off ideas. I also thank Alec Mangan, Michael Niezgoda, Janine Spethson,

Michael Moorehead, Subodh Subedi, Patrick Faue, Caleb Hatler, William Kunkel, and undergraduate students with whom I have worked on a daily basis. They all help me become a better teammate and made my PhD journey smooth and fun.

I thank my friends and colleagues in the department. I will miss the time we spend solving group homework assignments, debating international politics, and discussing food and culture. I thank my friends and members of the IGSA Indian student community, BRIDGE international student society, and the Badminton club for making my grad school life fun and memorable. My long list of friends- Rahul, Sid, Shruthi, Aishwariya, Vrishank, Deepankar, Abitha, Hemant, Mohan, Saket, Dipul, Sabari, Srinath, Kunal, Anjali, Komal, Tej, Sourabh, Ashrit, Arko, Shalini, Shivangi, Kriti, Chetan, Gayatri, Soundarya, Utkarsh, Disesh, Rajeev, Dawn, Anna, Daniel, Eric, Greta, Matt, Kristina, Ruiting, Rachel, Alkheder, Hamoud, and Irena for the random discussion, instant plans, and shared life experiences. I will cherish the memories forever.

Last but not the least, I could not have completed my thesis without the encouragement and support of my family. My father Late Mr. Vijay Agrawal led a life of simple living and high thinking. He supported all the decisions I made throughout my career and was my biggest cheerleader. My mother Mrs. Sarita Agrawal is a wise and strong lady. Her unconditional love and calm nature inspire me to become a better person. My brothers and sisters with whom I spend a wonderful time growing up. My little nephew and niece whose happy faces destress me in minutes.

Table of Contents

List of Figures

List of Tables

Nomenclatures

α	Laser absorptivity
A	Melt pool cross sectional area
β	Coefficient of linear expansion
C_p	Specific heat
d	Melt pool depth
d_l	Laser spot diameter
D_t	Thermal diffusivity
ϵ	Cooling rate
ϵ_t	Thermal strain
E	Elastic modulus
$\overline{E}$	Material toughness near the solidus temperature
E_{dim}	Dimensionless energy density
f_s	Solid fraction of semi-solid region
Fo	Fourier number
G	Thermal gradient
H	Hatch spacing
ΔH	Latent heat
I	Moment of inertia
J	Vaporization flux
K	Thermal conductivity
Ke	Keyhole number
λ	Evaporation energy per atom
λ_{PDAS}	Primary dendritic arm spacing
l	Melt pool length
L	Layer thickness
L_c	Characteristic length
Δm	Material vaporized
m_{dry}	Dry mass of the sample
m_{wet}	Mass of the sample when freely suspended in the fluid
M	Molecular weight
π_1	Dimensionless number 1

π_2	Dimensionless number 2
P	Laser power
P_s	Saturated vapor pressure
P^*	Chamber pressure
P_r	Recoil pressure
Pe	Peclet number
ρ	Density
ρ_{rel}	Relative density
ρ_{sample}	Density of the sample
ρ_{fluid}	Density of the fluid
r_l	Laser spot radius
R	Solidification rate/Molar gas constant/Melt pool aspect ratio
R_a	Average arithmetic height
σ_y	Yield strength
S_a	Average surface roughness
s_f	Shrinkage factor
τ	Characteristic time
T_m	Melting temperature
T_b	Boiling temperature
T_o	Build plate temperature
ΔT	Difference between peak and melting temperature
$T_{surface}$	Surface temperature
$T_{solidus}$	Solidus temperature
$T_{liquidus}$	Liquidous temperature
U_{max}	Maximum velocity of molten metal
V	Scanning speed
w	Melt pool width
X	Mole fraction

Abbreviations

AM	Additive manufacturing
DIC	Data image correlation
EBSD	Electron backscattered diffraction
HRA	Rockwell hardness scale A
HT	High throughput
IPF	Inverse pole figure
LOF	Lack of fusion
LPBF	Laser powder bed fusion
LT	Low throughput
OM	Optical microscope
PDAS	Primary dendritic arm spacing
PV maps	Laser power-scanning speed processing maps
SDAS	Secondary dendritic arm spacing
SEM	Scanning electron microscope
TEM	Transmission electron microscope
VED	Volumetric energy density

Abstract

One of the main challenges in the laser powder bed fusion (LPBF) process is to make dense and defect-free components. In the LPBF process, there are at least 100 independently controlled processing parameters that affect the laser-metal interaction. Selecting the adapted variables for a given material and application can be a challenging and time-consuming task. The goal of this work is to develop a high-throughput (HT) approach to rapidly identify and predict the LPBF processing window and improve the part's printability.

The HT approach included the fabrication of hundreds of hex nut-shaped specimens, each processed with a unique combination of processing variables. An easily removable scaffolding permitted rapid sample extraction from the base plate, thus saving machining costs and time. HT characterization provided the quantitative value of relative density and hardness with a total time estimation of 22 hrs. Both relative density and hardness showed a strong correlation with the processing parameters. HT approach helped in identifying lack-of-fusion offsets and keyholing thresholds for multiple materials like 316l stainless steel, Inconel 718, Haynes 282, cantor alloys, aluminum alloys, copper, and refractory metals. Based on the gathered experimental data points and literature values, a universal dimensionless number (π) is developed. This number is a function of processing parameters and materials properties and can be applied to predict the LPBF processing window.

The fraction of porosity defects critically depends upon the melt pool geometry and interlayer bonding. In chapter 3, an HT surface characterization is presented to examine the melt pool tracks and gain insights into different processing regimes. The variation in the surface roughness provided a direct correlation with the internal porosity defects. The lack-of-fusion

regime relates to high surface roughness ($S_a > 5$ µm), low dimensionless number ($\pi < 61$), and the presence of cavities in between the melt pool tracks. The balling regime correlates to high surface roughness ($S_a > 5$ µm), intermediate dimensionless number ($61 < \pi < 146$), and non-uniform melt pool track width. The keyhole regime shows low surface roughness ($S_a < 5$ µm), high dimensionless number ($\pi > 146$), and a curved melt pool track. The impact of the defects on the as-processed tensile mechanical properties demonstrates that samples with porosity exhibit up to 10% less tensile strength and 30% less ductility than optimal samples.

Power-velocity (PV) processing maps can aid in visualizing the effects of LPBF processing variables and different processing regimes. In chapter 4, an assessment of existing analytical equations and models was used to generate predictive processing maps. The melt pool equations combined with the defect criterion provided a quick approximation of processing regimes for a variety of materials. The time estimation for generating a predictive map based on analytical solutions is less than 5 mins. This work provides a boundary framework for designing the optimal processing parameters for new metals and alloys based on existing analytical solutions.

Finally, a low-throughput (LT) microstructural characterization was performed within the defined processing window. The microstructural analysis included quantification at various length scales (i.e., grains size and morphology, texture, primary dendrite arm spacing, and melt pool geometry). As the energy density increased, coarser grains with higher grain aspect ratios were observed. A model is proposed to explain the dependence of microstructure on the melt pool geometry. Dynamic failure response showed the sample an improved spall strength of up to 40% when processed in the middle of the processing window.

Chapter 1: Introduction

This chapter provides background and introductory concepts of additive manufacturing, the laser powder bed fusion process, key input processing parameters, process-induced porosity defects, power-velocity-based processing maps, and hierarchical microstructures in additively manufactured materials. It discusses the state-of-the-art and the limitations of the current practice. Finally, the primary goals and research objectives of the current study are defined.

1.1 Additive Manufacturing and Laser Powder Bed Fusion

Additive manufacturing (AM), also known as 3D printing, is a disruptive technology that offers a constraint-free design space to fabricate complex geometries in a single processing step. In this process, materials are deposited in a layer-by-layer manner to form a 3D component. Compared to traditional manufacturing routes, AM techniques help in reducing material wastage, reducing total parts needed, lowering the components cost, shortening the time to market, enabling small batch production, and rapid prototyping [1–3]. Examples of metal powder AM techniques include laser powder bed fusion (LPBF), directed energy deposition (DED), wire arc additive manufacturing (WAAM), and electron beam melting (EBM) [4–7]. The principle behind these processes is to introduce material in the powder or wire form and melt them using a high-energy heating source such as a laser or electron beam. AM techniques have been successfully applied to design lattice structures for component weight reductions, gyroid structures in heat exchangers for higher surface area, internal cooling channels of turbine blades for improved heat extraction, and tailored compositions in multi-material components for improved part performance [2,8].

Laser powder bed fusion (LPBF), also known as selective laser melting (SLM), is a widely adopted metal AM technique. A detailed explanation of the process can be found elsewhere [2,4]. Over the past decade, LPBF has gained high interest, especially among the energy, defense, and aerospace industries [4,9]. One of the benefits of the LPBF process is the ability to make complex geometries with fine spatial resolution and high dimensional accuracy [4].

In the LPBF process, there are at least 100 independently controlled processing parameters [10]. The schematic figure showing the widely studied LPBF processing parameters: laser power, scanning speed, hatch spacing, layer thickness, and laser spot size are shown in Figure 1 [11]. These primary variables control the amount of energy supplied per unit volume and the rate of material deposition. Other important variables include scan strategy, build plate temperature, support structures, etc. These parameters affect the melt pool geometry, solidification conditions, defect size and fraction, microstructural, and thus the performance of as-fabricated components [4,12,13]. Identifying the optimal processing condition for a given material is a challenging and time-consuming task, mainly due to the possible range of each parameter. Often, the manufacturer's recommendation is used to select processing parameters, but for new alloy systems or property-tailoring of a manufacturer's recommendation, trial-and-error methods are often required [14,15]. As a consequence, qualification and certification of fabricated parts can be challenging which limits the use of LPBF components in high-end applications [14,15]. To fully exploit the LPBF process, it is necessary to design, predict, and control the microstructural development in viable processing ranges.

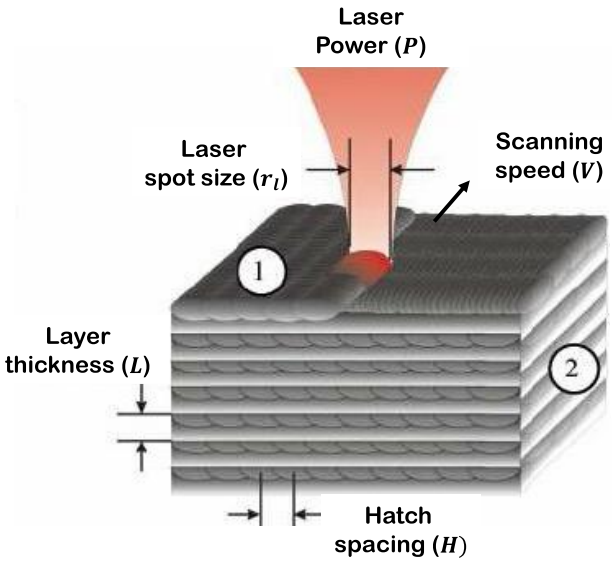

Figure 1. Schematic diagram of the LPBF process showing the widely studied processing parameters: laser power, scanning speed, laser spot size, hatch spacing, and layer thickness [11]

1.2 Laser-metal interaction

Processing parameters combined with the material's thermophysical properties dictate the laser-metal interaction. In this section, a brief discussion of the factors influencing laser-metal interaction and melt pool geometry is provided.

1.2.1 Materials properties

The thermophysical properties of materials provide information about the material's behavior under the application of heat. The most influential thermophysical properties within the context of the LPBF process are melting temperature, density, specific heat, thermal conductivity, and thermal diffusivity [13,16,17]. These properties are either related to thermodynamics or heat transfer phenomena. For example, specific heat is a thermodynamic variable, while thermal conductivity is a variable affecting heat transfer.

A material's intrinsic thermophysical properties like melting temperature, density, and specific heat are constant for a given crystal structure. In other words, their value does not vary with powder particle size or by the mass of powder being exposed to the laser beam. Material density is defined by atomic fraction and location of atoms in a unit cell. The melting point is related to the bond strength while the specific heat is dictated by the lattice vibrations. Typically, a material having a high melting point (i.e., stronger bonds) will have lower lattice vibrations and specific heat value. These parameters vary non-linearly with temperature, pressure, and materials composition. Several handbooks are available that contain an extensive list of the thermophysical properties at different temperature values [18–20].

Thermal conductivity refers to the ability of a material to conduct heat. In metallic materials, the addition of alloying elements decreases electron mobility and thermal conductivity. Thus, the thermal conductivity for pure metals like copper, molybdenum, or tungsten is higher than alloys like stainless steel, superalloys, or high entropy alloys. Thermal diffusivity is the ratio of thermal conductivity to density and specific heat. The product of density and specific heat provides information about the amount of heat that can be stored in a material. Thus, thermal diffusivity represents the rate of heat transfer through the material. Interestingly, copper has a lower melting point of 1356 K as compared to Inconel 718 but still needs a higher energy supply to process [21] because of its high thermal diffusivity [18].

For some materials, thermophysical properties are not readily available in handbooks, especially multicomponent alloys like high entropy alloys or graded alloy compositions. In such cases, a linear approximation method based on the weighted alloy composition can be used as a quick approximation [22]. For a binary composition, the effective density, thermal conductivity, and specific heat can be calculated as:

$$\rho_{eff} = \rho_A X_A + \rho_B X_B \quad (1)$$

$$K_{eff} = K_A X_A + K_B X_B \quad (2)$$

$$C_{p,eff} = \frac{\rho_A X_A C_{p,A} + \rho_B X_B C_{p,B}}{\rho_A X_A + \rho_B X_B} \quad (3)$$

where X_A and X_B are the elemental mole fraction, ρ_A and ρ_B are the elemental density (kg/m^3), ρ_{eff} is effective density (kg/m^3), K_A and K_B are the elemental thermal conductivity (W/mK), K_{eff} is effective thermal conductivity (W/mK), $C_{p,A}$ and $C_{p,B}$ are the elemental specific heat (J/kgK), and $C_{p,eff}$ is effective specific heat (J/kgK).

Experimentally, the thermophysical properties of materials can be measured using thermal analysis. For example, melting temperature and specific heat can be measured using differential scanning calorimetry and the thermal conductivity of metallic materials can be extracted using the light flash method [23,24]. Another material-dependent parameter is the laser absorption coefficient which helps in identifying the energy absorbed by the material. Unlike thermophysical properties, the value of the laser absorption coefficient is a function of laser wavelength, laser parameters, powder particle size, material composition, and powder packing density. The accurate measurement of the laser absorption coefficient is challenging, and dedicated in situ measurements or mathematical modelling is required [25,26].

1.2.2 Processing parameters

LPBF is a complex process where the solidification conditions can vary to a great extent. For example, cooling rates in the LPBF process range from 10^4 K/s to 10^6 K/s [4,27]. Similarly, thermal gradient (G) and solidification rate (R) can vary by two orders in magnitude. Studies have demonstrated that scan strategies and the G/R ratios can be applied to promote columnar-to-

equiaxed transitions and refine the as-fabricated microstructures [28–30]. Beam shaping is another strategy that can be used to alter crystallographic texture or solidification rate in the LPBF process [31,32]. These strategies can affect the residual stress build up, microstructure formation, and eventually the mechanical properties of the material. Powder spreading, and powder contamination levels also have a direct consequence on the as-solidified microstructures and properties of the material, but similar to residual stress or microstructure features, the user has no option to control them independently. In other words, there is no dedicated parameter for controlling residual stress or grain size in LPBF. Therefore, it becomes important to study the effects of processing parameters on laser-metal interaction and solidification conditions.

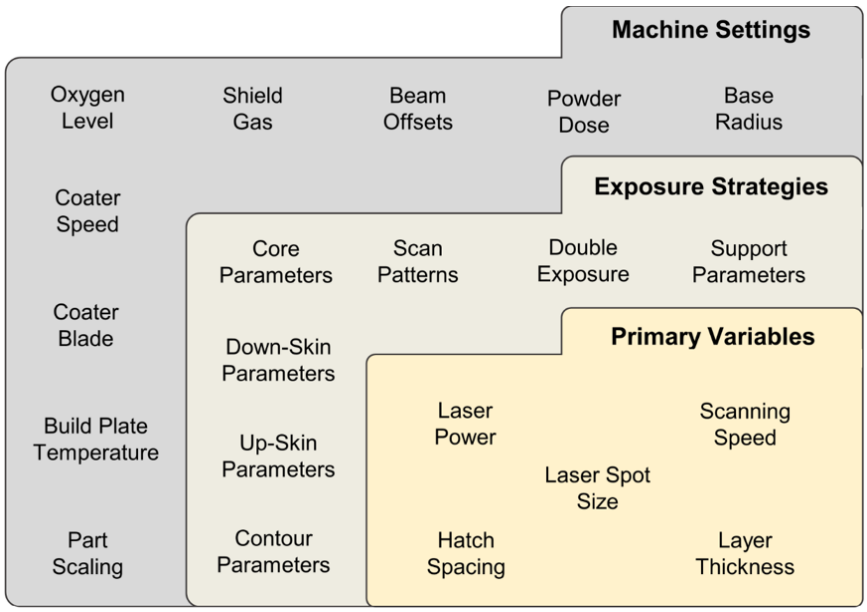

Figure 2. Classification of input processing parameters in laser powder bed fusion process

An example of every independent processing parameter for the LPBF process can be found on the EOS (GmbH, Germany) website [10]. These parameters can be classified into three broad

categories: (i) laser parameters, (ii) exposure settings, and (iii) machine settings as shown in Figure 2. Within each category, the parameters can be further sub-classified either as job-specific, geometry-specific, or powder-specific. For example, coater speed influences the powder spreading and powder bed packing density, and its value depends on powder size distribution (i.e., powder-specific parameter).

In principle, all processing parameters directly or indirectly affect the part's microstructure, properties, and performance. For example, build plate temperature influences residual stresses in LPBF components, shielding gas affects the powder bed contamination and spattering, and support structure parameters dictate the quality of overhanging structures [33–35]. Most studies have focused on five primary processing variables as they dictate the amount of energy supplied as mentioned in Figure 2. For a moving laser beam, the laser power represents the amount of heat supplied to a localized region and the scanning speed relates to the time for which the heat is supplied. A higher value of scanning speed might reduce the print time and cost but make the part more vulnerable to defects. The cross-sectional area of the laser beam varies with height, and thus the laser spot size refers to the size of the laser beam when in focus. Some of the studies have reported a productivity increase of about 840% by using dynamic laser units to control the laser focus-defocus [36]. Laser spot size diameters for most of the AM techniques range between 50-600 µm. For the LPBF process, laser spot size tends to be around 50-100 µm and for the DED process, it is usually around 600 µm. It should be noted that the size of the localized melt pool is not the same as the laser spot size. The melt pool size depends upon the laser parameters, material properties, and laser absorption coefficient. Hatch spacing and layer thickness represent the distance between successive tracks and successive layers, respectively. These parameters affect the re-melting of the previously solidified materials and play an important role in obtaining good

strength and inter-layer bonding. To fabricate sound components, the hatch spacing, and layer thickness shouldn't exceed melt pool width and depth values, respectively. In other words, there should be sufficient melt pool overlap and penetration.

Exposure strategies enable laser parameter variations for a different part's geometric features and microstructural evolution. Down-skin and up-skin parameters refer to the laser parameters for the initial and the final few layers of the deposition, respectively. Core parameters provide information about the laser parameters for the remaining layers between the up-skin and down-skin. As compared to core parameters, up-skin and down-skin layers are often deposited at a lower energy density to obtain a better surface finish [10]. Support structure enables the fabrication of overhanging design features and is purposely made porous to be easily removed in post processing. The energy density requirements for support structures are about 40% of that of core parameters [10]. Scan strategy sets the pattern in which the laser source moves within a layer, and hatch rotation determines the laser movement pattern between successive layers. Some of the common scan strategies are continuous line patterns, stripe patterns, island patterns, and scanning in-out patterns [34]. Each of these patterns has multiple variants with hatch angles aligned at different angles with respect to the horizontal axis. Unidirectional or bidirectional laser motion is another common variation within each scan strategy. Scan strategies affect the local heat distribution, microstructural texture, and residual stresses [37–39]. For example, the default scan strategy for the EOS M290 (GmbH, Germany) system is 5mm stripe thickness with bidirectional laser motion and 67 degrees of hatch angle rotation [10]. Multiple studies have shown that patterns with shorter scan vector lengths, such as the island scan strategy, result in faster cooling and different residual stress states, especially around the sample edges [22,34,40].

1.3 Challenges in LPBF process

One of the major challenges in the LPBF process is to identify an alloy's optimal processing conditions and make a defect-free, fully dense component. Processing defects can limit the strength and ductility of additively manufactured materials [41,42]. Several studies have focused on porosity defect characterization and porosity evolution [16,43–45]. Three common porosity defects observed in LPBF components are lack-of-fusion, balling, and keyhole. These solidification defects can lead to catastrophic failure. For example, failure analysis of additively manufactured 316L SS specimens showed the initiation of cracks at the fabrication-induced pores and defects during tensile testing [46]. In as-fabricated AM parts, defect morphologies, which can vary from spherical pores to high aspect ratio cracks, can also impact failure. For example, accelerated crack initiation was observed in the specimens having lack-of-fusion defects during high-cycle fatigue testing, whereas a minimal effect was observed in specimens having small equiaxed pores [47]. The defect type and volume fraction depend upon the melt pool geometry and processing conditions. Thus, control over the melt pool geometry via processing parameters is crucial for good interlayer bonding and defining an alloy's optimum printability range.

Lack of fusion (LOF) occurs due to insufficient penetration or overlapping of the melt pool. The underdeveloped melt pool or large hatch spacing results in the formation of cavities and porosities in the vicinity of the melt pool boundary. The cross-sectional surface of the LPBF-fabricated 316L stainless steel containing a lack-of-fusion defect is shown in Figure 3. These defects have high aspect ratios, and sharp corners, and their size can range from 1 to 100 μm. Low laser power or high scanning speed can make the part vulnerable to lack-of-fusion defects [48,49]. In a study by Mukherjee *et al.* [50], a normalized heat-input parameter (a non-dimensional number) showed a linear dependence on the number of lack-of-fusion defects.

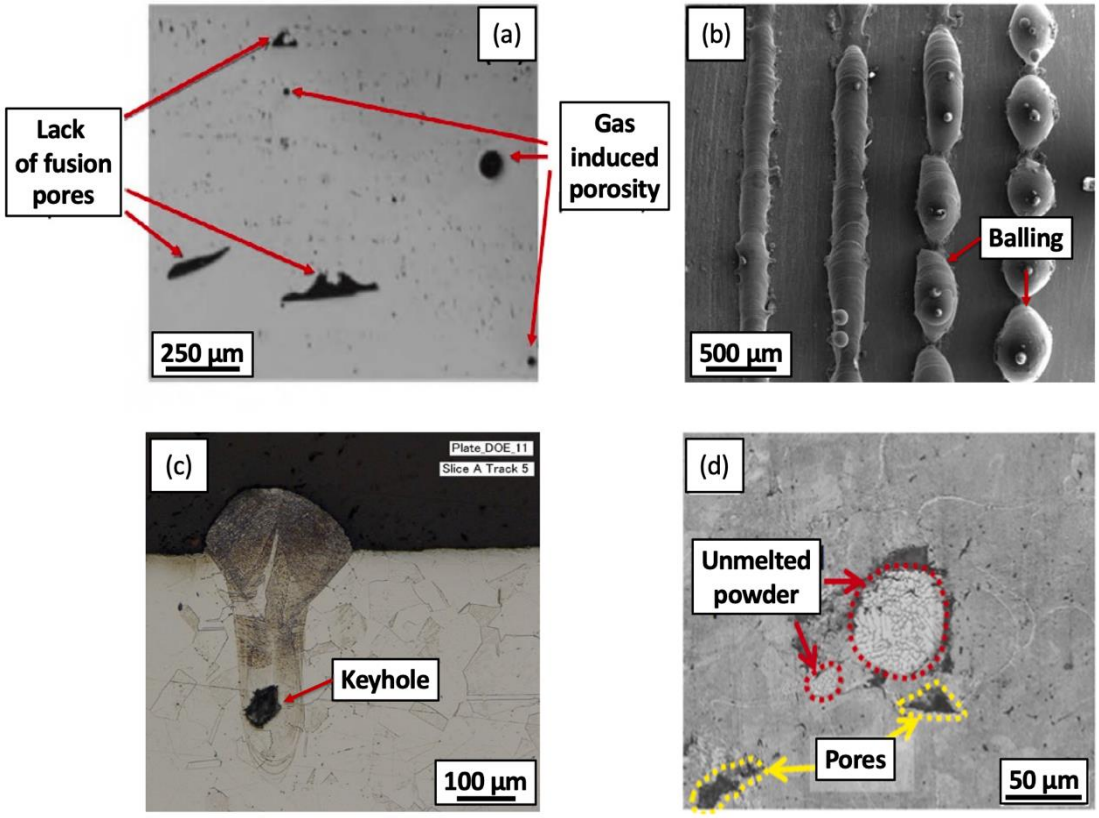

Figure 3. Cross sectional images of parts containing (a) lack-of-fusion defects [51] (b) balling [52] (c) keyhole porosities [53] and (d) unmelted powder particles [54].

Balling (or Rayleigh-Plateau) refers to the melt pool instability in which a small hump forms along the printed track. The instability in the melt pool occurs at high values of melt pool length to depth ratio. In such cases, the molten metal tries to lower its surface energy by forming a sphere rather than spreading freely over the unmelted substrate. The high contact angle between the spherical humps and the previously solidified layer results in porosity formation as shown in Figure 3. Balling can also affect the subsequent layer's powder packing, imparting processing defects, and increasing the part's surface roughness. A lower laser power and scanning speed

decrease the melt pool length and the chances of balling porosity [52,55]. High laser power and high scanning speed can promote balling [52,56].

Keyholing, in contrast to the lack of fusion, occurs due to excessive penetration of the fusion zone [53,57]. In such cases, higher vaporization, and recoil pressure result in cavity formation within the melt pool boundaries as shown in Figure 3. These defects generally have ellipsoidal or spherical geometries. Cunningham *et al.* [58] found that keyholing occurs when the keyhole front angle exceeds a critical value of 77 degrees. High laser power and low scanning speed increase the melt pool depth and thus the potential for keyhole defects [58].

Another potential processing defect can be the presence of under-melted or partially melted particles in the part. Under the scenarios of a low energy supply or a material with a low laser absorption coefficient, the fraction of under-melted particles can be high [54]. The cross-sectional surface of a component containing under-melted particles is shown in Figure 3. The issue of partially melted particles becomes more prevalent when two or more elemental powders having very different melting temperatures are mixed to get the desired alloy composition.

In addition to the porosity defects and partially melted particles, another challenge in the LPBF process is the ability to control the microstructure. The moving heat source thermally affects prior layers as a function of spatial and temporal processing conditions. In addition, rapid solidification and high thermal gradients lead to heterogeneous solidified microstructures [12,13]. Microstructural analysis shows the presence of high dislocation densities, columnar grain structure, sub-granular cellular structures, and crystallographic texture in as-fabricated parts [59]. The length scale of these microstructural features ranges up to five orders in magnitude [12]. Transmission Electron Microscopy (TEM) analyses show the presence of dislocation networks in the cell boundaries region [60,61], which could be effective in blocking the motion of dislocations.

Generally, with an increase in the energy input, the cellular-dendritic spacing increases [62]. In a recent study by Andreau et al. [63] crystallographic texture showed a strong correlation with the melt pool geometry and hatch spacing.

Commercially a limited number of alloys are currently available for LPBF fabrication. The LPBF process also offers material scientists an opportunity to discover new alloy compositions and take advantage of its constraints-free alloy design space. For example, the accelerated discovery of new high entropy alloys [64] and bulk metallic glass compositions [65]. However, each element and alloy compositions come with its unique processing challenges. For example, low laser absorptivity is an issue for fabricating pure copper, and high oxygen affinity is an issue for aluminum powders [54,66,67]. Poor feedstock powder quality and non-uniform powder size distribution even add complexity to this problem [68].

When processing conditions are well selected, as-fabricated AM 316L SS can show higher strength and ductility as compared to wrought 316L SS [69]. The main factors attributed to a strength increase are the cellular dendritic structure, grain size, and dislocation density [60,70,71]. The increase in ductility was attributed to a higher propensity for deformation twinning [12,72,73]. AM 316L SS also showed excellent fatigue strength and fatigue crack growth threshold values as compared to wrought materials, primarily due to high yield strength to tensile strength ratios [74,75]. However, the columnar grain and crystallographic texture in the build direction can often lead to anisotropic properties. For example, in 304L SS higher ductility was observed along the transverse direction, as compared to the building direction, while, both directions showed similar tensile strength [76].

1.4 State of the art and limitations of current practice

Prior studies have used *in situ* x-ray and thermal imaging techniques to observe the laser-metal interaction at a high spatial and temporal resolution [77,78]. The intensity of the synchrotron x-ray images represents density variations which help in identifying melt pool morphology, tracking spatter particles, and understanding pore formation mechanisms [45,78–80]. In a study by Guo *et al.* [81], synchrotron x-rays were used to calculate the melt pool dimensions at different processing conditions. Usually, the melt pool morphology changes from semi-spherical ($width \approx 2 * depth$) to deep ($depth \gg width$) with increasing laser power. This change in melt pool morphology occurs with a simultaneous increase in melt pool width and melt pool depth [44]. However, these techniques can be very expensive it requires high-energy incoming x-rays and advanced detector and instruments. In addition to synchrotron x-ray imaging, infrared cameras can be used to map the temperature distribution during melting and solidification as shown in Figure 4. This technique provides information such as melt pool dimensions, peak temperature, and local heating cycles, and can be applied as a feedback control system for processing parameters [82,83]. Although the resolution of images obtained from infrared cameras is less than synchrotron x-ray imaging, they are easier to acquire and analyze.

In addition to *in situ* techniques, other studies have focused on mathematical modelling techniques to understand various aspects of AM process. For example, finite element method (FEM) models have been used to calculate heat transfer and solidification conditions, and computational fluid dynamics (CFD) has been used to study melt pool dynamics [22,84,85] as shown in Figure 4. In a study by Lee *et al.* [17], thermal gradient and solidification rate were calculated to compare the solidification morphologies at different processing conditions for LPBF Inconel 718. Similarly, analytical models have also been developed to predict the melt pool

geometry, ideal hatch spacing, and defect boundaries [50,53,56,86,87]. Unlike FEM simulations, analytical models are time-efficient, computationally inexpensive, and provide a quick approximation. However, it is almost impossible to accurately model the complex heat transfer and melt pool dynamics.

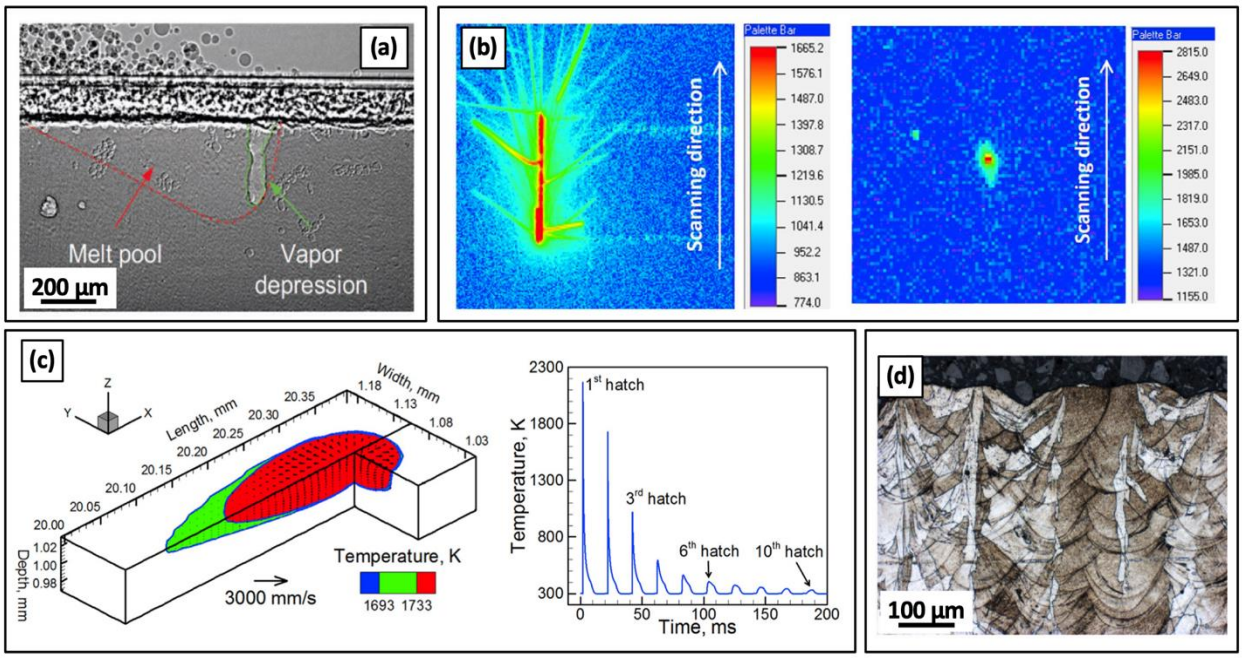

Figure 4. Different approaches are used to study melt pool (a) in situ synchrotron x-ray imaging [78] (b) in situ infrared thermal imaging at two different temperature ranges [88] (c) FEM-based simulations [84] (d) optical microscopy of as-fabricated materials [63].

Power-Velocity (PV) processing maps are a powerful tool to visualize the effects of LPBF processing variables to produce high density parts as shown in Figure 5. These maps provide useful information about the defect population and processing window to fabricate full density specimens. Processing maps have been systematically used by Beuth *et al.* [89] to overlay the contours of the part's density, surface roughness, and build rate onto a PV map. A few other recent

studies [90,91] have extended this idea and constructed processing maps for different materials like titanium, Ni-Nb, and a high entropy alloy. Processing maps for welding, deformation, and other manufacturing techniques were previously developed to guide users about the optimum processing conditions. However, most of these studies have focused on defects at different processing conditions, and there is a lack of understanding about micro structure evolutions and property variations at these conditions. Also, analyzing multiple samples from a large processing space can be a time-consuming task.

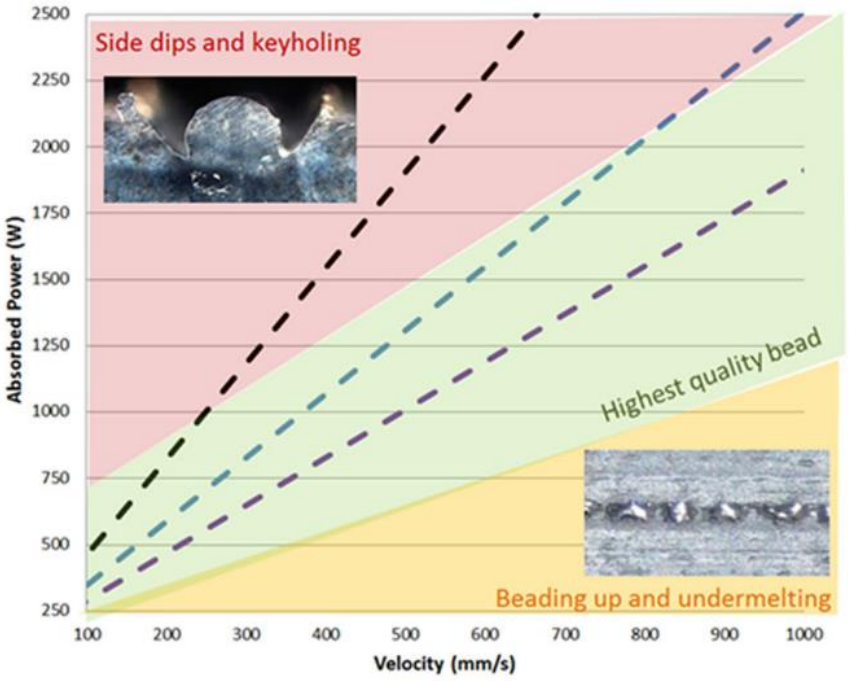

Figure 5. Typical Power-Velocity (PV) maps showing different processing regions for 316L stainless steel [89]

1.5 Primary goals and research objectives

The foregoing discussions in the earlier sections illustrate the opportunities and challenges in metal additive manufacturing. To commercialize LPBF techniques for high-end applications, process control and part printability needs to be improved.

The hypothesis and central idea behind the thesis are "**a control over melt pool geometry and laser-metal interaction is crucial to mitigate porosity defects and improve part's printability**". Also, a rapid screening technique of the AM samples is required to explore the large processing space and develop AM process for a variety of materials. A high-throughput approach was developed to address the problem. Specifically, the high-throughput approach can be beneficial for the LPBF process as the processing space is too large. Moreover, the interdependence of the parameters can be developed to rapidly define correlations not available in existing models. The overarching objectives of this thesis are as follows:

1) To develop a high-throughput approach enabling rapid interrogation of samples fabricated over a large LPBF processing space
2) To identify the physical and surface signatures of the additively manufactured materials
3) To develop a universal predictive model to estimate the alloy's processing bounds
4) To apply predictive models to new material systems and improve the alloy's printability
5) To understand the influence of processing parameters on the solidification conditions and as-fabricated microstructures.
6) To generate microstructure-based and property-based processing maps

Chapter 2: High-throughput experimentation to identify processing bounds

---

This chapter introduces the high throughput fabrication and characterization technique to rapidly identify the LPBF processing bounds. The experimental data and results presented in this chapter have been published in the following work:

- A.K. Agrawal, G. Meric de Bellefon, D. Thoma, High-throughput experimentation for microstructural design in additively manufactured 316L stainless steel, Mater. Sci. Eng. A. 793 (2020) 139841. doi:10.1016/j.msea.2020.139841.

In sections 2.4 and 2.6, a universal dimensionless number to predict the optimal processing regime and its application to process design Haynes 282 alloy are presented. In this collaborative work, my major role was to develop the HT experimental approach, design of experiments, data generation, and analysis for different metals and alloys. The experimental data and results presented in sections 2.4 and 2.6 have been published in the following work:

- B. Rankouhi, A.K. Agrawal, F.E. Pfefferkorn, D.J. Thoma, A dimensionless number for predicting universal processing parameter boundaries in metal powder bed additive manufacturing, Manuf. Lett. 27 (2021) 13–17. doi:10.1016/j.mfglet.2020.12.002.
- Z. Islam, A.K. Agrawal, B. Rankouhi, C. Magnin, M.H. Anderson, F.E. Pfefferkorn, D.J. Thoma, A High-Throughput Method to Define Additive Manufacturing Process Parameters: Application to Haynes 282, Metall. Mater. Trans. A. 53 (2022) 250–263. doi:10.1007/s11661-021-06517-w.

As discussed in the previous section 1.3 and section 1.2, hundreds of independently controlled processing variables affects the printability of LPBF components. Thus, there exists a critical need to develop a high throughput experimental approach and quickly assess the effects of processing variables on printability.

2.1 Introduction

Although high-throughput and combinatorial techniques have been widely used in the biological and pharmaceutical industry [92–94], HT techniques are gaining more acceptance in the materials community [95–97]. In an HT method, an array of samples is created with variations in composition or process parameters or other influencing factors [98]. After fabrication, the array of samples is screened to figure out the ‘‘sweet spot’’ for the property of interest as a function of composition or process parameters. The technique is faster compared to ‘‘one sample at a time’’ i.e., conventional manufacturing. Moreover, since all measurements are carried out on the same batch of samples and using the same tool at the same time, it is assumed that most of the systematic errors are eliminated during HT characterizations and generated data are reliable.

High-throughput (HT) experiments may permit faster rates of design of experiments (DOE), particularly when guided with a fundamental premise [95,96]. Large datasets obtained from HT experiments can be used as training sets for various machine learning algorithms [99,100] and can be used to predict the process parameter ranges. Ren *et al.* [65] have demonstrated the combined use of HT and machine learning for the discovery of metallic glasses. Specifically, for AM, given a known set of process parameters corresponding to specific material, HT can allow a systematic interrogation of processing parameter variations [101–103]. Moreover, the interdependence of the parameters can be developed to rapidly define correlations not available in existing models. Recent studies [104,105] using an automated HT tensile test were performed to evaluate the effects of processing parameters on the mechanical behavior of AM 316L SS. Other studies [106] have focused on HT process control via in-situ monitoring of the melt pool. To expand the AM techniques to other alloy systems, HT experiments are needed to quickly fabricate,

characterize, and identify the appropriate processing window, especially since there are a large number of processing variables in the LPBF technique.

In this work, hundreds of hex nut-shaped samples were fabricated at different combinations of processing conditions. An easily removable scaffolding permitted rapid sample extraction from the base plate, thus saving machining cost and time. A high throughput density and hardness measurements helped in identifying the estimates for lack of fusion offset and keyhole threshold for different materials like 316L stainless steel, Inconel 718, Haynes 282, cantor alloy, refractory materials, etc. A hex nut-shaped geometries of similar dimensions are useful for HT investigations as they provide two major benefits. First, easy extraction of samples from the build plate using a socket wrench. Second, six side surfaces to perform six hardness measurements at each side face.

The novelty of this work lies in using high-throughput fabrication and characterization techniques to quickly analyze LPBF-fabricated materials. These techniques allowed the identification of the processing bounds within a reasonable time frame of 2-3 days. Finally, a dimensionless number based on the material's properties and laser processing parameters is presented to provide a predictive estimate of the processing bounds for a new alloy system.

2.2 Experimental procedure

2.2.1 Material of interest

In this work, a wide range of pure metals and alloys have been additively manufactured such as stainless steel, nickel-base superalloys, high entropy alloys, aluminum alloys, copper, and refractory metals. These materials represent a wide range of thermophysical properties. For example, tungsten and molybdenum have a high melting point, copper has a high thermal

conductivity, aluminum alloys have a low density. Thermophysical properties of these materials is shown in Table 1. An extensive list of materials properties for several commercial alloys are available in handbooks [18,25]. In the AM process, thermophysical properties influence the melting and heat transfer and thus the laser-metal interaction. For example, thermal diffusivity of these materials varies two orders in magnitude from 2.88 to 115 mm^2/s, which significantly affects the material's ability to conduct as respect to store thermal energy. All of these metal powders for the LPBF process were procured from commercial sources. The powder particle size for each material was in the range of 15-40 µm as provided by the supplier.

Table 1. Thermophysical properties of commercial metals and alloys.

Material	Laser absorption coeff.	Melting temp (K)	Density (Kg/m^3)	Specific heat (J/KgK)	Thermal conductivity (W/mK)	Thermal diffusivity (mm^2/s)
316L SS	0.6	1683	7895	450	13.8	3.90
IN 718	0.5	1609	8150	435	11.4	3.20
H282	0.5	1648	8300	436	10.3	2.88
Cantor	0.4	1349	8042	430	12	3.47
AlSi10Mg	0.5	843	2680	915	110	45.00
Cu	0.4	1356	8930	384	399	115.00
Mo	0.4	2893	10220	250	142	56.00
W	0.4	3693	19250	130	164	66.00

2.2.2 High-throughput fabrication

All of the materials (as shown in Table 1) were additively manufactured in different batches using the EOS M290 system. A 400 W Ytterbium fiber laser with a wavelength of 1060 nm and a beam diameter of 100 µm was used as the energy source. Prior to build, wrought 316L stainless steel (SS) build plates were preheated to 80˚C, and an inert argon atmosphere was maintained throughput the chamber. A set of hex nut-shaped specimens, each having a width of 3.17 mm (1/8th in.) and a height of 3.0 mm, was fabricated. Each of the hex nut specimens were processed at different combination of laser power, laser scanning speed, and hatch spacing. All the other parameters such as stripe thickness = 5 mm were kept constant. These specimens were deposited over a 3.0 mm porous support structure for easy removal from the build plate as shown in Figure 6. The porous support structure was fabricated using the factory's default processing conditions. In addition, a volumetric energy density (VED) parameter was used to compare the combined effects of these parameters. VED (J/mm^3) signifies the amount of input energy into the melt pool and is defined by the equation:

$$\text{Volumetric Energy Density (VED)} = \frac{P}{VHL} \tag{4}$$

where P is the laser power (W), V is the laser scanning speed (mm/s), H is the hatch spacing (mm), and L is the layer thickness (mm).

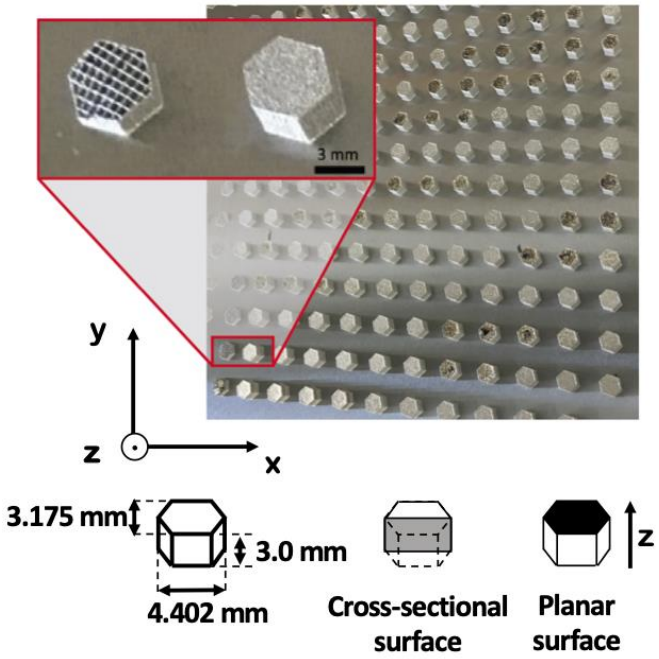

Figure 6. Schematic diagram of the hex nut geometry and a picture of the 316L SS hex nuts fabricated at different power and velocity combinations using an EOS M290

2.2.3 High-throughput characterization

HT hardness and density measurements on all hex nut specimens were performed. Hardness measurements were performed using the Rockwell tester. All the indents were made on the center of the side surface (xz plane) to maintain consistency. At least five indents were made on each specimen (as-fabricated surface) to get the average hardness measurements. Before the density measurements samples were grounded to remove any residual support structures from the bottom. An immersion density measurement method was used based on the Archimedes principle [107] using a Fluorinert™ FC-40 solution. An ASTM Standard B962 [108] was followed while measuring the density. Samples density (ρ_{sample}) were calculated using the equation:

$$\rho_{\text{sample}} = \frac{\rho_{\text{fluid}} \times m_{\text{dry}}}{m_{\text{dry}} - m_{\text{wet}}} \quad (5)$$

where ρ_{fluid} is the density of the FC-40 solution (= 1.86 g/cc), m_{dry} is the dry weight of the sample, and m_{wet} is the weight of the sample when freely suspended in the fluid. The relative density (%) was calculated by normalizing the dataset with respect to the densest sample.

2.3 High-throughput characterization of 316L SS

2.3.1 Density measurements

Immersion-based density measurements of the hex nut specimens as a function of VED are shown in Figure 7a. In the lower VED range of 5-70 J/mm^3, the density of the specimen increases from 75% to 98.5% with increasing VED. A linear dependence of density with energy density suggests the presence of lack-of-fusion type defects in these specimens [50]. In the VED range of 5-20 J/mm^3, few specimens showed relatively higher densities than the rest of the specimens. In these specimens, open pores were observed (Figure 7b) suggesting misleading density measurements, and thus those data points were treated as outliers. The presence of open pores in the unfused specimens is probably due to extremely low laser power or very high scanning speed values. A saturation point in the density was observed at 70 J/mm^3 which might be related to the lack-of-fusion offset. In the VED range of 70-150 J/mm^3, a similar and constant density was observed. The maximum density recorded was 7.90 g/cc (i.e., 99% dense as compared to wrought 316L SS). The actual specimen density may have some deviation due to surface roughness effects.

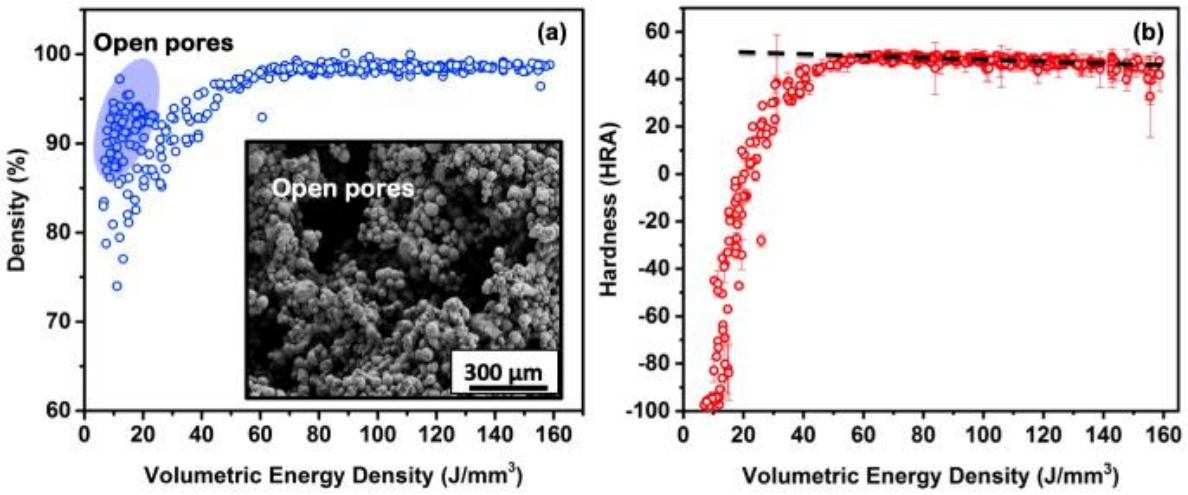

Figure 7. (a) High-throughput density measurement using Archimedes principle. Inset showing a SEM image of as-fab specimens (unpolished, bottom surface) having open pores. (b) High-throughput hardness measurement using a Rockwell indention.

2.3.2 Hardness measurements

Average hardness measurements of the hex nut specimens are shown in Figure 7b. Similar to density, the specimen's hardness increases with VED before reaching a maximum value of 50.1 HRA. Both density and hardness measurement showed a peak in the similar VED value suggesting a lack-of-fusion offset to be around VED ≈ 70 J/mm^3. Almost all the specimens in the lower VED, i.e., below 20 J/mm^3, showed a negative hardness value. The negative value stems from the material being too soft for the HRA scale measurement. The HRA scale is effective in measuring the hardness between 112 to 513 HV and if hardness is below 112 HV, Rockwell B or F scale should be used. Since most of the specimens were in the range of the HRA scale, only the HRA scale was used for consistency. A drop in the hardness from 50.1 to 39.95 HRA was observed in the VED ranging from 70-150 J/mm^3. The observed linear relationship between hardness and VED was obtained within the processing regime of VED = 70-150 J/mm^3 can be expressed by:

$$\mathrm{HRA} = 53.3 - 0.055 \times \mathrm{VED} \quad (6)$$

A p-value of $4.9\text{x}10^{-24}$ suggests the data to be statistically significant, despite an R-square value of 0.424. Above 150 J/mm^3, the average hardness values had increased scatter. Both HT density and hardness measurements suggests the processing offsets for 316L stainless steel is in the VED range of 70-150 J/mm^3 as shown in Figure 8.

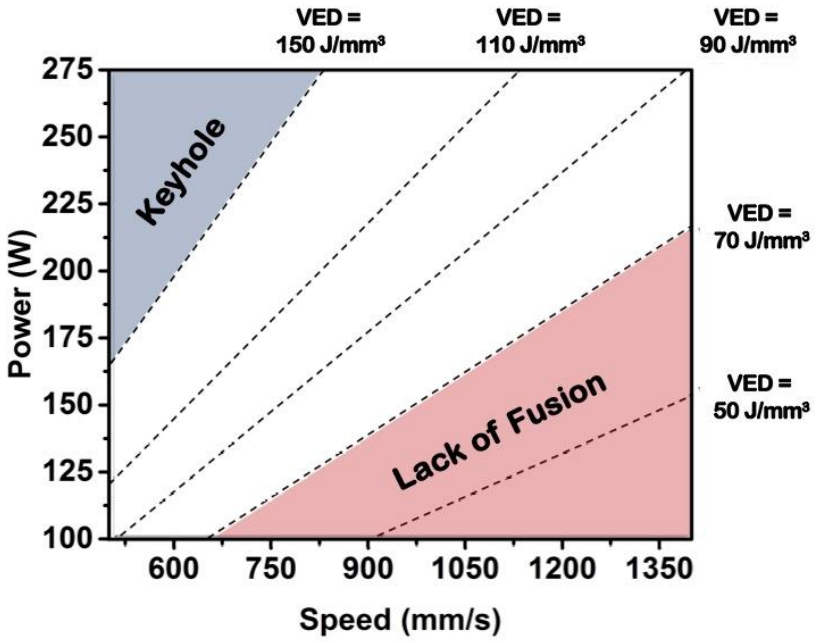

Figure 8. High-throughput processing map for 316L stainless steel

Both density and hardness measurement showed a strong correlation with VED (slope of PV graph) as demonstrated in Figure 7. Prior studies on 316 SS and Al-Si alloys have highlighted the limitations of volumetric energy density [109,110] as it fails to capture the overall melt pool physics. These previous studies have shown different density and hardness values for the same values of VED. In the present study, similar density and hardness values were observed for the

specimens with constant energy density, at least at the very coarse level afforded with the HT methods. At and beyond VED boundaries, like VED = 151.5 J/mm^3 where keyholing porosity is predicted, variation in hardness (50.1 to 40.0 HRA) was observed. This suggests that VED can be considered as a reliable parameter, at least within the boundary regions used in this study, but at too high or too low VED, power or velocity independently may have a stronger effect on the microstructure.

2.3.3 Defects and pores morphology

SEM images of the defects and pores from different regions of the HT measurements are shown in Figure 9. At a very high energy density sample (VED = 212.1 J/mm^3) keyholing defects were observed (Figure 9a). The keyholes were about 20-50 µm in size and had a spherical morphology. These defects were randomly distributed within the specimens and easy to find. The amount of keyhole pores was less prominent (but roughly the same size) as the VED approached 150 J/mm^3. Within the boundary regions of the LT study (i.e., VED = 70-150 J/mm^3) relatively dense specimens were obtained. These specimens (VED = 113.6 J/mm^3) showed pores in sub-micron size ranges (not clearly visible in Figure 9b) and are potentially confused with inclusion pull-out. The specimens at lower energy density (VED = 41.9 J/mm^3) i.e., below the lower boundary region (< 70 J/mm^3) showed various characteristics of lack-of-fusion, processing cracks, and un-melted powders. (Figure 9c). These defects have a high aspect ratio, and many have sharp edges. Overall, the defects and pores investigation showed a good correlation with the HT measurements.

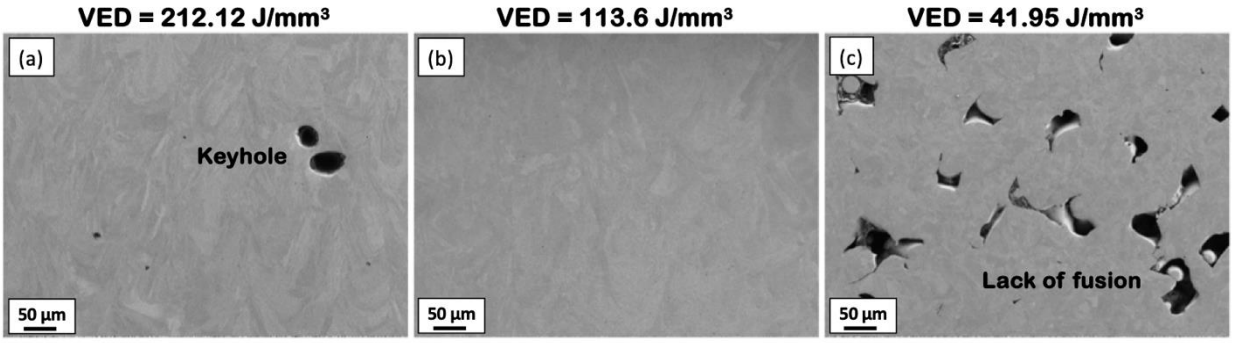

Figure 9. SEM images from different regions of PV maps showing (a) keyholes (b) high density and (c) lack-of-fusion type of porosities.

2.4 Dimensional analysis

A dimensional analysis was performed based on the Buckingham-Π theorem [111]. Pawlowski's matrix transformation method was used to identify different sets of dimensionless numbers for the LPBF process. Here, only the newly discovered dimensionless numbers are reported. A comprehensive list of well-known dimensionless numbers especially for the LPBF process like Fourier number, Peclet number, Biot number, Marangoni number, and Non-dimensional heat input can be found elsewhere [50,112,113]. The process variables appearing in the dimensional analysis are listed in Table 2.

Pawlowski's matrix transformation method helped in identifying two new dimensionless numbers. These numbers [114] can be expressed as a function of laser parameters and thermophysical properties:

$$\mathrm{E_{dim}} = \pi_1 = \frac{\mathrm{C_p P}}{\mathrm{K V^2 H}} \tag{7}$$

$$\mathrm{E_{dim2}} = \pi_2 = \frac{\mathrm{C_p}}{\mathrm{K}} \times VED \times \tau \tag{8}$$

where P is laser power (W), V is scanning speed (m/s), H is hatch spacing (m), τ is dwell time i.e., a ratio of laser beam diameter and scanning speed (sec), K is thermal conductivity (W/mK), C_p is specific heat (J/KgK), and VED is volumetric energy density (refer to equation (4).

Table 2. Process variables appearing in the resulting dimensionless number.

Process Variable	Description	Unit	Dimension
P	laser power	(W)	ML2T-3
v	laser scan speed	(mm/s)	LT-1
t	nominal layer thickness	(mm)	L
d	laser beam diameter	(mm)	L
h	hatch spacing	(mm)	L
Cp	specific heat capacity	(J/kg-K)	L2T-2θ-1
k	thermal conductivity	(W/mm-K)	MLT-3θ-1

The dimensionless number (E_{dim}) showed a good correlation with the relative density for various metals and alloys as shown in Figure 10. It can be observed that with an increase in dimensionless number the alloy's relative density increases till E_{dim}value reaches 61. Over a certain region (E_{dim}= 61 to 146) dense samples with a relative density of around 99.5% were obtained. Beyond the E_{dim}value of 146, the density values start to drop off. As a result, the stable region of $61 < E_{dim} < 146$ is designated as the green zone or the alloy's processing window.

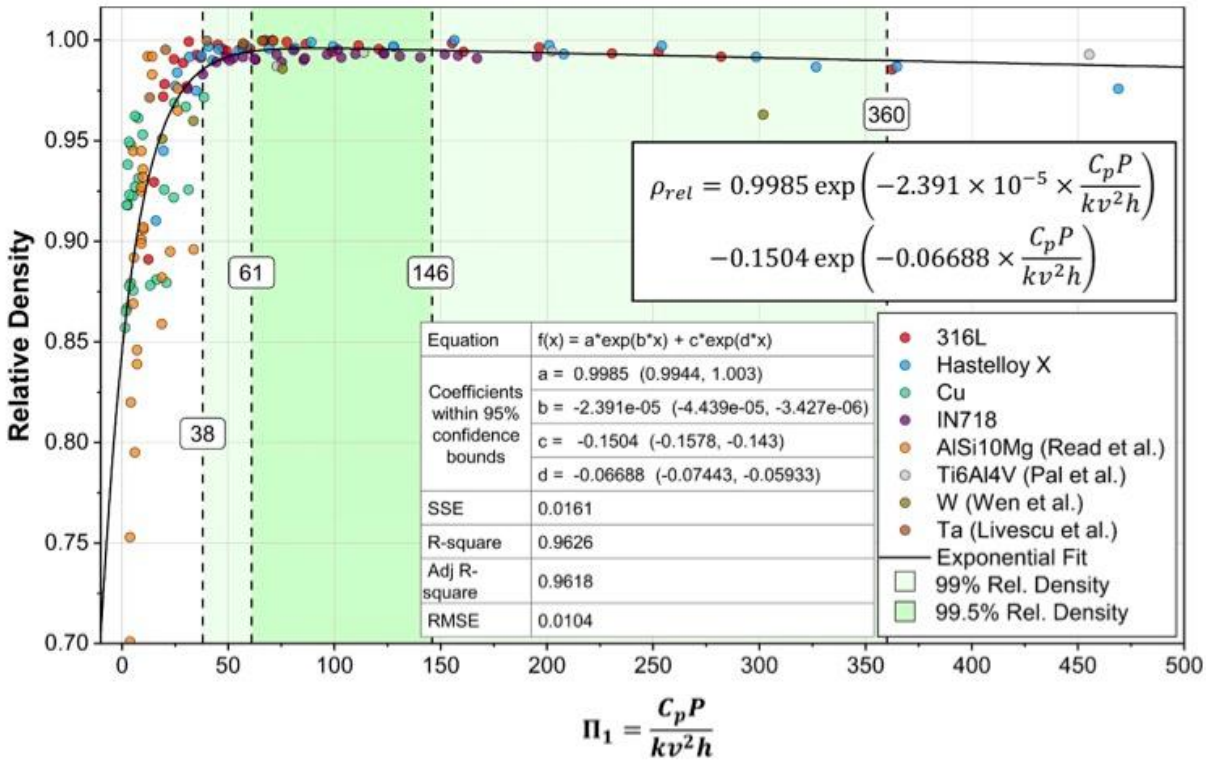

Figure 10. Correlation between relative density and dimensionless energy density

Dimensionless numbers offer flexibility and help in translating the volumetric energy density across different material systems and LPBF machines of different laser beam diameters. Since multiple experimental and reported data for various alloys have followed a similar dependence thus the dimensionless number can be used effectively to predict the LPBF processing bounds. An exponential based function helped in formulating the universal scaling laws with the R-square of 96%. The relative density estimates for a given processing condition can be made using the following equation [114]:

$$\rho_{rel} = 0.9985 \exp\left(-2.391 \times 10^{-5} \times \frac{C_p P}{K V^2 H}\right) - 0.1504 \exp\left(-0.06688 \times \frac{C_p P}{K V^2 H}\right) \quad (9)$$

2.5 Reliability of HT density experiments

A similar HT approach was applied to Inconel 718 and Cantor alloy. Both the alloys showed a strong correlation with the dimensionless energy density as shown in Figure 11. Interestingly, within the processing bounds (E_{dim}= 61 to 146) the relative density of the IN 718 alloys was in the range of 99% but the samples were dense and had minimal defects. This is primarily due to the outlier points in the data set at E_{dim} = 74 which contributed to errors in the normalization of the relative density values. Similarly, the Cantor alloy samples showed a high density of >99.5% within the processing bounds as shown in Figure 11b. However, during the cross-sectional analysis micro cracks were observed in those samples which are not representative of the measured density values. In short, abnormality in density values can arise due to measurement errors but HT experiments can help in estimating the processing bounds for lack of fusion and keyholing porosities. An estimation of the processing bounds for a variety of materials (as listed in Table 1) was performed using HT experimental approach.

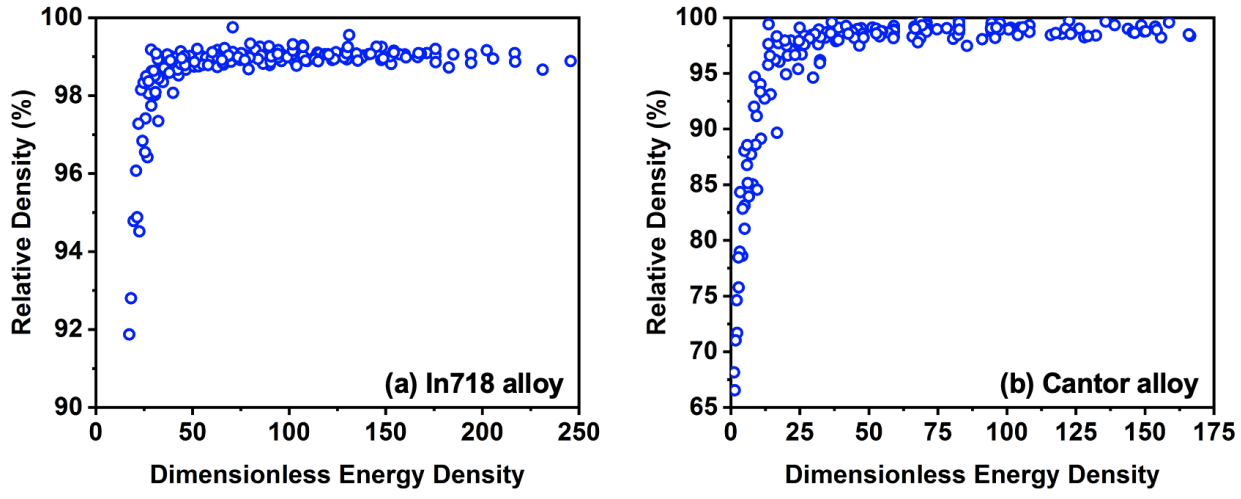

Figure 11. High throughput density measurements for (a) Inconel 718 and (b) Cantor alloys

To further understand the reliability and reproducibility of the HT measurements, two separate batches of In718 alloys were fabricated. Both the batches contained identical processing parameters for comparison and the samples were randomly placed over the build plate without giving any site preference to any samples. The variation in the relative density measurements is shown in Figure 12. The statistical analysis of the samples showed that on average the density measurements have an error of 0.16%. For some cases, the variation in relative density between two batches was in the range of 0.5-0.65%, especially in the lack of fusion region.

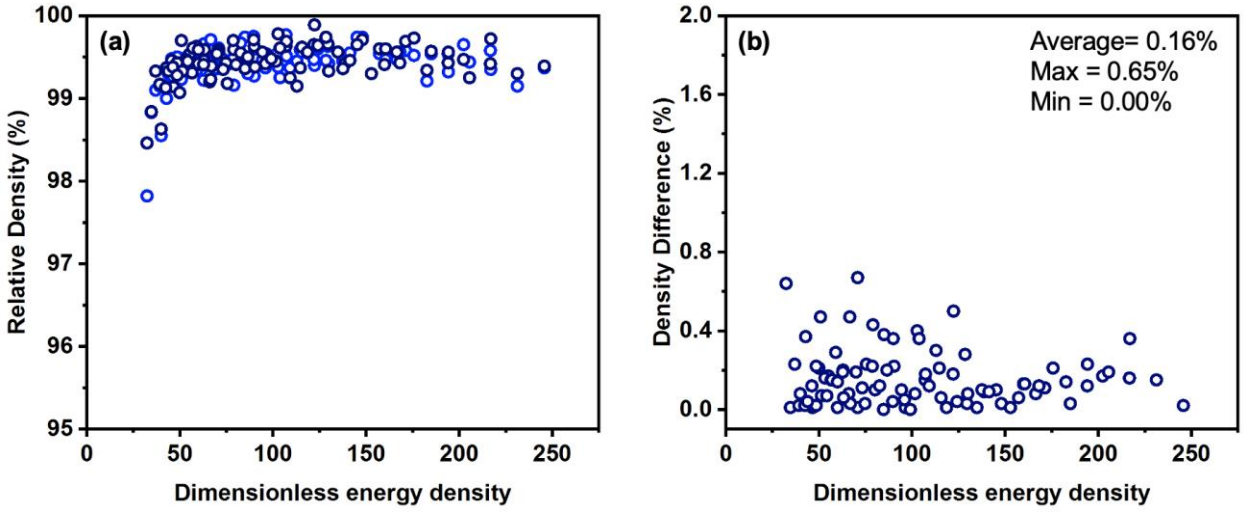

Figure 12. Reproducibility of high throughput density measurements. Two batches of In718 alloys were fabricated containing identical processing parameters randomly positioned over the build plate as represented by the blue and dark blue data points.

The study highlights that samples may show marginal deviation from the actual density values, but they are effective for quick approximation [107]. For example, the surface roughness of the as-fabricated LPBF specimens may introduce errors in both hardness and density measurements. Some other valuable information such as the defect's size, morphology, and

distribution also cannot be traced using these techniques. For such measurements, electron microscopes or x-ray microtomography would be a more suitable technique. However, electron microscopy and microtomography techniques can't be used for HT measurement, as analyzing hundreds of specimens using these techniques would not be feasible. The time estimation for HT fabrication is around 12 hours, out of which most of the time is devoted to the automated printing process. On average, HT immersion-based density measurement takes 2 minutes per specimen, and hardness measurement takes 4 minutes per specimen. As a result, HT fabrication and characterization can be performed within 22 hours for a batch of 100 specimens.

Overall, HT experiments are quick, efficient, and reliable in identifying the lower and higher processing bounds. In addition, the real value of this HT technique lies in creating large datasets that can effectively couple with machine learning models for rapid processing parameter discovery. Ideally, this approach can be applied to any material system and within a span of 22 hours, hundreds of specimens can be fabricated, extracted, and analyzed to determine the processing bounds.

2.6 Applications to Haynes 282 alloy

Haynes 282 alloy is a Ni-base precipitation harden alloy mainly used for high temperature structural applications. To test the universality and predictive capability of dimensionless numbers, high throughput experimental approach is applied to H282 alloy as shown in Figure 13. The HT density and hardness measurements showed similar trends as predicted based on the dimensionless number. In the plateau region of $61 < \Pi_1 < 146$ samples showed the highest density and hardness while below $\Pi_1 < 61$ and above $\Pi_1 > 146$ the porosity mode of lack of fusion and keyhole respectively was observed.

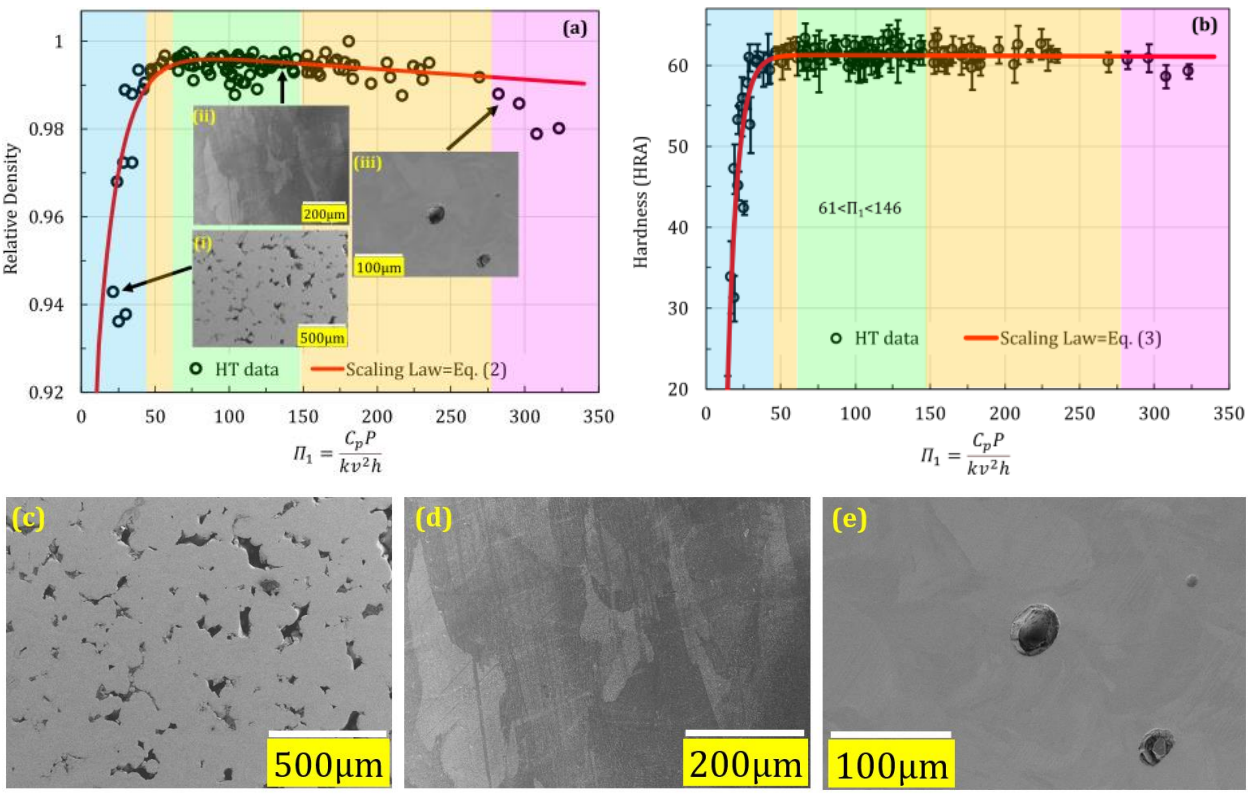

Figure 13. (a) Relative density as a function of dimensionless number Π_1; (b) Correlation between hardness and dimensionless numbers Π_1; Magnified view of inset micrographs in (a) showing: (c) Lack of fusion (LOF) porosity (from blue region), (d) specimens free from porosity (from green region), and (e) keyhole type porosity (from pink region). The yellow region indicates samples with high density but statistically containing regions of possible process defects.

Similar to the relative density, a scaling law that correlates HRA to the dimensionless number can be formulated as follows:

$$\mathrm{HRA} = 61.36 \exp\left(-1.266 \times 10^{-5} \times \frac{\mathrm{C_p P}}{\mathrm{K V^2 H}}\right) - 366.4 \exp\left(-0.15 \times \frac{\mathrm{C_p P}}{\mathrm{K V^2 H}}\right) \qquad (10)$$

Unlike the scaling law expressed in equation (9, the scaling law for HRA values is fitted to Haynes 282 data only and is not universal. Based upon the scaling law expressed by equation (10, the HRA drops below 60 as Π_1 value drops below 61. A gradual drop in hardness value may also occur when the samples enter the keyhole regime at $\Pi_1 > 146$.

This study shows that HT experimental data validate the effectiveness of the dimensionless number to identify a complete process boundary with lack-of-fusion and keyhole regions. For printing of Haynes 282, processing parameters of $P = 250$ W and a scan speed of 1000 mm/s, with an $h = 0.11$ mm and $t = 0.04$ mm would be the middle of the defined region with maximum density.

2.7 Conclusions

Overall, HT experiments enabled the fabrication, analysis, and screening of hundreds of specimens. This approach was applied to a wide range of materials such as stainless steel, nickel base superalloys, high entropy alloys, aluminum alloys, copper, and refractory materials. Based on the results and analysis the following conclusions can be reached:

1) The high-throughput approach is a quick, reliable, and effective way for identifying the processing bounds of as-fabricated LPBF components.
    a. A hex nut geometry is useful for high-throughput fabrication, density, and hardness measurements.
    b. Quick density and hardness measurements provided the estimates for the lack-of-fusion region and keyholing regions.
    c. The high-throughput analysis can be completed in 22 hours, allowing rapid definition of process parameters for an alloy system.

2) Dimensionless energy density can be an effective tool to predict the LPBF processing bounds and estimate the relative density value for given processing conditions.
    a. In the alloys processing region or green zone i.e., $61 < E_{dim} < 146$ high relative density of >99.5% was observed for different metals and alloys.
    b. Universal scaling laws can help in predicting the relative density and the porosity mode during fabrication.

Chapter 3: High-Throughput surface characterization to identify porosity defects

---

This chapter introduces the high throughput surface characterization to rapidly measure the surface roughness and study the melt pool tracks of hundreds of as-fabricated components. A unique correlation between surface characteristics and porosities was observed. This approach helped in identifying the internal porosity defects i.e., lack of fusion, balling, and keyholing. The experimental data and results presented in this chapter have been published in the following work:

- A.K. Agrawal, D.J. Thoma, High-throughput surface characterization to identify porosity defects in additively manufactured 316L stainless steel, Addit. Manuf. Lett. 3 (2022) 100093. doi:10.1016/j.addlet.2022.100093.

In section 3.6, the effect of laser polishing on fatigue behavior is presented. My role was to fabricate fatigue samples, perform fatigue experiments, data generation and analysis. The collaborators at Bremer Institut für Angewandte Strahltechnik (BIAS), Germany performed the laser polishing on the cylindrical surfaces. Other collaborators at the University of Wisconsin-Madison led and planned the experimental project. The experimental data and results presented in section 3.6 have been published in the following work:

- P.J. Faue, L.H. Beste, B. Richter, A. Agrawal, K. Klingbeil, D. Thoma, T. Radel, F.E. Pfefferkorn, Influence of laser polishing on fatigue life of conventionally machined and laser powder bed fusion 316L stainless steel, Manuf. Lett. 33 (2022) 670–677. doi:10.1016/j.mfglet.2022.07.083.

As discussed in the previous section 1.3, porosity defects depend upon the melt pool geometry and melt pool overlapping. Thus, a careful examination of the melt pool tracks can provide insights into different processing regimes.

3.1 Introduction

Prior studies have linked surface characteristics to printability during additive manufacturing. For example, studies of single-line tracks revealed the transition from a conduction to a keyhole mode of heat transfer at higher input energy density which resulted in higher melt pool penetration [53,115]. In-situ x-ray techniques showed increased melt pool depth can lead to sudden melt pool collapse and keyhole porosity formation [58,116]. In a recent study [56], the morphology of the single line track was evaluated at different scanning speeds. High scanning speeds showed discontinuity in the melt pool beads. In addition to single track analyses, studies have focused on the effect of the processing parameters and spatter particles on the surface roughness of the as-fabricated components [117–119]. Based on a statistical analysis, the scanning speed showed the highest influence on the surface roughness followed by laser power and hatch spacing [117]. A rough surface acts as a stress concentration site during mechanical testing. A machine-learning algorithm has been applied to predict the stress concentration of a rough AM surface [120]. The high-cycle fatigue life of AM 304L stainless steel showed a synergistic effect of surface roughness, porosity, residual stress, and microstructure [121], and a reduction in surface defects improved fatigue life. In another recent study [122], laser polishing was used to improve the surface quality during the post-processing of AM 316L stainless steel. The laser polishing and remelting of the top surface reduced the surface roughness by 86% and improved the strength and ductility of the material [122]. A theoretical analysis of the surface profile showed the effects of the melt pool's width, the slope of the melt pool's curve surface, and the melt pool's overlap on the surface roughness [123].

Since the surface morphology and roughness are linked to melt pool characteristics, the occurrence of processing defects, and the resultant mechanical properties, a fundamental

methodology to efficiently investigate the surface characteristics was conducted. In this study, a high-throughput (HT) surface characterization was used to quickly identify the optimal processing conditions for additively manufactured (AM) 316L stainless steel. Hex nut-shaped samples were fabricated at varying combinations of laser power, scanning speed, and hatch spacing. HT surface characterization enabled rapid quantification of the roughness variation. Since the melt pool tracks at the top surface of the AM part are preserved during fabrication, the roughness variation provided direct linkages to the internal porosity defects. Each of the processing regimes (lack-of-fusion, balling, keyhole, and optimal) showed a unique surface signature which permitted the identification of the alloy's processing bounds. Mechanical responses were evaluated for the samples from different processing regimes to quantify the impact of defining the regimes on mechanical properties. The HT approach accelerates the process parameter discovery for the LPBF process. This approach can be applied to quickly define the best processing conditions for any alloy system.

3.2 Experimental procedure

The pre-alloyed 316L stainless steel (SS) feedstock powders having a powder particle size of 15-40 µm were supplied by EOS GmbH, Germany. The chemical analysis of these powders was Ni: 13.94%, Cr: 18.39%, Mo: 2.86%, Mn: 1.47%, Si: 0.3%, and Fe: balance. Wrought 316L SS base plates were thoroughly cleaned and preheated to 80 ˚C prior for sample fabrication.

The HT fabrication of 316L SS was carried out as detailed in a previous study [124]. In short, an EOS M290 system equipped with a 400 W Ytterbium fiber laser source (wavelength = 1060 nm) was used to print 83 hex nut-shaped specimens (Figure 14). Each specimen was processed at different processing conditions covering a wide range of processing space as shown

in Table 3. The up-skin, down-skin, and contour parameters were turned off to preserve the as-fabricated surface features. Other processing variables were kept constant such as layer thickness = 0.02 mm, laser spot size = 100 µm, scan rotation = 67 degrees, and stripe thickness = 5 mm, etc. The porous support structure was fabricated using the factory's default settings. Porous support structures permitted easy extraction of the sample simply by twisting them using a socket wrench. On a different build plate, flat dog bone shape sub-size tensile specimens (ASTM standard [125]) were fabricated with a gauge length and width of 25 mm and 6 mm, respectively (Appendix 1). These specimens were directly printed on the build plate. Wire electrical discharge machining (Wire-EDM) was used to remove them from the build plate.

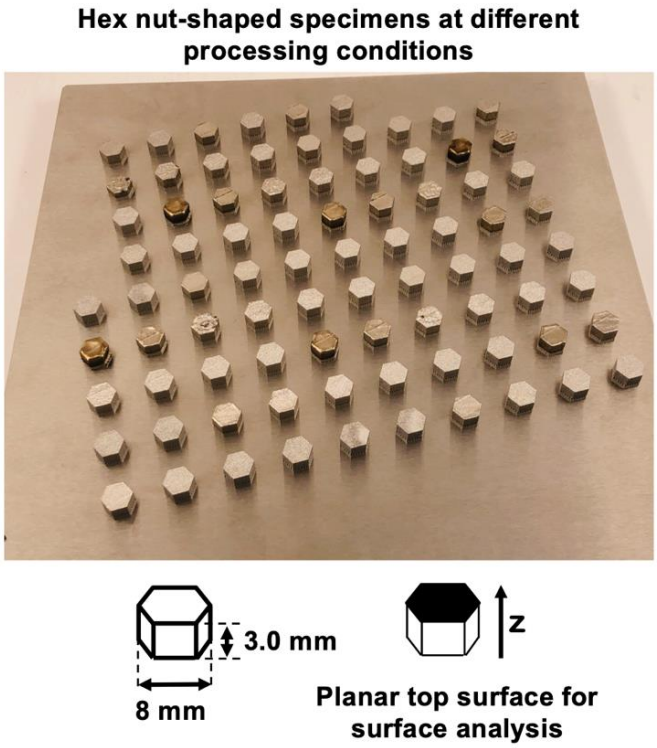

Figure 14. High-throughput (HT) fabrication of additively manufactured 316L stainless steel samples. Surface measurements were performed on the top as-fabricated surface of these hex nut-shaped specimens.

Table 3. Range of processing variables for the HT fabrication

	Laser power	Scanning speed	Hatch spacing
Process range	100 to 350 W	600-2000 mm/s	0.09-0.11 mm

The HT surface measurements of the as-fabricated sample's top surface were performed using a Bruker Alicona (Infinite focus G4) optical 3D measurements system. As-fabricated samples were individually scanned at 10x zoom with a lateral resolution of 2 µm and a vertical resolution of 50 nm. A waviness filter of 250 µm was applied to calculate the average surface roughness (S_a) values. A sufficiently large section of top surface area was scanned to evaluate surface roughness and minimize the effects of spattering and any local disturbance in powder bed. The surface roughness value represents the average deviation in z-height from the mean surface at each pixel point and can be calculated by:

$$S_a = \frac{1}{A}\iint |Z_{x,y}| dxdy \tag{11}$$

HT density measurements of the samples were carried out using an immersion-based technique [124]. Each specimen's dry mass and the wet mass (while freely suspended in the Fluorinert™ FC-40 solution (3M, St. Paul, MN)) were measured to calculate the density. For measuring the density, ASTM Standard B962 was followed [108]. The relative density (%) was calculated by normalizing the density values obtained from all the specimens.

Scanning electron microscopy (SEM) imaging for a reduced number of selected samples was performed. A ZEISS Leo 1530 FEG-SEM system was used for imaging as-fabricated top and cross-sectional surfaces. For cross-section imaging of defects and porosities, samples were

sectioned and conventional metallographic practices including mechanical grinding and polishing were performed.

Tensile testing of samples was performed using an MTS Sintech load frame equipped with a 50 KN load cell. The strain rate for the test was kept constant at 0.01 s^{-1}. The processing parameters for these samples are shown in Table 5. At least two tests per sample condition were performed to get an average value. Strain values were recorded using a non-contact data image correlation (DIC) method. Prior to testing, speckle patterns on the sample surface were created by spraying black paint over the white color background. Analysis of the DIC patterns was done using the Zeiss GOM correlate software package.

3.3 High throughput surface measurements

A total of 83 hex nut-shaped samples were fabricated at a varying combination of laser power, scanning speed, and hatch spacing since these variables have a direct influence on the amount of energy supplied and the rate of material deposition. The total processing time of the samples was approximately 8 hours. These samples were placed randomly on the build plate without any site preference for any processing conditions. The processing parameters for the HT experiments were designed based on a dimensionless number. The dimensionless number (π) can be expressed in terms of materials property as [114,126]:

$$\pi = \frac{C_p P}{K V^2 H} \tag{12}$$

where P is laser power (W), V is scanning speed (m/s), H is hatch spacing (m), K is thermal conductivity (W/mK) and C_p is specific heat (J/kgK). In the present study, a wide range of processing space covering π values from 7.5 to 350 was explored.

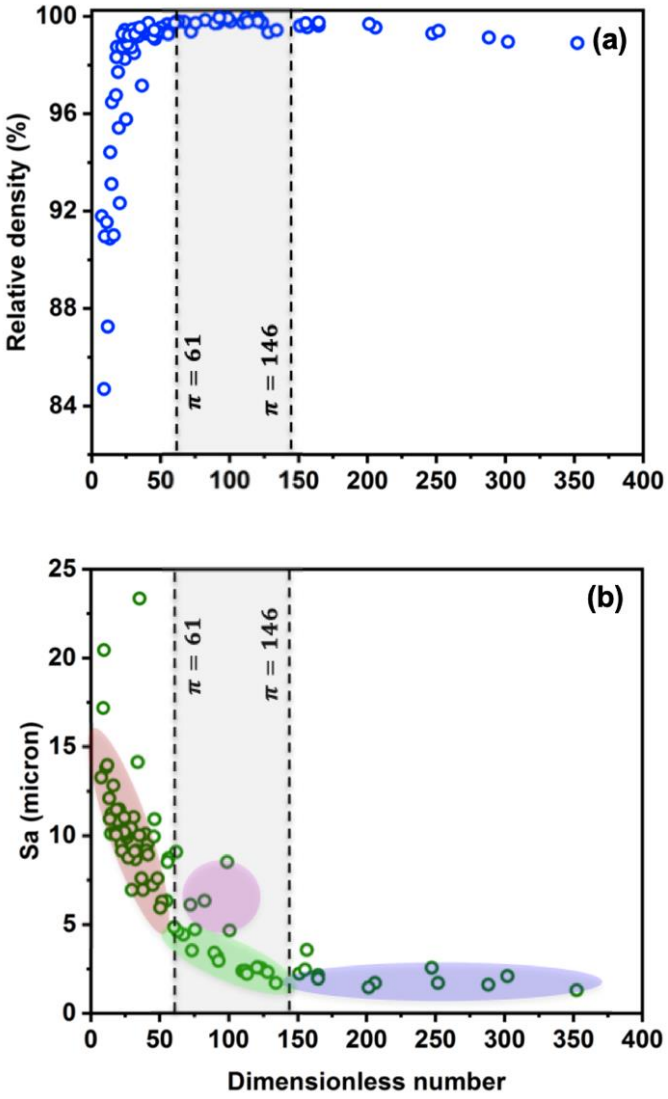

Figure 15. High-throughput (a) density and (b) surface measurements of as-fabricated 316L stainless steel samples. HT experiments provided rapid identification of the processing bounds for lack-of-fusion, balling, keyhole, and optimal regions.

The HT density and surface measurements of the hex nut-shaped samples were performed in approximately 3 and 7 hours, respectively. Both relative density and surface roughness showed a strong correlation with the dimensionless number as shown in Figure 15. The graph can be divided into three gradually transitioning regimes, potentially suggesting the different defect regimes: lack-of-fusion, keyhole, and intermediate. In the lack-of-fusion regime ($\pi<61$), insufficient energy was supplied resulting in low density and high surface roughness. The density value increases from 84% to 99%. The surface roughness decreases from 23 to 5.3 µm, suggesting the roughness decreases with a decreasing amount of lack-of-fusion porosity. In the keyhole regime ($\pi>146$), an excess amount of energy is supplied. Keyhole porosity increases with increasing dimensionless number and results in a density decrease. In this regime, a relatively smooth surface was obtained, with the surface roughness being approximately 2 to 4 µm. Similar trends in HT density measurements are reported in previous studies [114,124]. In the intermediate regime ($61<\pi<146$), high density samples were obtained. However, there exists a transition in the surface roughness. Surface roughness gradually decreases from 5 to 2 µm with the dimensionless number as highlighted by the green region. However, a few samples delineate from the gradual decrement and have a higher roughness of more than 5 µm (as highlighted by the pink region). Since all samples in the pink region were fabricated at higher laser power, it was considered possible that the variation in surface roughness could be connected to balling. Thus, the intermediate region can be subcategorized into two parts: (i) a balling regime associated with high roughness ($S_a>5$ µm) and (ii) an optimal regime associated with low roughness ($S_a<5$ µm).

To further investigate the proposed defect regimes suggested by the HT density and surface measurements, analytical models and low throughput characterizations were used. Multiple analytical models to estimate the melt pool geometry and processing regime are available in the

literature [91,127,128]. A combination of these models were used to generate the predictive processing maps for the LPBF process [128] and for detailed discussion refer to the Chapter 3:. The predictive power-velocity (PV) map for 316L SS at a constant hatch spacing of 0.11 mm and a layer thickness of 0.02 mm is shown in Figure 16. The PV map shows the estimates of the different processing regimes: keyhole (blue), balling (pink), lack-of-fusion (red), and optimal (green). The white region represents the transition regions. The estimates from the analytical model are consistent with the HT experiments. Four processing conditions, one from each processing regime, were selected for surface imaging (from the hex-nut fabrication) and mechanical testing as shown in Figure 16 (black circle points).

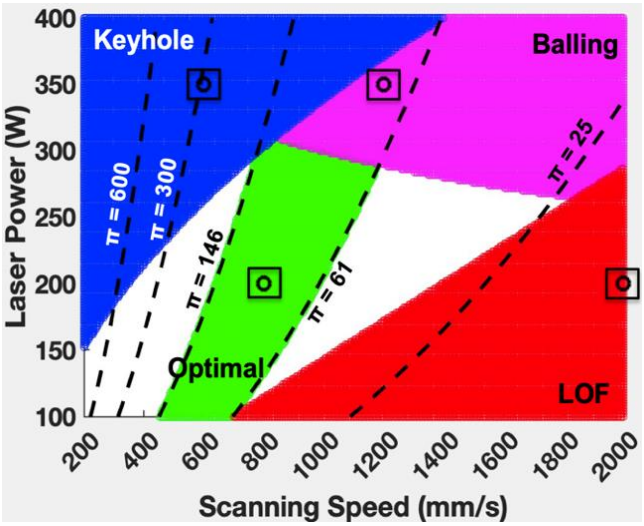

Figure 16. Predictive PV processing maps for 316L stainless steel showing the estimates for different processing regime: keyhole (blue), balling (pink), lack of fusion (red), and optimal (green). The estimates for different processing regimes were calculated using analytical equations [128]. The white region represents the transition regions. Black circle represents the samples selected from each processing regime.

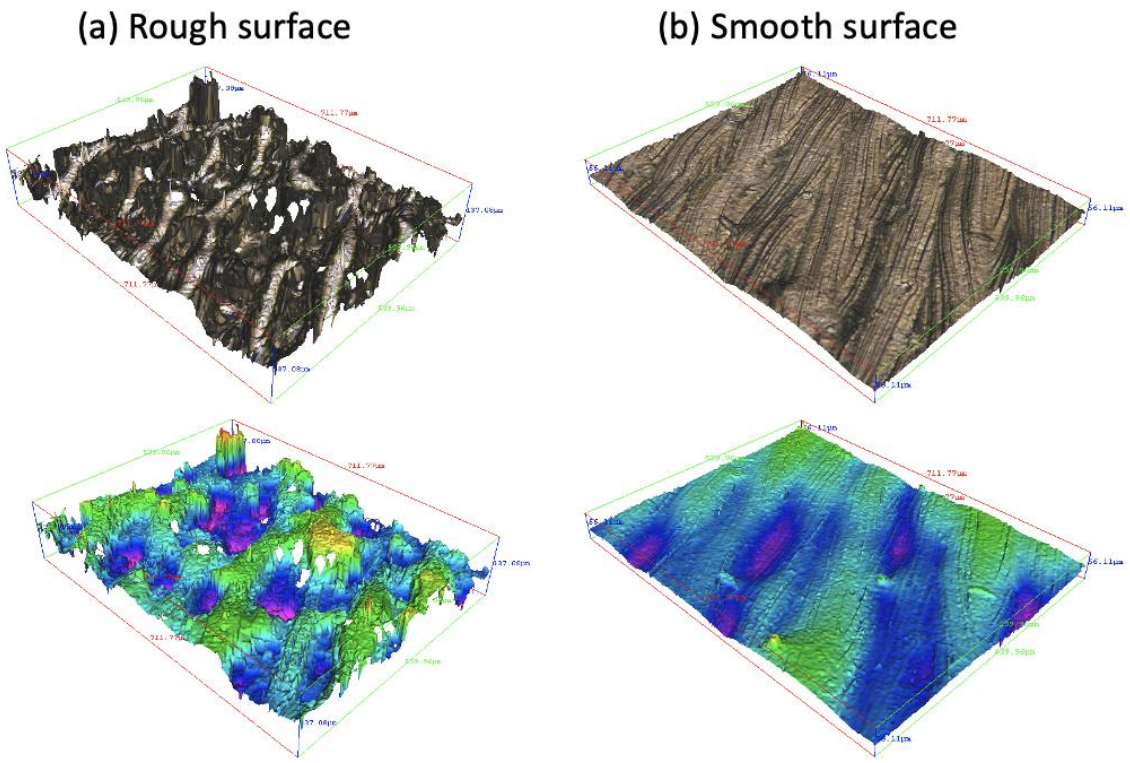

Figure 17. As-fabricated surface profile of the (a) lack of fusion showing high surface roughness and (b) optimal sample showing smooth surface

Table 4. Summary of the surface characteristics for the samples from different processing regime

Sample	Dimensionless number (π)	Surface roughness (Sa)	Melt pool tracks
Lack of fusion	$\pi < 61$	Sa > 5 µm	Cavities in between
Optimal	$61 < \pi < 146$	Sa < 5 µm	Uniform & no cavities
Balling	$61 < \pi < 146$	Sa > 5 µm	Non uniform width
Keyhole	$\pi > 146$	Sa < 5 µm	Curved tracks

Surface profiles of the lack of fusion and optimal sample is shown in Figure 17. The lack of fusion sample (π=15) showed rough surface with deep valleys near the melt pool tracks. In case of optimal region (π=93) the surface showed smooth surface. The variation in the surface profiles supports the correlation between the surface roughness and internal porosity defects

3.4 Correlation between surface roughness and internal porosities

Each processing regime i.e., lack-of-fusion, balling, keyhole, and optimal shows a unique surface characteristic. SEM images of the sample's top and cross-sectional surfaces from the different processing regions are shown in Figure 18. In the case of lack of fusion (π=15), the width of melt pool tracks is smaller than the hatch spacing. The insufficient overlapping of the melt pool tracks causes cavity and pore formation in between melt pool tracks. These pores are irregular in shape with a size of approximately 100 µm and lie in the vicinity of the melt pool boundaries. These surface characteristics align with the HT measurements as shown in Figure 15. The width of the melt pool track increases with the energy supply [81,129]. Therefore, as the dimensionless number increases, fewer cavities and porosities form between the melt pool tracks and the relative density increases. In the case of balling (π=72), the melt pool tracks are of irregular width. A spherical hump along the melt pool tracks can be observed. These humps are about twice the width of the melt pool tracks. Balling porosities are elongated towards the building direction and have high aspect ratios. Similar surface features were observed for all the samples in the pink region as shown in Figure 15b confirming the hypothesis of balling porosities in the intermediate region ($61<\pi<146$) and high surface roughness (S_a>5µm). In the case of the keyhole region (π=288), the sample surface is much smoother with minimal powder particles on the top surface. The melt pool tracks have curvature, possibly due to the high thermal stress and excess energy supply. Keyhole

pores are spherical in shape with an average size of around 50 µm. In the case of the optimal regime (π=93), the melt pool tracks are of uniform width with sufficient overlapping. The cross-section images are dense and defect-free. The melt pool trail-end marks are observed in the optimal regime, possibly because of the smooth surface and optimal heat supply providing a distinct surface signature.

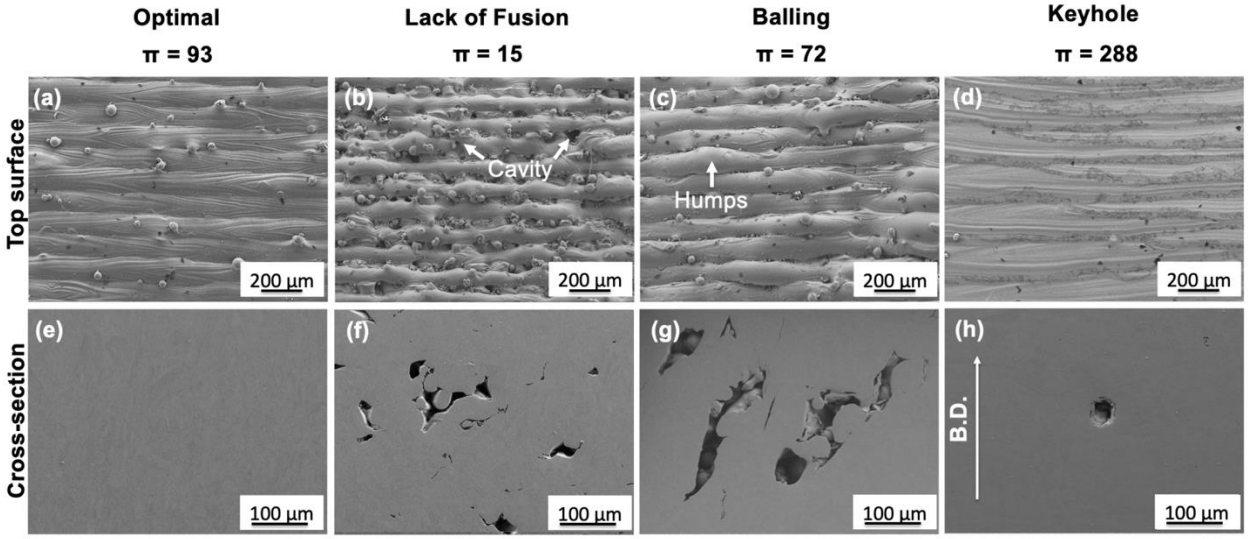

Figure 18. SEM images of top surfaces (a-d) and the cross-sectional surfaces (e-h) of the 316L stainless steel samples. Each porosity defects show unique surface characteristics.

A summary of the surface characteristics for different processing regimes is shown in Table 4 and to illustrate a schematic diagram of the findings is drawn in Figure 19. The criterion used to describe different processing regimes is a reduced order approximation and uncertainty exists during a gradual transition between the processing regimes.

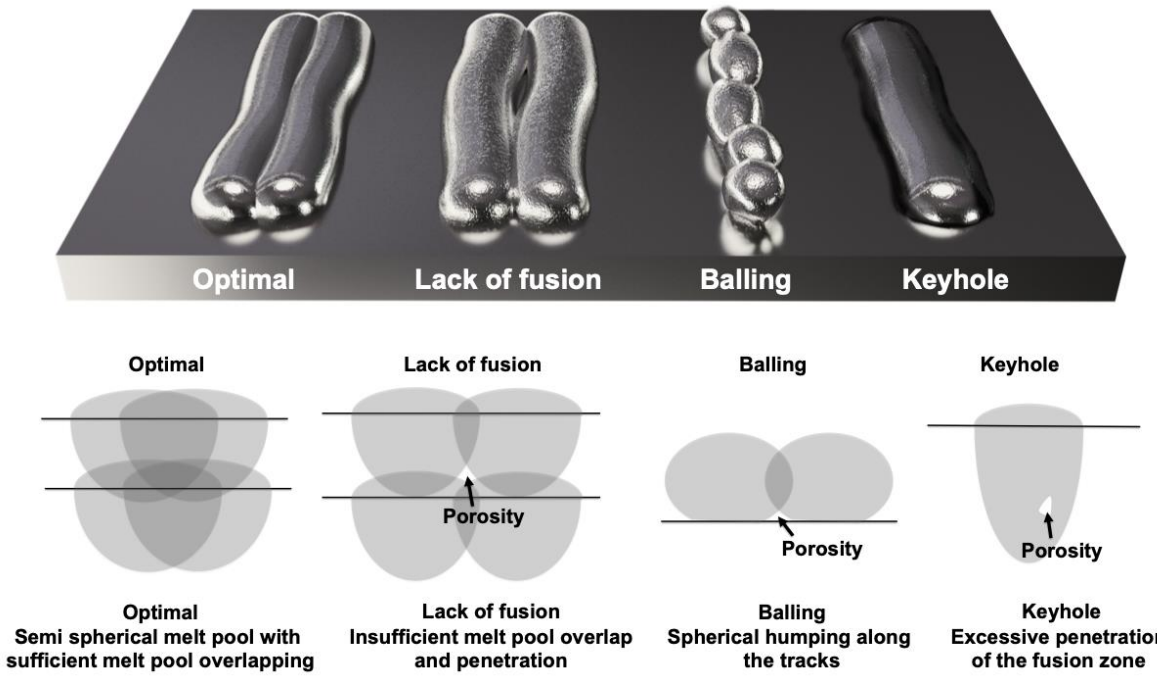

Figure 19. Schematic diagram showcasing the dependence between the surface roughness and the porosity defects

In general, the HT surface methodology works for the processing defects related to the melt pool track morphology such as lack-of-fusion, balling, and keyhole. A similar approach can be applied to identify the processing regions and minimize porosity defects for other alloy systems. However, the surface evaluation doesn't provide any information about the solidification cracks which are more dependent upon the solidification conditions and material shrinkage. Thus, for a crack-prone alloys, HT surface methodology will provide limited information and further steps would be required to mitigate the solidification cracks. It would also be interesting to study the effect of scan strategies and other key processing parameters on surface characteristics of additively manufactured components.

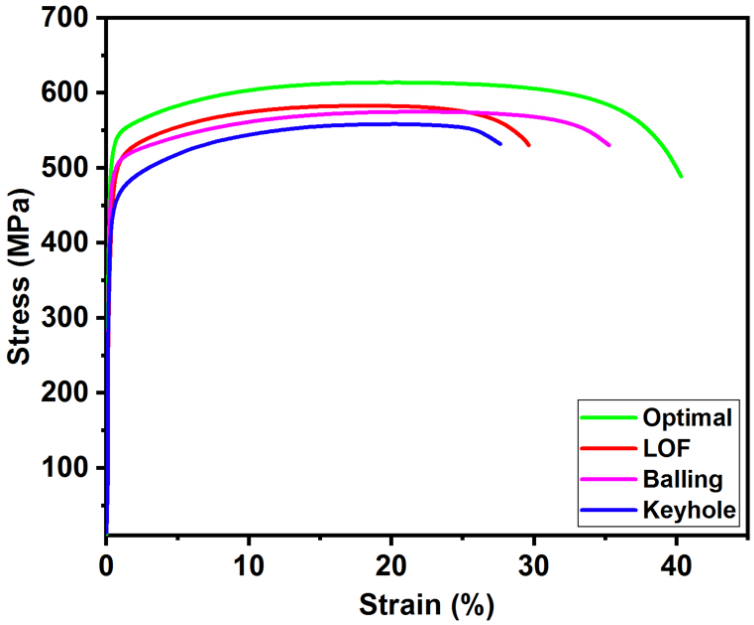

Figure 20. Engineering stress-strain curves of the as fabricated 316L stainless steel samples from different processing regime. Optimal condition (green) shows better strength and ductility over the samples from LOF (red), Balling (pink), and Keyhole (blue).

3.5 Mechanical response

The significance of developing HT methods to define optimal process parameters can be illustrated through mechanical testing. Mechanical responses of the as-fabricated samples from different processing regions were evaluated as shown in Figure 20 and Table 5. The samples with optimal processing conditions showed a tensile strength and ductility of 614 MPa and 40% respectively. An improvement of approximately 30% ductility and 10% tensile strength over the sample with porosity defects signifies the importance of optimizing the alloy's processing conditions for an alloy. Noticeably, the yield strength for the lack-of-fusion sample is higher than the keyhole sample despite having sharp pores and poor surface roughness (S_a>5µm). Recent studies illustrate that the microstructure coarsens with increasing energy supply [124,130–132].

Finer grain size and solidification features possibly contributed to higher yield strength in the lack-of-fusion samples [62,133]. Nonetheless, processing defects clearly alter the strength and ductility, and microstructural optimization may be required within the optimal process window.

Table 5. Summary of the tensile data for the samples from different processing regime.

Sample	Laser power (W)	Scanning speed (mm/s)	Dimensionless number	Yield strength (MPa)	Tensile strength (MPa)	Ductility (%)
Optimal	200	800	93	524 ± 16	614 ± 19	40 ± 1
LOF	200	2000	15	488 ± 19	575 ± 18	29 ± 2
Balling	350	1200	72	473 ± 22	583 ± 20	34 ± 1
Keyhole	350	600	288	433± 18	558 ± 17	28 ± 2

3.6 Influence of laser polishing on fatigue life

Laser polishing is a contact-free and volume-neutral alternative to traditional methods like mechanical or chemical polishing. In the case of laser polishing, the scanning laser remelts the top layer of the sample and solidifies it into a smooth surface. Laser polishing has been shown to be an effective method for reducing the surface roughness of metal surfaces [134,135]. In addition to modifying the surface roughness, laser polishing has also been found to change the microstructure and surface mechanical properties following processing [136,137]. The rapid solidification that occurs during laser polishing can result in finer, equiaxed grains when applied to additive components with an initial columnar microstructure [136].

In the work, the gauge section of the fatigue samples was laser polished using Raylase Superscan III-15, Bremen, Germany [138]. The incident beam diameter at the material surface was 120 µm during laser polishing. The laser was operated in continuous wave mode with a power of 34 W. The beam was scanned across the surface at a processing speed of 100 mm/s. The scanning strategy used to polish the fatigue samples consisted of 8 discrete scan fields incremented around the samples' circumference. Each scan field consisted of the line passes parallel to the rotational axis of the fatigue sample with an overlap between consecutive passes equal to 60% of the beam diameter. A dual pass polishing strategy described in Figure 21 was used to reduce the effects of the overlapping scan fields. Other goals of the scanning strategy were to effectively distribute heat input in space and time as well as reduce the effects of process artifacts at the start and stop of a single line pass by starting/stopping the line at a point on the sample beyond the gauge section where the diameter starts to increase. The heat input was spread out in time by waiting 60 seconds between the start of consecutive scan fields.

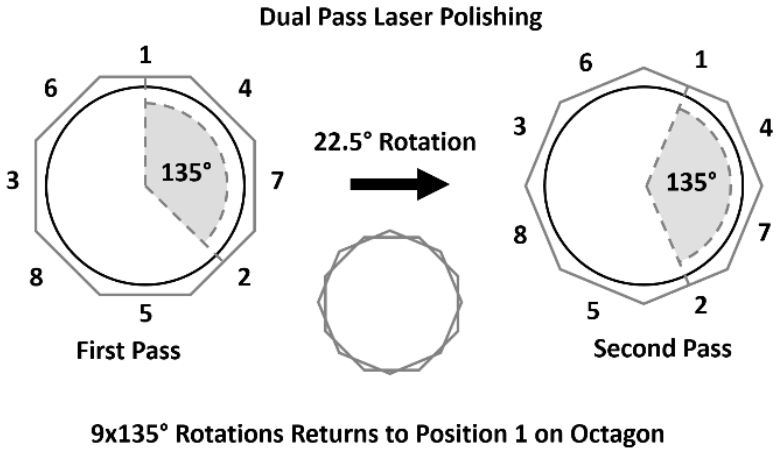

Figure 21. Dual pass scanning strategy using eight discrete scan fields.

Table 6. Roughness of the cylindrical samples before and after laser polishing

Roughness	LPBF-manufactured	Laser polished
Mean arithmetical height (R_a)	10.94 µm	4.85 µm
Mean surface roughness (S_a)	35.83 µm	10.99 µm

Roughness values of the samples before and after laser polishing are shown in Table 6. The mean arithmetical height, Ra, reduced from 10.94 µm to 4.85 µm and the mean surface roughness, Sa, reduced from 35.83 µm to 10.99 µm because of laser polishing. Approximately, laser polishing remelted the sample top layer with the remelt depth and the remelt width was 28.7 ± 2.1 µm and 78.1 ± 6.2 µm respectively [138]. It can be observed that the laser polishing process was able to effectively reduce spatial wavelength across the entire roughness spectrum for the samples.

The effects of laser polishing on the S-N curve and fatigue life are shown in Figure 22. No improvement in the fatigue life was observed for the stress amplitude of 225 and 300 MPa despite lowering the surface roughness by about 60%. This indicates that roughness is not the only major contributing factor to the fatigue life of metal AM components and the resulting fatigue life of AM parts, whether laser polished or not, is largely due to other properties including but not limited to microstructure, internal porosity, or residual stress. Only in the case of the lowest stress amplitude of 150 MPa an improvement in fatigue life waw observed suggesting only at the lower stress levels and high fatigue cycles, roughness becomes a dominant mode of fatigue failure.

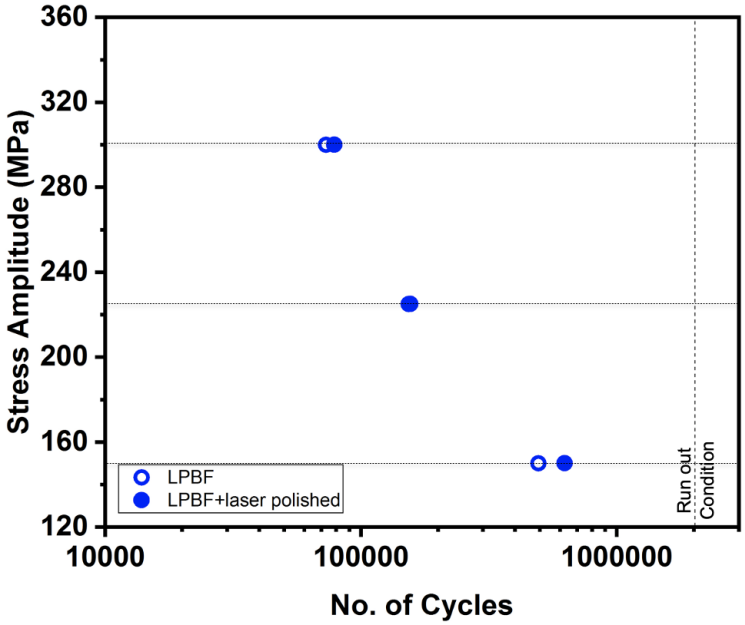

Figure 22. S-N curve of 316L stainless steel samples showing fatigue life of as-build LPBF samples and laser polished samples [138].

3.7 Conclusion

In summary, a high-throughput surface characterization approach was used for rapid process parameter discovery of additively manufactured (AM) 316L stainless steel. Based on the results and analysis, the following conclusions can be reached:

1) The high-throughput surface measurements can be applied to quickly identify the processing offsets for lack-of-fusion, balling, and keyhole regions. The time estimation for HT fabrication and characterization of 83 AM samples is 18 hours.
2) Surface features correlate to internal porosity defects. Cavities in between the melt pool tracks showed the presence of lack-of-fusion porosity. A non-uniform width of the melt

pool track is the characteristic feature for balling porosities. Slight curvatures in the melt pool tracks are related to keyhole porosities.

3) Samples processed at optimal processing a condition showed a 30% ductility improvement and 10% yield strength improvement over the samples containing porosity defects illustrating the importance of defining defect regimes in the LPBF process.

Laser polishing and fatigue studies of the 316L stainless steel were performed. Overall, laser polishing helped in reducing the surface roughness of the cylindrical section by 60%. At high stress amplitudes of 225 and 300 MPa no improvement in fatigue life was observed. Marginal improvement was observed at the lowest stress amplitude of 150 MPa suggesting microstructure, internal porosity, or residual stress to be the major factor influencing fatigue life.

Chapter 4: Predictive processing maps: an analytical approach

---

This chapter provides a framework to predict and visualize processing maps of additively manufactured materials based on the existing analytical models. The analytical approach provides a quick estimate with a total computing time of fewer than 5 mins. This approach can be applied to different alloy systems given that the material's thermophysical properties are provided. The predictive model and discussions presented in this chapter have been published in the following work:

- A.K. Agrawal, B. Rankouhi, D.J. Thoma, Predictive process mapping for laser powder bed fusion: A review of existing analytical solutions, Curr. Opin. Solid State Mater. Sci. 26 (2022) 101024. doi:10.1016/j.cossms.2022.101024.

4.1 Introduction

In this chapter, we aim to combine existing analytical models and porosity defect criteria to rapidly generate PV processing maps and compare them with experimental data from the literature. We especially aim to predict the PV processing window for the LPBF process as a function of hatch spacing, layer thickness, and material properties.

The general theme of the chapter is presented in Figure 23. Laser processing parameters and materials properties serve as input variables to construct the LPBF processing map. These sets of input variables are either constant for a given material (like materials properties) or can be independently controlled (like laser parameters) during LPBF processing. The only exception is the laser absorption coefficient which can vary with powder size distribution. A brief discussion on the input parameters and how these variables affect the laser-metal interaction as discussed in

the earlier section 1.2. Several design parameters and dimensionless numbers have been developed to correlate the processing parameters and describe various aspects of the LPBF process. A comparison of these commonly used design parameters along with their strength and limitations is presented in section 4.2. In section 4.3, different analytical models available in the literature are presented to quickly estimate the melt pool geometry including melt pool width, depth, and length. Control over the melt pool is crucial, if porosity defects in AM components are to be avoided. The evaluation in section 4.4 discusses how the melt pool geometry affects porosity and details the existing defect criteria for lack-of-fusion, under-melting, balling, and keyholing regions. In section 4.5, additional analytical models and dimensionless numbers are discussed highlighting the dependence of laser-metal interaction on compositional changes, thermal strain, depression zone, solidification cracking, and as-solidified microstructure. The estimates of melt pool geometry and defect criteria were combined to construct and compare the LPBF processing maps for different materials. Finally, the processing maps predictions are then compared with existing experimental data gathered from the literature to provide an assessment of the predictive capability of these maps. These results are presented in section 4.6.

This chapter offers three benefits: (i) a critical review of the analytical models available in the literature, (ii) an insight into different porosity defects and strategies to mitigate them, and (iii) a predictive tool that serves as a feedback loop to quickly identify the LPBF processing window.

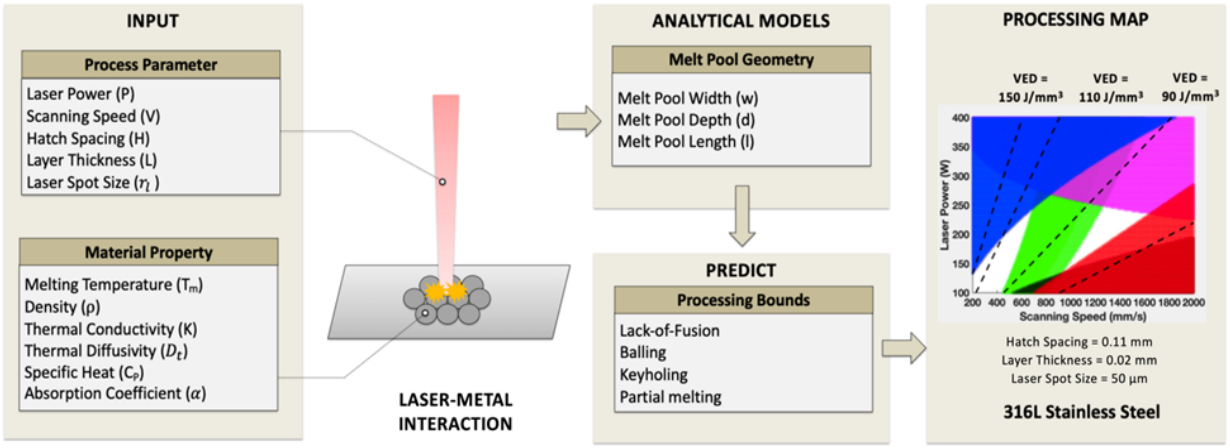

Figure 23. The general theme of chapter. A set of process parameters and materials properties were selected as an input variable to predict the melt pool geometry and LPBF processing bounds of a material.

4.2 Design parameters

The material properties and LPBF processing parameters combine to form a large set of input parameter required for fabricating components. Design methodologies to condense the multiple input parameters into physically significant relationships for evaluating the LPBF process have been explored and will be presented. Please note that millimeter is often used to reflect the length scale in energy density terms introduced below. In more derived analytical expressions introduced later in the text, the standard SI unit of meters is used. The difference is purely a matter of convenience.

4.2.1 Energy density

Multiple energy density-based parameters are proposed to provide the combined effects of laser parameters. These design parameters are helpful in visualizing and optimizing the processing conditions. Some of the commonly used energy density parameters are:

a) Linear energy density (LED) gives the amount of the input energy supplied over a laser distance (in J/mm). In this case, the laser beam is considered as a point heat source. This parameter correlates laser power and scanning speed and can be expressed as:

$$\text{Linear Energy Density (LED)} = \frac{\text{P}}{\text{V}} \tag{13}$$

where *P* is laser power (W), and *V* is scanning speed (mm/s).

b) Areal energy density (AED) is a modified version of the LED where the laser spot radius is incorporated to estimate the energy spread over the unit area (in J/mm^2). AED correlates all three laser parameters using the following equation:

$$\text{Areal Energy Density (AED)} = \frac{\text{P}}{\text{V}\text{r}_\text{l}} \tag{14}$$

where *P* is laser power (W), *V* is scanning speed (mm/s), and r_l is laser spot radius (mm).

c) Volumetric energy density (VED) gives the information about energy supplied per unit volume (in J/mm^3). This parameter accounts for the total energy supplied to a local region including the additional energy supplied during heating cycles. Therefore, hatch spacing and layer thickness are used in the equation to provide a better approximation of the process input parameters. VED can be calculated as:

$$\text{Volumetric Energy Density (VED)} = \frac{\text{P}}{\text{VHL}} \tag{15}$$

where *P* is laser power (W), *V* is scanning speed (mm/s), *H* is hatch spacing (mm), and *L* is layer thickness (mm).

d) Specific energy density (SED) is a modified version of VED where instead of using hatch spacing and layer thickness values, actual melt pool dimensions were considered. To a certain degree, SED provides a better approximation of the energy supplied (in J/mm^3) since the melt pool geometry can vary locally along the build direction [13]. However, using SED as a design parameter can be challenging since melt pool geometry is difficult to measure *in situ* and it is not an independently controlled processing variable. SED can be calculated in terms of melt pool width and melt pool depth as:

$$\text{Specific Energy Density (SED)} = \frac{\text{P}}{\text{Vwd}} \tag{16}$$

where P is laser power (W), V is scanning speed (mm/s), w is melt pool width (mm), and d is melt pool depth (mm).

Out of all four, VED is a widely accepted design parameter by the AM community because of its simplicity. Some studies have shown a correlation between microstructure and VED [124,130]. In contrast, other studies have shown part's density variation even for the same VED [109]. Comparing the results from different studies suggests that the VED can be considered as a reliable parameter only within a certain laser power and scanning speed range. At extremely high or extremely low VED values, individual effects from laser power or scanning speed can have a dominating effect on printability.

4.2.2 Normalized enthalpy

Normalized enthalpy is an alternate design parameter used by the AM community. This parameter was first developed for welding processes and was later modified for the AM process

[53]. Normalized enthalpy has a few merits over energy density. It combines both material properties and laser parameters which are essential for describing the laser-metal interaction. In a recent study, normalized enthalpy combined with FEM models were used to translate the optimal processing parameter from one alloy to another [139]. Another study has shown a dependence between the normalized enthalpy and melt pool depth [53]. Thus, the conduction to keyhole mode heat transfer can be estimated using this parameter. Normalized enthalpy can be calculated using the following equation:

$$\frac{\Delta H}{H_s} = \frac{\alpha P}{\pi H_s \sqrt{D_t V r_l^3}} = \frac{\alpha P}{\pi \rho C_p T_m \sqrt{D_t V r_l^3}} \tag{17}$$

where P is laser power (W), V is scanning speed (m/s), r_l is laser spot radius (m), T_m is melting temperature (K), ρ is density (kg/m^3), C_p is specific heat (J/kgK), D_t is thermal diffusivity (m^2/s), and α is laser absorptivity. However, unlike energy density, normalized enthalpy does not account for hatch spacing or layer thickness. In other words, this parameter will not provide any information about defects such as lack of fusion, which are heavily dependent upon the melt pool layers overlapping. Also, the normalized enthalpy depends on the laser absorption coefficient which can be challenging to measure experimentally.

4.2.3 Dimensionless numbers

Dimensionless numbers are derived from dimensional analyses using the Buckingham Pi theorem [111]. Some of the popular dimensionless numbers relevant to AM processes are the Fourier number, the Peclet number, the Marangoni number, the Stefan number, the Weber number, and the non-dimensional heat input, etc. [113]. The Fourier number provides information about

the rate of heat dissipated with respect to the rate of heat stored in the part. The Fourier number can be expressed as:

$$\mathrm{Fo} = \frac{\mathrm{D_t}\tau}{\mathrm{l^2}} = \frac{\mathrm{D_t}}{\mathrm{Vl}} \tag{18}$$

where, D_t is thermal diffusivity (m^2/s), τ is characteristic time (s), l is melt pool length (m), and V is scanning speed (m/s). A higher value of the Fourier number is desirable to reduce heat storage, thermal strain, and residual stress. The Peclet number is defined as:

$$\mathrm{Pe} = \frac{\mathrm{U_{max}L_c}}{\mathrm{D_t}} \tag{19}$$

where, D_t is thermal diffusivity (m^2/s), U_{max} is the maximum velocity of molten metal inside the fusion zone (m/s), and L_c is the characteristic length such as length or width of the melt pool (m). At a lower Peclet number, the conduction mode of heat transfer is dominant, while at a higher Peclet number, the convective mode of heat transfer starts to dominate. Similarly, other dimensionless numbers provide information such as melting efficiency, capillary effects, and extent of the Marangoni effects within the melt pool [50,113]. However, most of these dimensionless numbers cannot be used as a sole design parameter to identify the processing window of the LPBF process. In a recent study by Rankouhi *et al.* [114], a dimensionless energy density was used for determining the processing window for the LPBF process. The dimensionless energy density can be expressed in terms of materials properties and laser parameters as:

$$E_{dim} = \frac{C_p P}{KV^2 H} \tag{20}$$

where P is laser power (W), V is scanning speed (m/s), H is hatch spacing (m), K is thermal conductivity (W/mK) and C_p is specific heat (J/kgK). There are two major benefits of using dimensionless energy density as a design parameter. First, it can be applied to translate the optimal processing parameters across different materials or LPBF systems. Second, all the variables needed to calculate the dimensionless energy density are either material's constant or independently controlled process variables.

It is also interesting to compare the three design parameters from eq. (15, (17, and (20 with respect to P and V. Each design parameter can be expressed as a function of P and $1/V^n$ i.e.:

$$\text{Design parameters} \propto \frac{P}{V^n} \tag{21}$$

For $n = 1$, the design parameter is volumetric energy density (linear), for $n = 0.5$ it is normalized enthalpy equation (squared root), and for $n = 2$ it is dimensionless energy density (squared). A schematic diagram of this inter-dependency is shown in Figure 24. However, the LPBF process is complex, and the melt pool dynamics may or may not be fully captured in any of these design parameters depending upon the range of parameters being studied. It is also possible that different design parameters would be appropriate for different ranges of power-velocity combinations. Nevertheless, design parameters are useful for quick approximation and reducing the dimensionality of the LPBF processing variables.

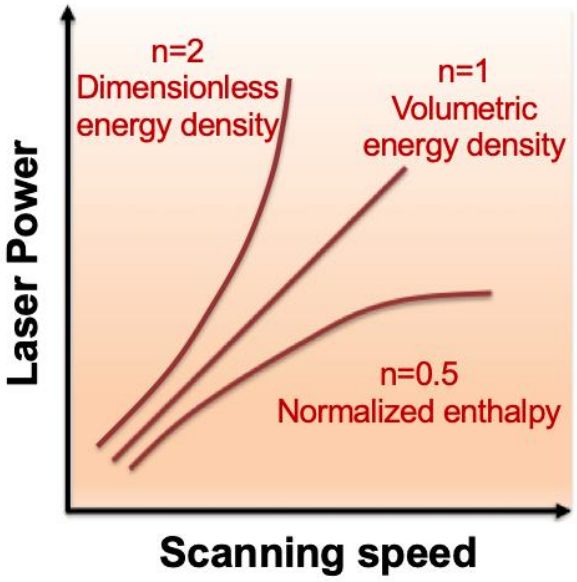

Figure 24. Comparison of the three commonly used design parameters from eq. (15, (17, and (20, showcasing the difference in the inter-dependency between laser power and scanning speed.

4.3 Analytical melt pool models

Upon exposure to the laser energy, the powder's surface temperature rises rapidly. In a localized region, the temperature exceeds the melting temperature forming a melt pool boundary. The supplied heat also raises the temperature in the vicinity of the melt pool. These regions are known as heat-affected zones. The melt pool shape and size have a direct consequence on porosity defects, solidification conditions, and microstructural features. The two governing forces that control the melt pool flow are the Marangoni force and recoil pressure [17,140]. Other forces such as buoyancy force, gravitational force, and Lorentz force have negligible effects on the melt pool flow. The Marangoni force is a thermo-capillary effect that occurs due to large thermal gradients and temperature dependent surface tension [141,142]. It pushes the molten metal to flow from high temperature to low temperature regions, making the melt pool flow vigorously within the fusion

boundary. Recoil pressure originates from the rapid evaporation of alloying elements from the melt pool surface. This force pushes the liquid metal inwards creating a vapor cavity known as vapor depression zone [140]. At a high energy density, the peak temperature, Marangoni force, and recoil pressure increase, leading to an unstable melt pool [58]. Thus, the melt pool geometry can become shallow, deep, or semi-spherical depending on the heat supply and processing variables [81,129].

Techniques such as *in situ* synchrotron x-ray imaging, infrared thermal imaging, FEM simulations, and optical microscopy have been used to study and measure the melt pool geometry and heat distribution. Analytical models use the thermophysical data and processing parameters to estimate the melt pool geometry at given processing conditions. Unlike *in situ* imaging and FEM simulations, these models provide time efficient, computationally inexpensive, and quick approximation of the melt pool geometry. Details of these analytical models based on the Rosenthal equations and scaling laws are discussed below.

4.3.1 Rosenthal equations

Heat distribution in a solid with a moving heat source (e.g. welding processes) can be calculated using the Rosenthal equations [143]. In the study by Tang *et al.* [10] the Rosenthal equations were used to obtain an analytical expression of melt pool geometry i.e., the region for which the local temperature is equal to the alloy's melting temperature. Some of the key assumptions made to derive the analytical equations are: (i) the heat flow is two-dimensional, (ii) there are negligible effects from convective heat transfer i.e., only conductive mode of heat transfer is considered, (iii) the laser beam acts as a point source, (iv) specific heat and thermal conductivity are temperature independent, and (v) the melt pool is semi-elliptical in shape. The width of the melt pool can be expressed as:

$$\text{Width (w)} = \sqrt{\frac{8\alpha P}{\pi e \rho C_p V(T_m - T_o)}} \tag{22}$$

Assuming a semi-elliptical melt pool shape, the melt pool depth can be expressed as:

$$\text{Depth (d)} = \frac{\text{Width (w)}}{2} = \sqrt{\frac{2\alpha P}{\pi e \rho C_p V(T_m - T_o)}} \tag{23}$$

where P is laser power (W), V is scanning speed (m/s), T_m is melting temperature (K), T_o is the far-away temperature (K), assumed to be the build plate temperature, ρ is density (kg/m^3), C_p is specific heat (J/kgK), and α is laser absorptivity.

4.3.2 Scaling laws

In the study by Rubenchik *et al.* [87], a scaling law analysis based on the Egar-Tsai (ET) thermal model was performed to calculate the melt pool geometry. Some of the key model assumptions are: (i) melt flow and thermo-capillary effects are neglected, (ii) the effects of the heat of fusion on temperature distribution is not considered, and (iii) specific heat and thermal conductivity are temperature independent. From this model the melting process can be characterized in terms of two dimensionless numbers p and B. The expression for p and B is given as:

$$p = \frac{D_t}{Vr_l} \tag{24}$$

$$B = \frac{\alpha P}{\pi \rho C_p T_m \sqrt{D_t V r_l^3}} \tag{25}$$

where P is laser power (W), V is scanning speed (m/s), r_l is laser spot radius (m), T_m is melting temperature (K), ρ is density (kg/m^3), C_p is specific heat (J/kgK), D_t is thermal diffusivity (m^2/s), and α is laser absorptivity. The dimensionless number p represents the overall shape of the melt pool, and it is the ratio of the thermal diffusion length to the dwell time. Therefore, a lower value of p means the melt pool is shallow and long. The dimensionless number B represents the ratio of the input laser energy to the enthalpy. For a well-developed melt pool, both p and B have a value greater than 1. The melt pool dimensions including width, depth, and length are defined in terms of dimensionless numbers p and B and can be expressed as:

$$\text{Depth (d)} = \frac{r_l}{\sqrt{p}}\left[\begin{matrix} 0.008 - 0.0048B - 0.047p - 0.099Bp \\ + plnp(0.32 + 0.015B) + lnB(0.0056 - 0.89p + 0.29plnp) \end{matrix}\right] \tag{26}$$

$$\text{Length } (l) = \frac{r_l}{p^2}\left[\begin{matrix} 0.0053 - 0.21pB + 1.3p^2 - (0.11 + 0.17B)\, p^2 lnp \\ + B(-0.0062 + 0.23p + 0.75p^2) \end{matrix}\right] \tag{27}$$

$$\text{Width (w)} = \frac{r_l}{Bp^3}\left[\begin{matrix} 0.0021 - 0.047p + 0.34p^2 - 1.9p^3 - 0.33p^4 + \\ B(0.00066 - 0.007p - 0.00059p^2 + 2.8p^3 - 0.12p^4) + \\ B^2(-0.0007 + 0.015p - 0.12p^2 + 0.59p^3 - 0.023p^4) \\ + B^3(0.00001 - 0.00022p + 0.002p^2 - 0.0085p^3 + 0.0014p^4) \end{matrix}\right] \tag{28}$$

In another analysis, Fabbro *et al.* [144] utilized scaling laws to predict the melt pool aspect ratio (depth-to-width ratio). The following simplifying assumptions were made in constructing this model: (i) the melt pool is cylindrical in shape with diameter and length equal to the laser spot size diameter and melt pool depth, respectively, (ii) the temperature of the keyhole wall is constant and equal to the evaporation temperature of the material, and (iii) the melt pool is moving across a substrate with a constant temperature and at a constant speed. The melt pool aspect ratio is defined as:

$$\mathrm{R} = \frac{\mathrm{d}}{\mathrm{w}} = \frac{\mathrm{R_0}}{1 + (\mathrm{V}/\mathrm{V_0})} \tag{29}$$

where,

$$\mathrm{R_0} = \frac{\alpha \mathrm{P}}{\mathrm{n d_l K}(\mathrm{T_b} - \mathrm{T_o})} \tag{30}$$

$$\mathrm{V_0} = \frac{2\mathrm{nK}}{\mathrm{m d_l} \rho \mathrm{C_p}} \tag{31}$$

Here, R is the melt pool aspect ratio (depth-to-width), d is melt pool depth (m), w is melt pool width (m), V is laser scanning speed (m/s), α is laser absorptivity, P is laser power (W), d_l is laser spot diameter (m), K is thermal conductivity (W/mK), T_b is evaporation temperature (K), T_o is substrate temperature (K), ρ is density (kg/m^3), C_p is specific heat (J/kgK), m and n are linear coefficients that depend on the Pe number (refer to eq. (19)) and can be approximated analytically (to determine the values of m and n, readers are referred to [144]).

The melt pool aspect ratio can be used to determine the transition from conduction to keyhole mode of heat transfer in the LPBF process. It can be assumed that melt pool shifts from

conduction to keyhole for $R \geq 1$. This transition plays a vital role in LPBF processing of highly reflective materials such as copper. Jadhav *et al.* [145] have used the melt pool aspect ratio to determine the laser power and scan speed values where the keyhole mode of heat transfer can be achieved in LPBF processing of pure copper.

4.4 Criteria for porosity threshold

Several types of defects can be observed in the as-fabricated AM components such as porosities, contamination, cracking, delamination, distortion, surface roughness, microstructure inhomogeneity, and crystallographic anisotropy. This section specifically focuses on porosity and different analytical models to determine the porosity thresholds for lack of fusion, balling, keyholing, and partially melted powder particles. These analytical models are based upon the melt pool geometry and are either derived from the mathematical considerations or the experimental observations. Determination of these threshold values are essential to identify the processing window for any alloy.

4.4.1 Lack-of-fusion offset

Lack of fusion is one of the most studied porosity defects. These defects are detrimental to the properties because of their high aspect ratio and sharp edges. Their volume fraction increases with a decrease in energy supply [49,146]. But even in the case of a fully developed melt pool, a substantial fraction of lack-of-fusion defect can exist due to insufficient melt pool overlapping and high hatch spacing. In the study by Tang *et al.* [147] considering a dual semi-elliptical melt pool, a geometric model was proposed for the lack of fusion criterion as shown below:

$$\left(\frac{H}{w}\right)^2 + \left(\frac{L}{d}\right)^2 \leq 1 \tag{32}$$

where H is the hatch spacing (mm), L is the layer thickness (mm), w is the melt pool width (mm), and d is the melt pool depth (mm). According to this model, the ratio of the melt pool width to hatch spacing and melt pool depth to layer height should be high enough to provide sufficient overlapping. In another recent study [49], an expression for lack-of-fusion (LOF) index was applied to estimate the porosity defect fraction. It can be calculated in terms of laser parameters, melt pool geometry, and materials properties as:

$$\text{LOF index} = \rho\left(C_p \Delta T + \Delta H\right) \times \frac{\pi r_l^2 V}{\alpha P} \times Fo \times \frac{L}{d} \times \left(\frac{H}{w}\right)^2 \tag{33}$$

where P is laser power (W), V is scanning speed (m/s), H is hatch spacing (m), L is layer thickness (m), ΔT is the difference between peak temperature and melting temperature (K), ΔH is the latent heat of the material (J/kg), ρ is density (kg/m^3), C_p is specific heat (J/kgK), α is laser absorptivity, d is the melt pool depth (m), w is the melt pool width (m), and Fo is the Fourier number (dimensionless). As a rule of thumb, the penetration depth of the melt pool should be 50% higher than the layer thickness (i.e., $d/L > 1.5$) to avoid lack-of-fusion defects and improve interlayer bonding [86]. Also, the fraction of the lack-of-fusion defects increases linearly with the LOF index and can be calculated using:

$$\text{Volume of the LOF defects} = 15.3 \times \text{LOF index} \tag{34}$$

4.4.2 Balling threshold

Balling defects are a result of dynamic instability where the humping or irregular beads form along the melt pool tracks. These defects are influenced by the fluid dynamics, surface tension, and morphology of the melt pool [13]. Balling also occurs in the processes involving fluid flows such as welding [148,149]. When the Plateau-Rayleigh instability criterion is satisfied, that is the ratio of the melt pool length and width exceeds the critical value of pi, the molten metal tries to lower its surface energy by forming spherical droplets instead of spreading over the base plate [22,56]. In the work by Yadroitsev *et al.* [55] a modified version of the balling criterion was proposed for single track formation in the LPBF process. This model considered the added stability provided by the horizontal segmental melt pool tracks and can be represented by:

$$\frac{\text{Length (l)}}{\text{Width (w)}} < \sqrt{\frac{3}{2}}\pi \text{ or } 3.8 \tag{35}$$

Similarly, different critical values of the dynamic instabilities have been reported ranging from 2.3 to 6.24 depending upon the application. At high laser power and scanning speed, the melt pool has a lower width and an elongated tail end, and such processing conditions promote the balling defect [22,149].

4.4.3 Keyholing threshold

Keyhole porosities are spherical types of defects which occur due to melt pool instability at excessive heat supply. These pores often form in pairs and can be observed much below the powder surface [22,58]. An increase in laser power results in a gradual increase of the melt pool depth, and beyond a transition point, the depth starts to increase rapidly. This transition point is

when heat transfer changes from conduction to keyhole mode. [53,150]. At larger melt pool depths, the chances of gas entrapment from the vapor depression zone increases. Thus, the frequency of keyhole porosities also increases with energy density. Studies performed on *in situ* synchrotron x-ray techniques show that a higher melt pool front angle leads to keyhole porosities [58]. In the study by King *et al.* [53] an experimental correlation between the normalized enthalpy and keyhole threshold was reported. The keyhole threshold can be approximated by taking the ratios of the melting temperature (T_m) and boiling temperature (T_b) as shown below:

$$\frac{\Delta H}{H_s} = \frac{\alpha P}{\pi \rho C_p T_m \sqrt{D_t V r_l^3}} < \frac{\pi T_b}{T_m} \tag{36}$$

where P is laser power (W), V is scanning speed (m/s), r_l is laser spot radius (m), T_m is melting temperature (K), T_b is boiling temperature (K), ρ is density (kg/m^3), C_p is specific heat (J/kgK), D_t is thermal diffusivity (m^2/s), and α is laser absorptivity.

Data from different laser beam diameters suggest that the keyhole threshold for various alloys ranges between a normalized enthalpy value of 6 to 30. There are also some studies that predict the keyhole threshold based on the melt pool geometry [91]. Experimental data suggest that keyhole porosities can be avoided by increasing the width to the depth ratio as given below:

$$\frac{\text{Width (w)}}{\text{Depth (d)}} > 1.5 \tag{37}$$

With an increase in energy supply, the melt pool geometry changes from a shallow semi-spherical shape to a deep cylindrical shape. Therefore, eq. (37) suggests that keyholing occurs at higher energy densities.

4.4.4 Under-melted or partially melted threshold

Another potential processing defect can be the presence of under-melted or partially melted particles in the part. Under the scenarios of a low energy supply or a material with a low laser absorption coefficient, the fraction of under-melted particles can be high [54]. The issue of partially melted particles become more prevalent when two or more elemental powders having very different melting temperatures are mixed to get a desired alloy composition. The surface temperature can be estimated in terms of normalized enthalpy as given below:

$$T_{surface} = \frac{T_m \Delta H}{H_s} = \frac{\alpha P}{\pi \rho C_p \sqrt{D_t V r_l^3}} \tag{38}$$

where P is laser power (W), V is scanning speed (m/s), r_l is laser spot radius (m), T_m is melting temperature (K), ρ is density (kg/m^3), C_p is specific heat (J/kgK), D_t is thermal diffusivity (m^2/s), and α is laser absorptivity.

The under-melted and partially melted particles will get infused in a component when the surface temperature is lower than the melting temperature of the alloy i.e.:

$$T_{surface} = \frac{\alpha P}{\pi \rho C_p \sqrt{D_t V r_l^3}} < T_m \tag{39}$$

4.5 Additional analytical models

There are other analytical models and dimensionless numbers that do not necessarily contribute to construction of the processing maps but are relevant to the LPBF process. In this section, models to estimate vapor pressure, compositional change, thermal strain, depression depth, solidification cracking, and dendritic arm spacing are discussed briefly.

4.5.1 Vapor pressure and composition change

In the case of excessive heat supply, the peak temperature can easily exceed the material's boiling temperature leading to high vapor pressure and material volatilization. The saturated vapor pressure (P_s) can be calculated using the expression [53]:

$$\mathrm{P_s} = \mathrm{P^*}\exp\left[\lambda\left(\frac{1}{\mathrm{T_b}} - \frac{1}{\mathrm{T_s}}\right)\right] \tag{40}$$

where P^* is the atmospheric or the chamber pressure (Pa), λ is the evaporation energy per atom (eV), T_b is the boiling temperature (K), and T_s is the surface temperature (K) (refer to eq. (39)). Similarly, the recoil pressure (P_r) can be estimated to be around 0.56 times the saturated vapor pressure (P_s) [53]. In some alloys, especially when the boiling temperature of two alloying elements is significantly different, high vapor pressure can lead to variation in the compositional concentration. The vaporization flux (J_i) can be estimated using the Langmuir equations [86]:

$$\mathrm{J_i} = \frac{\mathrm{P_i}}{\sqrt{2\pi \mathrm{M_i R T_s}}} \tag{41}$$

where P_i is vapor pressure for alloying element i (Pa), M_i is the molecular weight of element i (kg/mol), R is the molar gas constant (J/molK), and T_s is the surface temperature (K) (refer to eq. (39). Finally, the amount of material vaporized (Δm_i) can be calculated using the expression [86]:

$$\Delta \mathrm{m_i} = \frac{\mathrm{lA_s J_i}}{\mathrm{V}} \tag{42}$$

where V is the scanning speed (m/s), A_s is the melt pool cross-sectional area (m^2), l is the track length (m), and J_i is the vaporization flux (mole/m^2s). Calculating the actual value of the melt pool area can be complicated. Nevertheless, eq. (26, (27, and (28 can be applied to get rough estimates of the melt pool geometry. The above equations can assist in defining the optimal processing parameters by avoiding material volatilization and fabricating parts with desired chemical composition.

4.5.2 Thermal strain

Residual stress in AM components originates from the spatial variation in thermal gradient and nonuniform thermal expansion and contraction [33,151]. For example, during solidification of the liquid metal, the new layer solidifies quickly and contracts at a faster rate than the layers beneath it. The geometrical constraints impose tensile stresses in the top layer and compressive stresses in the subsequent bottom layers [33]. These macroscopic stresses (long gradients of plastic deformation) can cause cracking, warpage, and distortion of AM components. The extent of the part's distortion can be estimated in terms of thermal strain (ϵ_t) and can be expressed in terms of materials property and processing parameters as [86]:

$$\epsilon_t = \frac{0.9\beta}{\mathrm{EI\ F_o}} \times \frac{\Delta \mathrm{T}\,\tau}{\sqrt{\rho}} \times \mathrm{LED}^{3/2} \tag{43}$$

where LED is linear energy density (J/m) (refer to eq. (13), ρ is density (Kg/m^3), ΔT is the temperature difference between the peak temperature and the solidus temperature (K), τ is the characteristic time (s), β is the coefficient of linear expansion, E is elastic modulus (MPa), I is the moment of inertia of the base plate (Kgm^2), and Fo is the dimensionless Fourier number. It is evident from the above equation that the thermal strain increases with an increase in LED and a control over the laser parameters, thermal gradient, and cooling rates can reduce the residual stress within AM components. Another factor which can influence residual stress is part geometry, more specifically changes in moment of inertia [13,85,152]. For example, warpage of a rectangular bar occurs along its long axis and the propensity of warpage increases with rectangular bar's aspect ratio.

In polycrystalline materials, another subcategory of residual stress (i.e., microscopic residual stress) prevails due to microstructural heterogeneity [153]. Local lattice mismatch, impurities, and high dislocation densities lead to elastic stress fields and differences in slip behavior. Studies have highlighted that dislocation density increases with an increase in energy density [60,61]. However, individual effect of macroscopic and microscopic residual stress cannot be estimated using eq. (43. Process parameters including hatch spacing and layer thickness relate to the number of heating and cooling cycles. Each cycle causes annealing effects in the surrounding regions resulting in annihilation of dislocations. It is important to note that the above analytical expression does not account for annealing effects and stress relaxation. To completely estimate residual stresses at different processing conditions more rigorous experimental and computational techniques should be applied [33,151,154,155].

4.5.3 Depression depth

A vapor cavity (i.e., vapor depression depth) forms due to the evaporation from the melt pool surface and a high recoil pressure exerting inward forces on the melt pool. A very large depression depth increases the probability of keyhole porosity formation. Several *in situ* synchrotron x-ray studies have been performed to study the depression depth and laser-metal interaction. In the study by Gan *et al.* [156] low dimensional scaling laws have been presented to estimate the depression depth and porosity fraction. The depression depth was defined in terms of a dimensionless keyhole number (*Ke*) which can be expressed as:

$$\mathrm{Ke} = \frac{\alpha(\mathrm{P}-\mathrm{P_o})}{\mathrm{V}{\mathrm{d_l}}^2}\left(\frac{1}{\rho \mathrm{C_p}(\mathrm{T_b}-\mathrm{T_o})}\right)\left(\frac{\mathrm{T_m}-\mathrm{T_o}}{\mathrm{T_b}-\mathrm{T_o}}\right) \tag{44}$$

where P is laser power (W), V is scanning speed (m/s), d_l is laser spot diameter (m), P_o is the minimum laser power able to generate a keyhole (W), α is laser absorption coefficient, ρ is density (Kg/m^3), C_p is specific heat (J/kgK), T_m is melting temperature (K), T_b is boiling temperature (K), and T_o is the build plate temperature (K). All the experimental data obtained from the *in situ* studies for different alloys correlated well with the depression depth (e^*) and Keyhole number. This correlation is expressed as:

$$\mathrm{e^*} = 5.12 - 5.07\,\exp(-\mathrm{Ke}) \tag{45}$$

4.5.4 Solidification cracking

The ability of a material to resist solidification cracking (or hot cracking) depends upon its thermodynamic properties and the solidification conditions. One of the rough parameters that can be used to quickly estimate the material's susceptibility to solidification cracking is the freezing temperature range i.e., the difference between the liquidus and the solidus temperature. A material with a high freezing temperature range takes longer to solidify with subsequent formation of thin liquid films between the grain boundaries making them prone to solidification cracking. Other metallurgical factors such as the presence of low-melting eutectics, solidification morphology, and surface tension of the grain boundary liquid also influence the material's tolerance to solidification cracking. The crude estimates from the freezing temperature range criterion are not effective to design alloy compositions, especially for welding and AM processes because of the high cooling rates and metastable solidification. In studies by Kou [157,158], an index was presented to calculate the alloy's susceptibility to solidification cracking. According to this criterion, the cracking depends upon the maximum steepness of the curve between temperature (T) and square root of the fraction solid $(f_s)^{1/2}$ and it is expressed as:

$$\text{Kou index} = \frac{\mathrm{dT}}{\mathrm{d}(\mathrm{f_s})^{1/2}} \text{ near } (\mathrm{f_s})^{1/2} = 1 \tag{46}$$

Where T is temperature (K) and f_s is solid fraction of semi-solid region. The lower the steepness, the higher the material's resistance to solidification cracking would be. This parameter can be calculated using any commercial thermodynamic software package provided that the thermodynamic database is available. In the study by Tang et al [159], a modified version of Kou

index was presented by combining the effects from the solidification kinetics, solidification shrinkage, and high temperature materials property. The modified index can be expressed as:

$$\text{Modified index } 1 = \frac{\mathrm{dT}}{\mathrm{d}(\mathrm{f_s})^{1/2}} \frac{1}{\sqrt{1-\mathrm{s_f}}} \tag{47}$$

$$\text{Modified index } 2 = \frac{\mathrm{dT}}{\mathrm{d}(\mathrm{f_s})^{1/2}} \frac{1}{\bar{\mathrm{E}}} \tag{48}$$

Where T is temperature (K), f_s is solid fraction of semi-solid region, s_f is shrinkage factor, and $\bar{E}$ is materials toughness (MPa) near the solidus temperature. Shrinkage factor represents the ratio of the materials density at liquidous to materials density at solidus temperature. The material with high solidification shrinkage will have more susceptibility towards solidification cracking. Other index is a function of material toughness i.e., yield strength multiplied by fracture strain. A material possessing high material toughness at elevated temperatures will show better resistance to solidification cracking. In the comparative analysis between the above index, modified index 2 (eq. (48) provided the better correlations with the experimental and synchrotron results.

4.5.5 Cooling rate and dendritic arm spacing

The average cooling rate can be estimated based on heat distribution calculations and Rosenthal equations. In the study by Tang *et al.* [160], the average cooling rate (ε) was expressed as:

$$\varepsilon = 2\pi \mathrm{K}(\mathrm{T_{solidus}} - \mathrm{T_o})(\mathrm{T_{liquidus}} - \mathrm{T_o})\frac{\mathrm{V}}{\mathrm{P}} \tag{49}$$

where P is laser power (W), V is scanning speed (m/s), K is thermal conductivity (W/mK), T_o is build plate temperature (K), and $T_{solidus}$ and $T_{liquidus}$ are the solidus and liquidus temperature, respectively (K). It is evident from the above equation that the cooling rate depends upon laser power and scanning speed. The average cooling rate increases with a decrease in linear energy density (refer to eq. (13). Experimental observations also support the inverse dependence of energy density and cooling rate [13,161]. Also, the above equation implies that the material with higher thermal conductivity will exhibit a greater cooling rate dependence with the laser parameters.

The dendritic arm spacing is directly related to the average cooling rate [162–164]. Generally, the secondary dendritic arm spacing (λ_{SDAS}) can be calculated using the cooling rate value as:

$$\lambda_{SDAS} = a\varepsilon^{-b} \tag{50}$$

Where ε is cooling rate (K/s), and a and b are material constants. For example, the values of a and b for 316L stainless steel are 25 and -0.28 respectively [165,166]. An estimate of the primary dendritic arm spacing (λ_{PDAS}) can also be made using the cooling rate, but these values show marginal deviation as the PDAS continues to coarsen during the solidification process. In as-solidified components, the yield strength and hardness are correlated with the dendritic arm spacing values using a Hall-Petch equation as:

$$\sigma_y = \sigma_o + K(\lambda_{SDAS})^{-0.5} \tag{51}$$

Where σ_y is yield stress (MPa), σ_o is internal frictional stress (lattice resistance to dislocation motion) (MPa), K is strengthening coefficient, and λ_{SDAS} is secondary dendritic arm

spacing (μm). For most alloys, the hardness can be approximated by taking one-third of the yield strength [167]. Thus, the as-solidified microstructures and properties are related to the laser-metal interaction (eq. (49, (50, and (51). Therefore, a better control over the process variables can help to refine the microstructures and tailor the material's properties.

4.6 Predictive processing maps

Section 4.4 introduced four types of porosity defects and their respective analytical models and threshold criteria. These thresholds can be combined with analytical expressions reviewed in this work to obtain comprehensive processing maps for different materials. The purpose of these maps is to provide an overview of the processing space that can be constructed analytically and without the need to conduct experiments to obtain data. The selected equations to construct these maps use *a priori* parameters as opposed to parameters that require *in situ* measurements. Further refinement maybe possible with the *in situ* experimental data gathered from other expressions introduced in this work. Microstructural features such as hot short cracking, texture, and grain size will most likely be a subset within these processing bounds. Tailoring of these features will only be possible once the primary processing conditions and their associated defects are identified.

4.6.1 PV map construction

With consideration of the analytical expressions presented in this review, the predictive PV processing maps were constructed for eight different elemental metals and alloys i.e., 316L stainless steel, Cantor alloy, Inconel 718, Haynes 282, Copper, Tantalum, Molybdenum, and Tungsten. The thermophysical properties required to generate these PV maps were previously shown in Table 1. This group of materials are commercially available for the LPBF process, and

they represent a broad range of thermophysical properties. For example, tungsten has a high melting temperature and copper has a high thermal conductivity. In addition, some of these materials are single-phase alloys while others are precipitation hardened alloys. Thermal diffusivity for these materials ranges from 2.88 to 115 mm^2/s which differs by two orders in magnitude. Values reported in Table 1 are at room temperature and assumed to be temperature independent. In addition, changes in the physical properties due to differences in powder processing is neglected. For example, it might be possible that the feedstock powder particles may have a lower density (due to gas porosities or metastable phases) than their wrought counterparts. Finally, an approximation of the laser absorption coefficient was made by taking the average values of the reported ranges. These values are difficult to precisely measure and are dependent on the laser parameters and powder size distribution [25].

PV maps provide a visual snapshot of the LPBF processing regime. Processing maps consist of five distinct regions: keyhole (blue), balling (pink), partially melted powders (grey), lack of fusion (red), and optimal (green) as shown in Figure 25. These PV maps were plotted at constant hatch spacing, layer thickness, and laser spot size (infrared fiber laser with ~100 µm spot size) for each material in accordance with some of the available experimental data in the literature. A comparison between the two is presented in section 4.6.2. Additionally, constant VED lines are plotted to highlight the overall input energy required to process these materials at each region. The VED values vary from 25 to 600 J/mm^3.

Table 7. Selected analytical equations and corresponding thresholds used to construct PV maps.

Region	Equation(s)	Threshold
Lack of fusion	$Width\ (w) = \sqrt{\frac{8\alpha P}{\pi e \rho C_p V (T_m - T_o)}}$ $Depth\ (d) = \sqrt{\frac{2\alpha P}{\pi e \rho C_p V (T_m - T_o)}}$	$\left(\frac{H}{w}\right)^2 + \left(\frac{L}{d}\right)^2 \leq 1$
Balling	$Depth\ (w) = \frac{r_l}{\sqrt{p}}\left[\begin{matrix}0.008 - 0.0048B - 0.047p - 0.099Bp \\ + plnp(0.32 + 0.015B)\ + lnB(0.0056 - 0.89p + 0.29plnp)\end{matrix}\right]$ $Length\ (d) = \frac{r_l}{p^2}\left[\begin{matrix}0.0053 - 0.21pB + 1.3p^2 - (0.11 + 0.17B)\ p^2 lnp \\ + B(-0.0062 + 0.23p + 0.75p^2)\end{matrix}\right]$ $Width\ (l) = \frac{r_l}{Bp^3}\left[\begin{matrix}0.0021 - 0.047p + 0.34p^2 - 1.9p^3 - 0.33p^4 + \\ B(0.00066 - 0.007p - 0.00059p^2 + 2.8p^3 - 0.12p^4) + \\ B^2(-0.0007 + 0.015p - 0.12p^2 + 0.59p^3 - 0.023p^4) \\ + B^3(0.00001 - 0.00022p + 0.002p^2 - 0.0085p^3 + 0.0014p^4)\end{matrix}\right]$	$\frac{l}{w} < 3.8$
Keyhole	$\frac{\Delta H}{H_s} = \frac{\alpha P}{\pi H_s \sqrt{D_t V r_l^3}} = \frac{\alpha P}{\pi \rho C_p T_m \sqrt{D_t V r_l^3}}$	$\frac{\Delta H}{H_s} < \frac{\pi T_b}{T_m}$
Under-melted	$\frac{\Delta H}{H_s} = \frac{\alpha P}{\pi H_s \sqrt{D_t V r_l^3}} = \frac{\alpha P}{\pi \rho C_p T_m \sqrt{D_t V r_l^3}}$	$\frac{T_m \Delta H}{H_s} < T_m$
Optimal	$E_{dim} = \frac{C_p P}{K V^2 H}$	$61 \leq E_{dim} \leq 146$

The lack-of-fusion region was calculated using the Rosenthal-based melt pool equations (eq. (22 and (23) and the LOF offset criterion (eq. (32). Rosenthal equations were derived assuming semi-elliptical melt pool geometry (i.e., the melt pool depth is twice the melt pool width). These assumptions are valid only at lower energy density values and thus they are appropriate to calculate the LOF regions. The balling region was calculated using the melt pool estimates from the Egar-Tsai models (eq. (26, (27, and (28) combined with the balling criterion (eq. (35). Similarly, the calculations for the keyhole threshold (eq. (36) and under-melted regions (eq. (39) were based on the normalized enthalpy values (eq. (17). Finally, the optimal region was estimated from the

dimensionless energy density (eq. (20) where the dimensionless energy density values of 61 and 146 represent the lower and upper processing boundaries respectively. Within these ranges, a high relative density of 99.5% was observed for different metals and alloys [114]. The selected equations and their corresponding thresholds are summarized in Table 7.

In certain sections of PV maps, overlapping of processing regimes can occur. For example, lack-of-fusion and under-melted regions overlap at lower energy density regions. In principle, all the processing conditions that result in under-melted particles will also show a lack-of-fusion porosity. So, the under-melted region is expected to be within the lack-of-fusion region. However, due to different analytical models used for each defect, the under-melted region extends outside the lack-of-fusion region. The deviation in the prediction is due to: (i) inability to precisely predict the melt pool geometry at different processing conditions, and (ii) uncertainty in the threshold values for different defect criteria. Similarly, the overlapping of keyhole and balling regions occurs at high power and high velocity values. The overlap of different regions also suggests that individual criteria is not sufficient to completely bound the formation of porosity defects.

It is important to note that the mapped regions are a result of simplified analytical models. As a result, they should be interpreted as coarse predictions rather than absolutes. Any processing condition that does not lie within the lack-of-fusion (red), under-melted (black), balling (pink), and keyholing (blue) regions is less likely to show any porosity defects during fabrication. In other words, the probability of defect formation increases as the corresponding defect boundary is crossed. Similarly, the optimal (green) region represents the set of processing parameters that are least likely to cause porosity defects.

Processing maps for 316L stainless steel and Cantor alloy are shown in Figure 25a and b. These maps are plotted at a hatch spacing of 0.11 and 0.08 mm and a layer thickness of 0.02 and

0.05 mm. Both alloys are based on the Fe-Cr-Mn elemental constituent with 316L stainless steel having a Fe-rich composition and the Cantor alloy having an equiatomic composition. The middle of the optimal processing window for 316L and Cantor alloy is around 200W and 800 mm/s and 250W and 850 mm/s, respectively.

Processing maps for Inconel 718 and Haynes 282 alloys are shown in Figure 25c and d. These maps are plotted at a hatch spacing of 0.11 mm and a layer thickness of 0.04 mm. Both alloys are precipitation hardened Ni-base superalloys and have similar alloy compositions. The lack-of-fusion region estimated for Haynes 282 is much bigger as compared to Inconel 718. However, the middle of the processing window for both alloys is around 250 W and 950 mm/s. In comparison to the 316L stainless steel, the Ni-base superalloys require about 50% less input energy density, primarily due to the use of a thicker layer thickness in the calculations.

Processing maps for copper and refractory metals are shown in Figure 25e-h. Interestingly, the keyhole and balling region is not expected in any of these materials within the calculated processing ranges as shown in Figure 25e-h. All these metals require very high energy density to fabricate, and the processing window is skewed towards the high power of 360-400 W and low scanning speed of 200-250 mm/s. Refractory metals have high melting temperatures, therefore, higher input energy is needed to melt them. Although the melting temperature of copper is low, the metal has a high thermal diffusivity and low laser absorption coefficient in the infrared range. Most of the heat absorbed by copper powder gets transferred to surrounding regions. Thus, to reduce the porosity defects in LPBF processing of copper and refractory metals, higher energy densities are required [21,67,168,169].

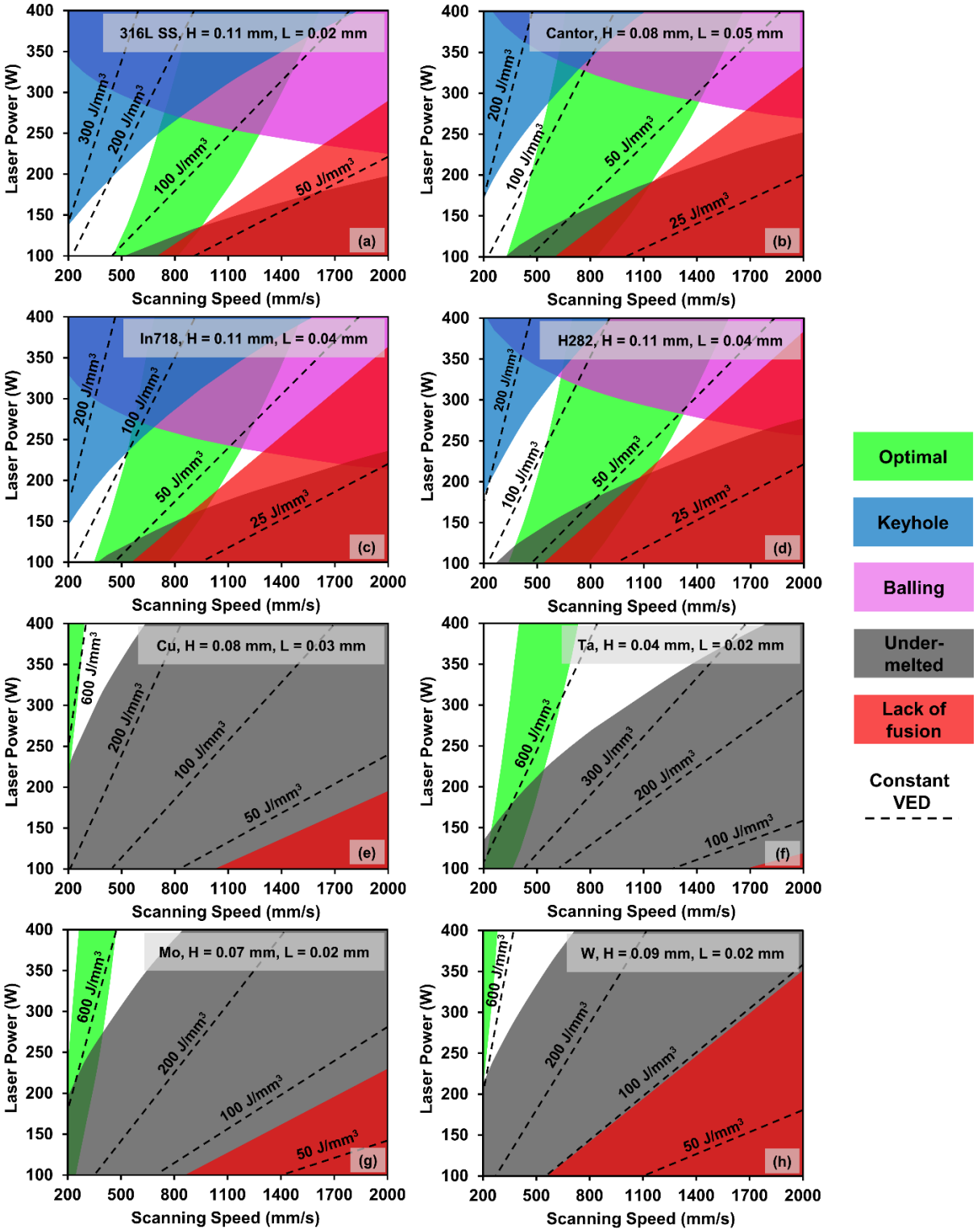

Figure 25. Predictive PV processing maps for (a) 316L stainless steel (b) Cantor alloy (c) Inconel 718 (d) Haynes 282 (e) Copper (f) Tantalum (g) Molybdenum, and (h) Tungsten generated using analytical models.

Table 8. A summary of reported experimental data in the literature pertaining to PV maps in Figure 25.

Material	Power (W)	Velocity (mm/s)	Hatch Spacing (mm)	Layer Thickness (mm)	VED (J/mm3)	Reported Region	Predicted by PV maps	Ref.
SS316	120	600	0.11	0.02	91	LOF	No	Agrawal et al. [124]
	200	800			114	Optimal	Yes	
	200	1300			70	LOF	No	
	280	600			212	Keyhole	Yes	
Cantor Alloy	200	750	0.08	0.05	63	Optimal	Yes	Dovgyy et al. [170]
	200	430			110	Keyhole	No	
Inconel 718	100	1000	0.11	0.04	23	Under-melted	Yes	Scime and Beuth [129]
	250	200			284	Keyhole	Yes	
	250	800			71	Optimal	Yes	
	300	1400			49	Balling	Yes	
Haynes 282	200	1500	0.11	0.04	30	LOF	Yes	Islam et al. [126]
	250	975			58	Optimal	Yes	
	350	500			159	Keyhole	Yes	
Cu	150	600	0.08	0.03	104	LOF	Yes	Yan et al. [54]
	250	400			260	LOF	No	
	350	1000			146	Under-melted	Yes	
Ta	370	550	0.04	0.02	841	Optimal	Yes	Livescu et al. [67]
	370	770			601	LOF	No	
Mo	250	400	0.07	0.02	446	Keyhole	No	Higashi and Ozaki [169]
	250	1000			179	LOF	Yes	
	350	400			625	Optimal	Yes	

W	200	400	0.09	0.02	278	LOF	Yes	Tan et al. [171]
	200	300			370	LOF	Yes	
	200	200			556	LOF	Yes	

4.6.2 Experimental data

To assess the predictive capability of the constructed PV maps, experimental data were gathered from the literature for each corresponding material in Figure 25. A summary of the selected experimental data is presented in Table 8. A one-to-one comparison of generated maps and available experimental data is only possible if the laser spot size, laser wavelength, and powder particle size, are similar in both scenarios. The PV maps are generated using a laser spot size of ~100 µm with a wavelength of ~1070 nm. Similar laser systems were used in the collected experimental data. Moreover, similar hatch spacing, layer thickness and *P*-*V* range was used in the reported experimental data. Overall, the experimental data agrees with the analytical PV processing maps.

There are a few instances where the experimental data does not agree with the analytical predictions. For those cases, the experimental data is in fact in close proximity to the predicted region in the PV map. For every material under consideration in this work, the optimal parameter set that is experimentally obtained, is accurately predicted by the PV processing maps. This agreement highlights the predictive capability of analytical PV maps in guiding users to find the desirable processing parameters of materials under development for LPBF in a cost effective and timely manner.

4.7 Summary and outlook

The present work provides a framework for designing processing parameters in the LPBF process based on a comprehensive review of available analytical models. The models used are mainly considered for melt pool geometry and the occurrence of porosity defects. These models are applied to wide-ranging metals and alloys processed by LPBF to quickly generate and predict the processing maps. The processing maps provide information about the various types of porosity defects at different power-velocity combinations. The predictive capability of the processing maps is compared with existing experimental data from across the literature. Predictions can be improved significantly by improving the melt pool geometry estimates. Although these maps are approximations and some of the calculations rely on hard to acquire parameters such as laser absorption coefficient, analytical based PV maps can be computed quickly to provide an estimation for the processing window. This approach can be easily coupled with HT experiments or *in situ* monitoring to improve the predictability and verify the LPBF processing bounds. The following summary captures the approach to generate predictive LPBF processing maps and fabricate dense LPBF components:

1) Materials properties and process parameters are the key factors influencing the laser-metal interaction and melt pool geometry.
2) Control over the melt pool geometry is essential to mitigate and minimize porosity defects. Melt pool geometry including width, depth, and length can be quickly estimated using the Rosenthal and Egar-Tsai based analytical models for various processing conditions.

3) Defect criteria for different porosity defects such as lack of fusion, balling, and keyholing, coupled with melt pool geometry can be used to estimate the processing bounds and generate predictive processing maps.
4) Dimensionless numbers and design parameters help in correlating the processing parameters and reducing the dimensionality of the input parameter processing space.
5) Existing analytical solutions for the LPBF process can be combined to construct processing maps with excellent predictive capability for optimal or defective regions.

Chapter 5: Microstructural design of LPBF components

In this chapter, the influence of processing parameters on microstructure and performance is presented. Within the optimal region, as identified in earlier chapters, multiple samples have been chosen for low throughput microstructural characterization. The microstructural analysis included quantification of average grain size, grain aspect ratio, texture, dendritic arm spacing, and melt pool morphology. The experimental data and results presented have been published in the following work:

- A.K. Agrawal, G. Meric de Bellefon, D. Thoma, High-throughput experimentation for microstructural design in additively manufactured 316L stainless steel, Mater. Sci. Eng. A. 793 (2020) 139841. doi:10.1016/j.msea.2020.139841.

In section 5.8, spall strength on selected additively manufactured 316L SS was evaluated. The experiments were conducted in collaboration with Los Alamos National Laboratory. My major role was to process design, supply samples, and quantify microstructural features for the samples. The results and data presented in this section are unpublished with a manuscript in preparation.

Similarly, section 5.9 is focused on the microstructural design of precipitation hardened Inconel 718 alloy specifically minimizing Laves phase fraction from the as-fabricated materials. My role included the design of experiments (DOE), sample fabrication, and microstructural investigation. Collaboration is underway for the TEM analysis of the samples. The results and data presented in this section are unpublished.

Out of all of the alloys (Table 1), a detailed analysis on 316L SS is done mainly due to two reasons: (i) the alloy's widespread commercial and industrial applications and (ii) relatively simpler in processing being a single-phase FCC alloy. In this chapter, an approach to control and design the microstructure of LPBF-fabricated 316L SS is presented.

5.1 Introduction

Additively manufactured materials display unique hierarchical microstructures consisting of cellular-dendritic structure, high dislocation density, columnar grains, low angle grain boundaries, and crystallographic texture [12,172–176]. Such microstructural evolution arises as a result of the rapid solidification conditions and high thermal gradient [13]. In addition, the moving laser beam and multiple thermal cycles in the LPBF process affects the prior solidified structures [13].

AM materials display an excellent combination of yield strength and ductility [12,60,177,178]. High strength is attributed to fine cellular structure and high dislocation density [179–182]. Cellular structures are effective in blocking the dislocation motion. Thus, finer structure sizes lead to more dislocation resistance and strengthening effects [183]. These structures are thermally stable, and a small amount of cell size increment was observed even at high temperatures [59,184]. However, the yield strength of the parts drops significantly after the heat treatment due to the annihilation of dislocations, suggesting dislocation density is also a dominant strengthening factor [62,71,75,185,186]. Interestingly, despite having high dislocation density, the TEM analyses of LPBF samples revealed dislocation forms a network around the interdendritic region and a negligible number of dislocations are present within the dendritic region [60].

In most cases, columnar elongated grains are observed in as-fabricated LPBF samples. In addition, epitaxial grain growth leads to grain sizes three to four times the deposition layer thickness [12,172]. A strong crystallographic texture along the building direction also results in an anisotropic mechanical response of AM materials [187–191]. A study by Bertoli *et al.* [63] showed that crystallographic texture is strongly related to the melt pool geometry and hatch spacing.

This work is aimed at quantifying the effects of processing parameters on microstructural features. Microstructural analysis at different length scales (average grain size, grain aspect ratio, texture, dendritic arm spacing, melt pool morphology) was performed. The dependence of microstructural evolution on the melt pool geometry was established. This study will help design as-solidified microstructures of additively manufactured materials.

5.2 Experimental procedure

Based on the results of the HT study, seven samples within the processing window of VED= 70-150 J/mm^3 (refer to section 2.3.3) were selected for low throughput analysis. These specimens had a relative density of >99% and were free from lack-of-fusion or keyholing type defects. The processing parameters of these seven specimens are shown in Table 9. The processing parameters of LT specimens were selected such that effect of laser power, scanning speed, and VED can be studied.

The seven specimens were sectioned along the build direction and cold mounted using an epoxy resin to study the planar and the cross-sectional surface. Planar surfaces were ground to the approximate depth of 1 mm from the bottom surface, and this depth was uniform for all the specimens. A conventional metallographic practice involving mechanical grinding and polishing was used to prepare these specimens for further analysis. Final polishing was performed using a 0.5-micron alumina and 0.05-micron colloidal silica solution. Prior to microscopy, specimens were cleaned and rinsed using isopropanol.

Electron backscatter diffraction (EBSD) mapping of planar surfaces was carried out in a FEI Helios G4 High-Resolution FEG-SEM. An accelerating voltage of 30 kV and a current of 51 nA was used to collect EBSD data form the 1x1 mm region with a step size of 1 µm. EBSD data

was analyzed using the MATLAB based MTex toolbox, in particular to calculate grain sizes and textures. To calculate a grain size, grain boundaries having a misorientation greater than 5 degrees were mapped. Smaller grains (i.e., total grain area <20 μm^2) were removed from the analysis. The grain size was calculated by measuring the largest distance (in pixels) within each grain. Non-weighted number average provided the average grain size value. Refer to "Appendix 2" for detailed grain size analysis. For texture analysis, the 'odf1' function was used to calculate the orientations of each pixel. A reconstruction of these datasets using the 'plotIPDF' function was done to generate IPF maps with the build direction as a reference direction.

Similar metallographic preparation and electrochemical etching were performed for the cross-sectional surfaces. Electrochemical etching of the 316L SS was done using a 0.1 M oxalic acid solution operated at 5.5 mV to reveal grain boundaries and dendrites. Chemical etching using ferric chloride solution was used (i.e., 5 g $FeCl_3$, 20 ml HCl, 80 ml ethanol) to reveal the melt pool boundaries. Optical microscopy (OM) and Scanning Electron Microscopy (SEM) of cross-sectional surfaces were carried out in a Keyence VHX-5000 and a ZEISS LEO 1530 FEG-SEM respectively. An accelerating voltage of 5 kV was used to collect the SEM images. SEM and optical image analysis were performed using ImageJ software, in particular for dendrite analysis.

5.3 Effect of processing parameters on as-solidified microstructure

EBSD maps and inversed pole figure (IPF) plots of the specimen's planar surfaces are shown in Figure 26. Grains had an irregular and elongated shape. In each specimen, the variation in grain size was from 10 to 50 µm. As the energy density increases from 69.9 to 151.5 J/mm^3, an increase in average grain size from 23.0 to 35.1 µm was observed. In addition, the texture of the

specimens also varied with VED. At a lower VED of 69.9 J/mm^3, a random texture was observed. With increasing VEDs, specimens showed a texture towards (110) and (100) plane with respect to the build direction. These specimens showed an IPF intensity of ≈2, which means twice the number of grains were oriented towards (110) plane than that of completely random texture. A similar variation in average grain size and texture with VED was observed for the rest of the specimens (see Table 9).

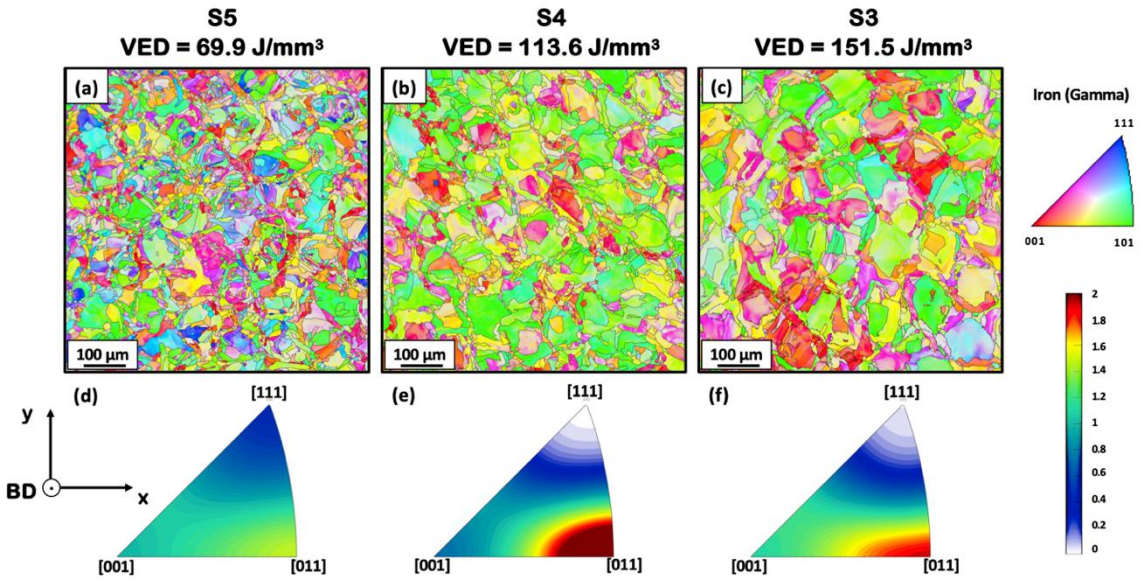

Figure 26. EBSD maps and IPF of the 316L SS LPBF-fabricated specimens (a,d) S5, VED = 69.9 J/mm^3, (b,e) S4, VED = 113.6 J/mm^3, and (c,f) S3, VED = 151.5 J/mm^3. The reference direction for the IPF maps is Build direction (BD).

A similar microstructure was obtained at constant VED values. EBSD mapping of specimens S2 and S5 processed at similar VED ≈ 70 J/mm^3 are shown in Figure 27. In both specimens, the average grain size was measured to be 23.0 and 22.8 µm, and a random texture was observed. The difference in the average grain size was less than 5%. EBSD mapping of other

specimens also showed similar average grain size values at constant VED of 90 J/mm^3 and 150 J/mm^3 (Table 9).

Table 9. Processing parameters and LT characterization of the selected specimens

S.No.	Laser power(W)	Scanning speed (mm/s)	VED (J/mm^3)	Average grain size (μm)	Grain aspect ratios	Primary dendrite arm spacing (μm)
S1	120	600	90.9	26.1 ± 19.8	3.6 ± 1.2	0.42 ± 0.05
S2	120	800	68.2	22.8 ± 15.1	2.7 ± 1.4	0.40 ± 0.03
S3	200	600	151.5	35.1 ± 31.7	5.6 ± 2.5	0.56 ± 0.04
S4	200	800	113.6	34.3 ± 27.6	3.4 ± 1.9	0.46 ± 0.04
S5	200	1300	69.9	23.0 ± 16.3	3.0 ± 0.6	0.39 ± 0.03
S6	260	800	147.7	34.9 ± 33.6	5.0 ± 1.5	0.57 ± 0.10
S7	260	1300	90.9	30.9 ± 30.9	3.10 ± 1.4	0.47 ± 0.07

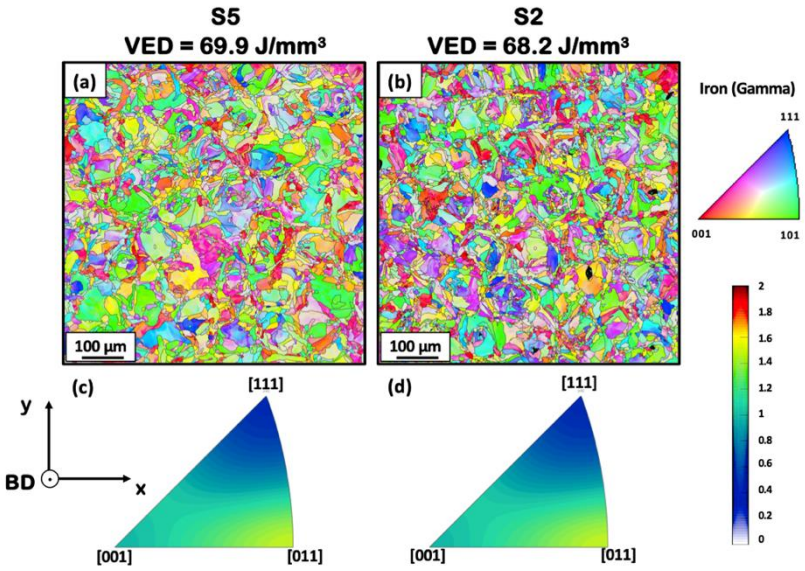

Figure 27. EBSD maps and IPF of the 316L SS LPBF-fabricated specimens (a,c) S5, VED = 69.9 J/mm^3 and (b,d) S2, VED = 68.2 J/mm^3.

The cross-sectional SEM images of the S3, S4, and S5 specimens are shown in Figure 28a-c. Specimens were aligned such that the build direction points upwards, and the SEM images were taken at a similar height in the build direction to maintain consistency. Grain boundaries (white boundaries) in each of the images were manually drawn. For each grain, longitudinal length and transverse length were measured. By analyzing multiple images from each processing condition, statistically, the average grain aspect ratio was calculated. At lower energy densities of 69.9 J/mm^3, more spherical grains were observed. The average grain aspect ratio was around 3.0 ± 0.6. As the energy density increased to 151.5 J/mm^3, the average grain aspect ratio also increased from 3.0 $\pm$ 0.6 to 5.6 ± 2.5. Interestingly, an increase in the average grain aspect ratio was accompanied by a simultaneous increase in both longitudinal length and transverse length.

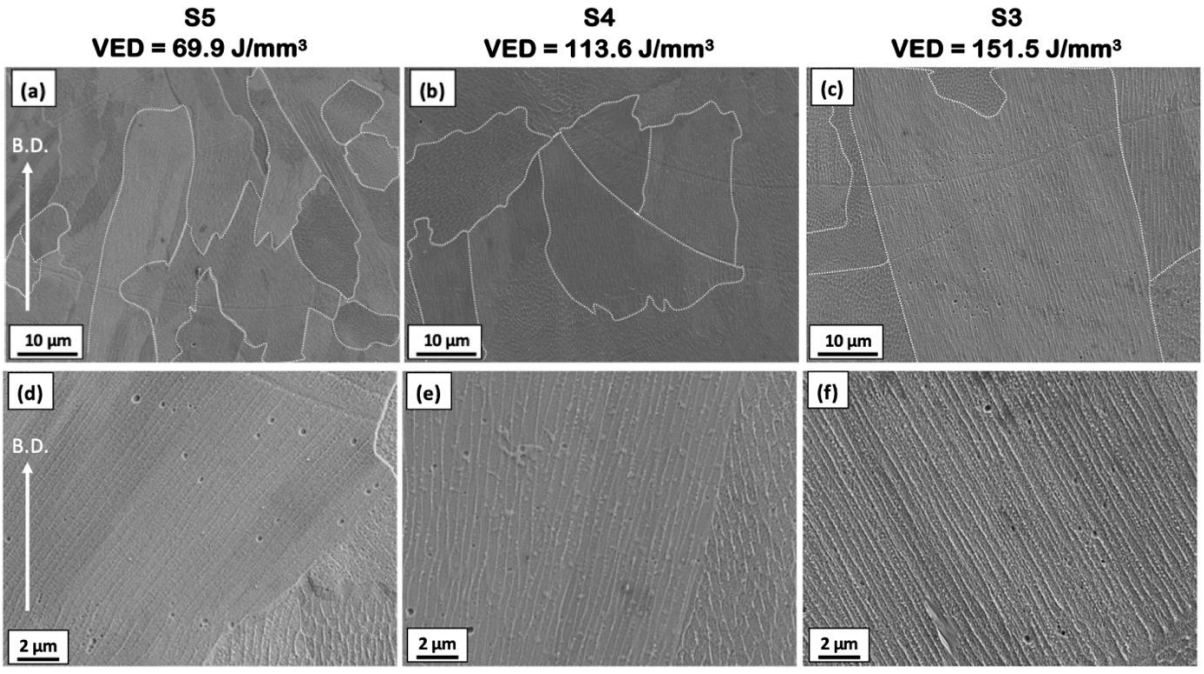

Figure 28. Cross sectional SEM images of the 316L SS LPBF-fabricated specimens (a,d) S5, VED = 69.9 J/mm^3, (b,e) S4, VED = 113.6 J/mm^3, and (c,f) S3, VED = 151.5 J/mm^3 showing grain morphology (white dash lines) and primary dendrite arm spacing.

The dendritic structure of the S3, S4, and S5 specimens is shown in Figure 28d-f. In LPBF components, the solidification structures vary along the z-direction owing to the variation in cooling rates. For comparison, specimens were aligned in the building direction and the various SEM images were captured at a similar z-height in each specimen. Also, images of dendrites were captured along the center of the melt pool to minimize the influences of heat affected zones. The distance between the dendrites was measured only for the cases in which the dendrites were long (constant distance) ensuring the dendrites were perpendicular to the surface. Multiple measurements (i.e., 15-20 per specimen) for primary dendrite arm spacing were performed. At lower energy densities of 69.9 J/mm^3, the average primary dendrite arm spacing measurement was 0.39 ± 0.03 µm. As the energy density increased to 151.5 J/mm^3, the average primary dendrite arm spacing increased by around 43%. A linear regression analysis (R-square = 0.95, p-value = 1.9e-4) was performed to estimate the primary dendrite arm spacing (µm):

$$\text{PDAS} = 0.26 - 0.0019 \times \text{VED} \tag{52}$$

5.4 Effect of processing parameters on melt pool geometry

Melt pool boundaries of the S3, S4, and S5 specimens are shown in Figure 29. Successive overlapping of the melt pool is apparent in all of the specimens. The overlapping pools are essential for good bonding between the layers and fabricating fully dense components. Some of the layers have a long streak of the melt pool due to the orientation effects (hatch rotation of 67 degrees). A detailed measurement of the melt pool dimensions was difficult due to the orientation effects and the overlapping melt pools.

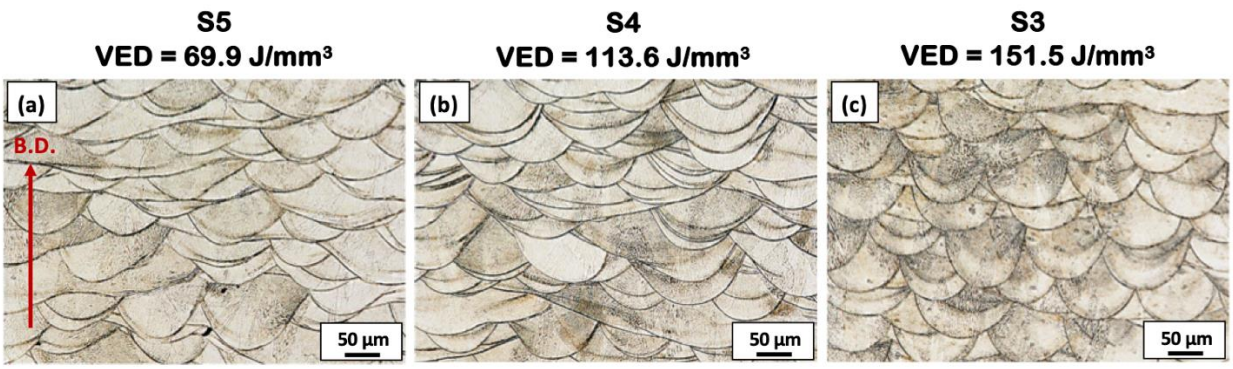

Figure 29. Cross sectional optical micrographs of the 316L SS LPBF-fabricated specimens (a) S5, VED = 69.9 J/mm^3, (b) S4, VED = 113.6 J/mm^3, and (c) S3, VED = 151.5 J/mm^3 showing melt pool boundaries.

Dependence of the melt pool dimensions with energy density is shown in Figure 30. At a lower VED of 69.3 J/mm^3, a shallower melt pool was observed with a more conical morphology. The melt pool dimensions were calculated by taking an average measurements of melt pool size across the bulk cross section of the sample. The average width and depth of the melt pool was around 110.22 $\pm$ 8.04 µm and 63.45 $\pm$ 11.19 µm, respectively. The width of the melt pool was similar to the laser beam diameter ($\approx$ 100 µm). As the energy density increased, the melt pool became deeper and had a semi-spherical morphology. At a VED of 151.5 J/mm^3, the average width and the depth of the melt pool was around 133.70 $\pm$ 10.84 µm and 90.95 $\pm$ 10. 32 µm, respectively. The variation in melt pool depth with energy density has also been reported in prior studies [87] .

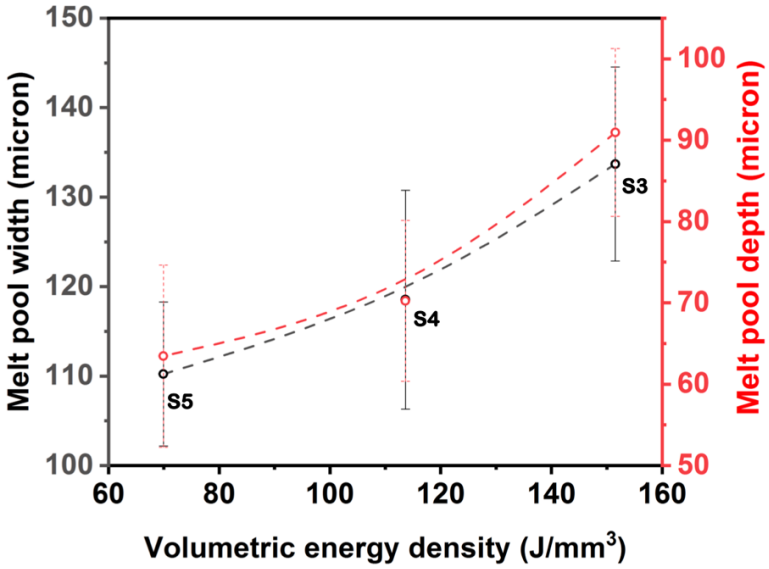

Figure 30. Melt pool width (black) and melt pool depth (red) of the S3, S4, and S5 specimens. A fitted line is used for a visual guide of the two data sets.

5.5 Microstructure-based process maps

PV maps are a convenient way to compare microstructural features as a function of process parameters. The average grain size (Figure 31a), the grain aspect ratio (Figure 31b), the average grain boundary misorientation (Figure 31c), and the primary dendrite arm spacing (Figure 31d) are summarized as "heat maps" within the acceptable VED boundaries [124]. The average GB misorientation showed similar trends with energy densities as grain size and grain aspect ratio. At lower energy densities, a high fraction of high angle boundary was measured, potentially due to the presence of more spherical grains and higher cooling rates. As the energy density increased, the fraction of high angle boundaries decreased. These specimens also showed a higher fraction of columnar grains with grain aspect ratio up to 5.60. Collectively, the microstructural refines at lower energy densities, with a corresponding increase in grain boundary misorientation.

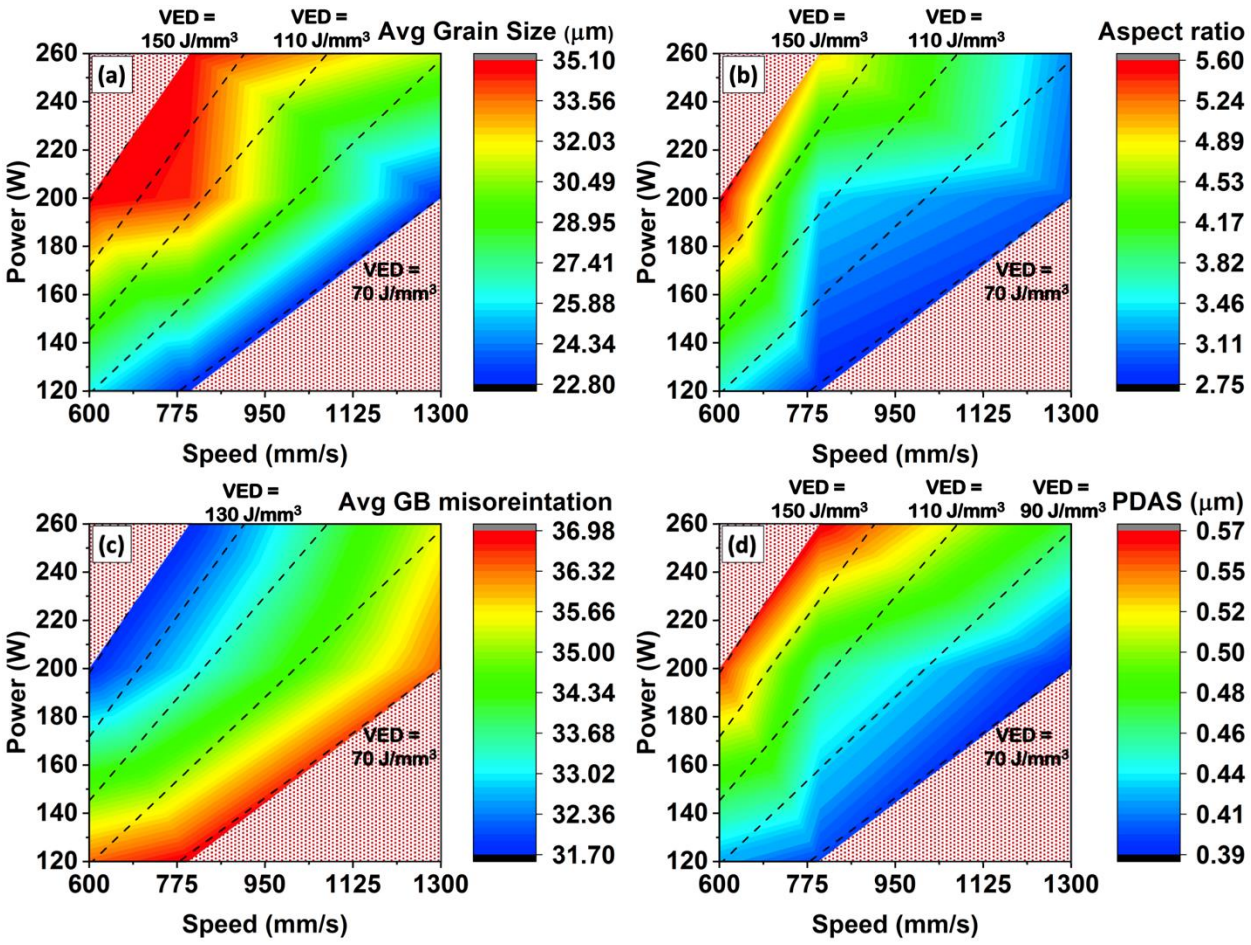

Figure 31. Microstructural mapping of (a) grain size (b) grain aspect ratio and (c) average grain boundary misorientation (d) primary dendrite arm spacing of 316L SS fabricated using LPBF techniques. Heat maps are generated using data points of the S1-S7 specimens.

Texture analysis and IPF mapping of the LT specimens are summarized and shown in Figure 32. The specimens with energy densities around 70 J/mm^3 showed a more random texture. As the energy density increased, a texture towards (110) formed. In different alloy systems, similar texture anisotropy results in as-built LPBF components were also reported [63,67,192]. A further increase in energy densities (above 110 J/mm^3) resulted in a grain orientation shift towards the (100) plane with respect to the build direction. A stronger (100) texture is expected at very high

energy densities (VED > 150 J/mm^3). A (100) texture promotes epitaxial grain growth since it is well aligned with the preferential FCC crystal growth direction [193], supporting the presence of coarser grains and higher grain aspect ratio. A texture variation with energy density can be used to manipulate the mechanical properties of the as-fabricated structures [194].

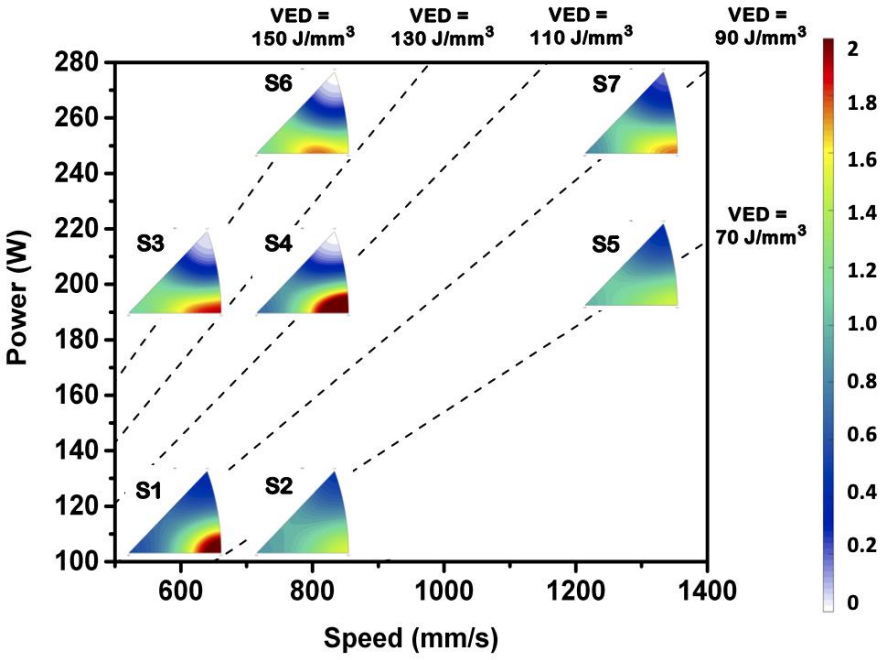

Figure 32. IPF maps of the S1-S7 specimens drawn over the PV map. The reference direction for the IPF maps is the build direction.

5.6 Microstructure dependence on the melt pool geometry

Complementing the rapid determination of processing conditions using the HT methodology, LT microstructural investigations can provide useful trends and physical insights, particularly as these features relate to the melt pool. A schematic model based on melt pool geometry is proposed to explain variations in the microstructures of the as-fabricated LPBF

components (Figure 33) [124]. In case 1, the lower VED values lead to a shallower melt pool and faster cooling [77,195]. As a result, grains nucleate and grow from the boundary and the center of the melt pool. Upon solidification, these grains will show overall finer grain sizes due to the multiple nucleation sites and more random texture due to the random distribution in the grain growth direction. This hypothesis is supported by the data collected at a relatively lower VED of 69.9 J/mm^3 where finer grains, lower grain aspect ratio, and finer dendritic microstructures were observed (Figure 33). These specimens also showed random texture along with higher average GB misorientations.

In case 2, medium range VED, a hemispherical melt pool forms coupled with a lower cooling rate than in case 1. In this case, grains nucleate only from the melt pool boundaries and grow along the heat flow direction. Upon solidification, these grains will have a relatively coarser grain size. For such melt pool shapes, the heat flow direction would be somewhere around 30-60 degrees with respect to building direction. Since FCC crystals have a preferential growth direction along [100] direction [193], most of the grains (~45 degrees) will have a (110) orientation along the planar surface. This hypothesis is supported by the experimental data at a VED of 113.6 J/mm^3, where both coarser grains and primary dendrite arm spacings were observed (Figure 31). These specimens also showed (110) plane crystallographic texture along the build direction.

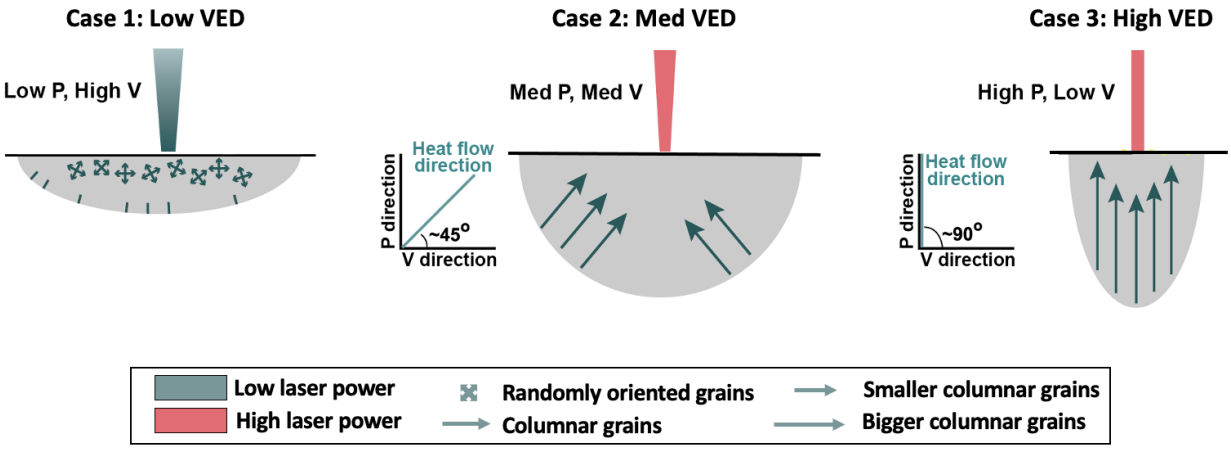

Figure 33. Microstructure dependence on the melt pool geometry of as-fabricated LPBF components. At lower VED, spherical grains having random texture forms (represented by the four-headed arrow). With increasing VED, increasing columnar grains form with a texture

In case 3 (Figure 33c), the high energy density leads to the formation of a deep melt pool coupled with the lowest cooling rate [77,195]. In this case, grains nucleate from the melt pool boundary and grow along the heat flow direction. Upon solidification, these grains will have the coarsest grain size and the coarsest dendrite arm spacing due to lower cooling rates. Since the laser speed is slower in this scenario, the laser power will have the most influence on the heat flow direction (i.e., (100)). Since FCC crystals grow preferentially along the [100] direction [193], most of the grains show crystallographic texture trending towards the (100) plane. The model presented is supported by experiments at a VED of 151.5 J/mm^3 where the coarsest average grain size of 35.1 µm and a primary dendrite arm spacing of 0.56 µm were observed (Figure 31). The grain aspect ratio was also 5.6 as compared to 2.7 at lower VED, and there was a higher fraction of low angle grain boundaries. The proposed melt pool model is further supported by the IPF maps (Figure 32). The crystallographic texture in the build direction started to shift from (110) to (100) plane as the VED increased.

5.7 Microstructure-hardness correlation

The microstructure of the as-fabricated specimens can promote change in the hardness and mechanical properties of a material. Common mechanisms to improve the strength of the as-fabricated AM materials include grain boundary strengthening, dislocation sub-structure strengthening, and dislocation density strengthening. Previous studies [12,196] have reported that the cellular dendritic solidification structures have a greater influence on yield strength than the grain size in LPBF-fabricated 316L SS. The effective strengthening is primarily due to the presence of dense dislocation networks in the interdendritic regions. The dependence of yield strength on primary dendrite arm spacing is given by the Hall-Petch relationship (refer to equation (51). For 316L values of σ_o and k_{HP} are 183.31 MPa and 253.66 MPa$\sqrt{\mu m}$, respectively [12] resulting in the equation:

$$\sigma_y = 183.31 + 253.66/\sqrt{PDAS} \tag{53}$$

Where $\sigma_y$is the yield strength (MPa) and $PDAS$ is the primary dendrite arm spacing (µm). Using equations (52 and (53, contributions of the primary dendrite arm spacing to the strengthening were estimated. Similarly, for different VED values, measured hardness values were calculated using equation (9. A comparison of the estimated yield strength and the measured hardness value is shown in Table 10. With an increase in VED from 70 to 150 J/mm^3 a drop of about 10% was observed in both the hardness and estimated yield strength value. The quick comparison suggests consistency between the measured hardness values (using the HT technique) and the contribution of the primary dendrite arm spacing to the estimated yield strength (using the LT technique). These results provide the basis for predicting the specimen's hardness and yield strength, solely based on input process parameters for 316L SS.

Table 10. Comparison of the estimated yield strength and the measured hardness value

VED (J/mm^3)	Measured PDAS (μm) (Eq. (52)	Calculated Yield Strength (MPa) (Eq. (53)	Measured Hardness (HRA) (Eq. (9)	% Drop in Yield Strength	% Drop in Hardness
69.1	0.39	589.34	49.51	--	--
90.9	0.43	569.37	48.31	3.39	2.42
113.5	0.47	551.49	47.07	6.42	4.93
149.6	0.54	527.47	45.08	10.54	8.94

5.8 Spall strength measurements

One of the important properties for defense, aerospace, and automotive applications is crashworthiness or dynamic damage resistance. As compared to uniaxial mechanical testing, these properties are more sensitive to porosity defects and printability [197,198]. Thus, spall strength evaluation for all of the LT specimens (mentioned in Table 11) was performed. A cylindrical specimen of diameter 20 mm and height 5 mm was used as a target specimen and a wrought 316L SS was used as an impactor. The impactor was accelerated with a velocity of 256-269 m/s using a single stage gas gun. The PDV probes helped in measuring the free surface velocity at different time intervals as shown in Figure 34(a).

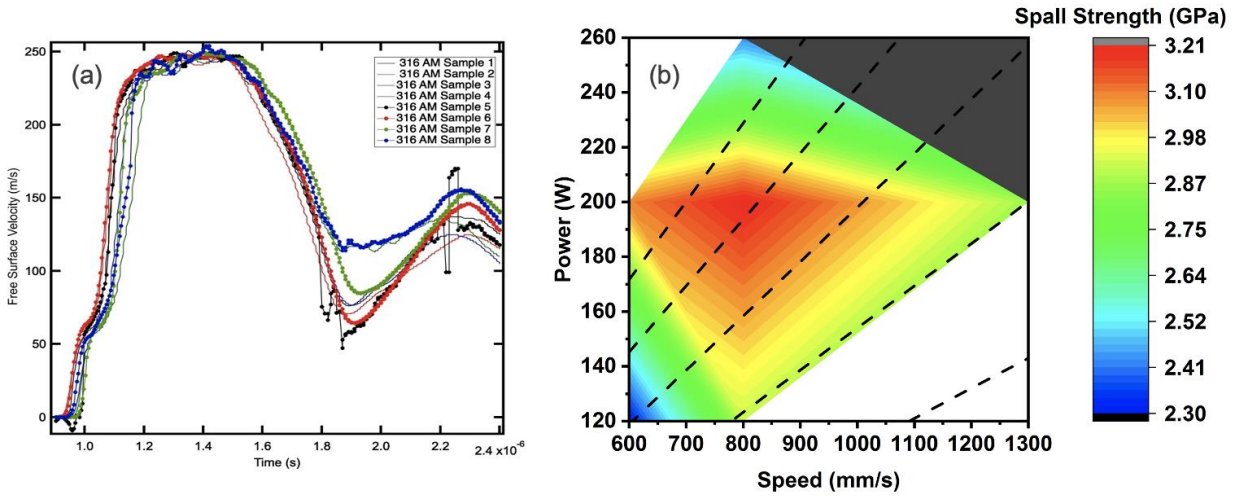

Figure 34. (a) Measured values of free surface velocity at different time intervals and (b) PV maps showing spall strength for LPBF 316L stainless steel

Table 11. Spall strength of additively manufactured 316L stainless steel

Sample number	Laser power (W)	Scanning speed (mm/s)	Hatch spacing (mm)	Volumetric energy density (J/mm^3)	Spall strength (GPa)
S1	120	600	0.07	142.86	2.96
S2	120	600	0.09	111.11	3.03
S3	120	600	0.11	90.91	2.30
S4	120	800	0.11	68.18	2.91
S5	200	600	0.11	151.52	3.09
S6	200	800	0.11	113.64	3.21
S7	200	1300	0.11	69.93	2.87
S8	260	800	0.11	147.73	2.43

PV based maps showing the spall strength of the additively manufactured 316L stainless steel were generated as shown in Figure 34b, and a summary of the processing conditions and the spall strength is shown in Table 11. Interestingly, the sample with the highest spall strength was also processed at the middle of the sweet spot i.e., with laser power of 200 W and scanning speed of 800 mm/s. This sample showed a high spall strength of 3.21 GPa which is 30-40% higher as compared to the samples processed at different processing conditions. Also, the LPBF samples showed about 25% higher spall strength than their wrought and conventionally manufactured counterparts [199].

Unlike hardness measurements (Figure 7), no dependence with volumetric energy density was observed suggesting a combination of competitive factors including porosity defects, microstructural features, and residual stress are affecting the dynamic response of a material [200,201]. A detailed study on the influence of processing parameters on dislocation density, stored energy, and residual stress are planned work (section 6.1). Still, the results from the dynamic response measurements suggested processing in the middle of the sweet spot and minimizing porosity defects can lead to optimal mechanical properties.

5.9 Laves phase distribution in Inconel 718 alloy

Laves phase i.e. $(Ni,Cr,Fe)_2(Nb,Mo)$ forms during the solidification of nickel-base superalloys [202]. Several studies have observed the presence of Laves phase in LPBF-fabricated IN 718 components [203,204]. These topological closed packed (TCP) structures are brittle and thus deteriorate the alloy's mechanical properties and provide an easy path for crack propagation. In addition, the Laves phases deplete the useful elements like Nb and Mo from the matrix resulting

in lesser volume fraction strengthening precipitates i.e., γ′′ (Ni_3Nb) [205]. Removal of Laves phase from the as-fabricated components is very difficult. Usually, to dissolve these phases, a high homogenization temperature of 1120-1180 ℃ is required during the post-heat treatment process causing excessive grain growth [206]. So, a better approach is to avoid or minimize the fraction of Laves phase during the solidification process itself.

The key idea behind the Laves phase minimization is the control over the solidification conditions and solute redistribution. During solidification, the Nb and Mo elements eject into the liquid region resulting in enriched elemental concentration at the solid-liquid interface. When the Nb concentration exceeds 20 wt.% the terminal liquid solidifies as Laves phase [205]. So, it would be interesting to apply LT microstructural analysis to nickel-base superalloys and quantify the dendritic arm spacing, solute concentration profile across the dendritic structure, and the fraction of Laves phase in each of the LT specimens.

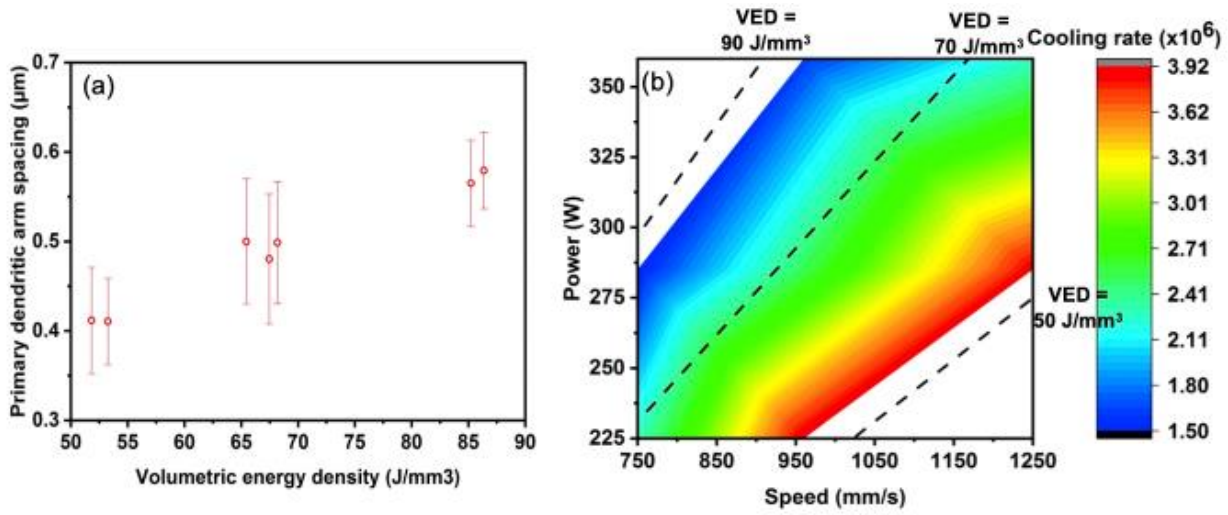

Figure 35. (a) Effect of volumetric energy density on primary dendritic arm spacing of IN 718 alloy and (b) Processing maps displaying estimated cooling rate values at different laser power and scanning speed.

Based on the HT experiments as discussed in sections 2.4 and 2.5, seven samples were selected for detailed microstructural analysis. The variation of primary dendritic arm spacing with volumetric energy density is shown in Figure 35a. It can be seen that with an increase in VED the dendritic arm spacing increases from 0.41 to 0.59 µm. An estimate of the cooling rate was made using the empirical relationship:

$$\lambda_1 = 97\ (\epsilon^{-0.36}) \tag{54}$$

Where λ_1 is the primary dendritic arm spacing and ϵ is the cooling rate. The process mapping of the estimated cooling rate is shown in Figure 35b. Similarly, thermal gradient (G) and solidification rate (R) were also calculated. The identification of the Laves phase and solute distribution was difficult to measure using SEM and EDAX mainly due to their nanoscale size as shown in Figure 36. In principle, TEM can help in obtaining both the pieces of information and planned work. This study highlights that the laser processing parameters offer great flexibility to design the as-fabricated microstructure and control the solidification route.

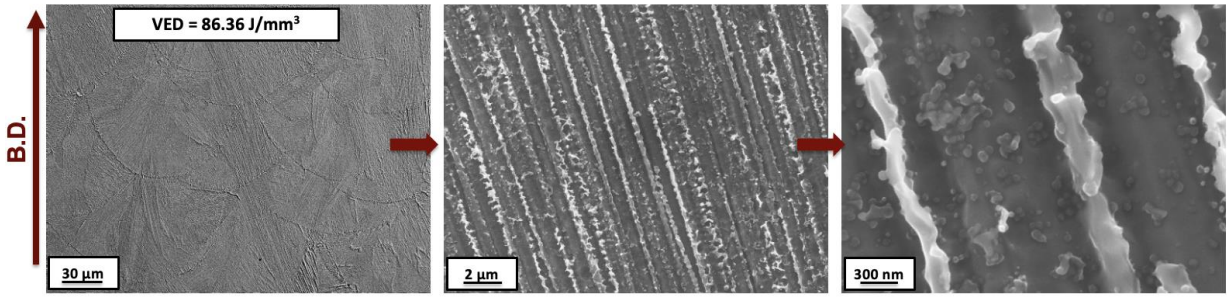

Figure 36. SEM imaging of as-built In718 samples showing the possibility of Laves phase in the inter dendritic region at higher VED ranges.

5.10 Conclusions

A comprehensive LT microstructural characterization was performed on the LPBF-fabricated 316L SS. Based on the results and analysis the following conclusions can be reached:

1. Energy densities permit microstructural design strategies with low-throughput studies.
    a) At lower energy densities of (VED = 69.9 J/mm^3) finer grains, low grain aspect ratios, finer dendritic structure, and more random texture was observed.
    b) As the energy density increased, coarser grains with higher grain aspect ratios were observed.
    c) Under a constant energy density, the microstructure remained unchanged.
2. The variation in microstructures at different energy densities can be explained in terms of melt pool geometry. Lower energy density results in a shallower melt pool and faster cooling rates lead to more randomly oriented, fine grain structures. Higher energy densities result in deeper melt pools and slower cooling rates, leading to coarse elongated grains with a texture towards (110) and (100) planes with respect to the build direction.
3. High-throughput regression of hardness as a function of volumetric energy density (VED) was consistent with a Hall-Petch relationship corresponding to the primary dendrite arm spacings (determined with low-throughput characterization).
4. Samples showed 30-40% improvement in dynamic failure response and a high spall strength of 3.21 GPa was observed when processed at the middle of the optimal processing window.
5. Laser processing parameters may offer a fabrication route to minimize Laves phase fraction in the Inconel 718 alloy.

Chapter 6: Future work

6.1 Stored energy and dislocation density measurements

Additive manufactured (AM) components often show high residual stresses mainly due to the rapid solidification, high thermal gradient, geometric constraints, and multiple thermal cycles during fabrication. In AM samples, dislocation densities can be as high as 10^{14}-10^{15} m^{-2} forming a dislocation cell along the interdendritic regions. These dislocation cell networks can give rise to unique mechanical properties and performance.

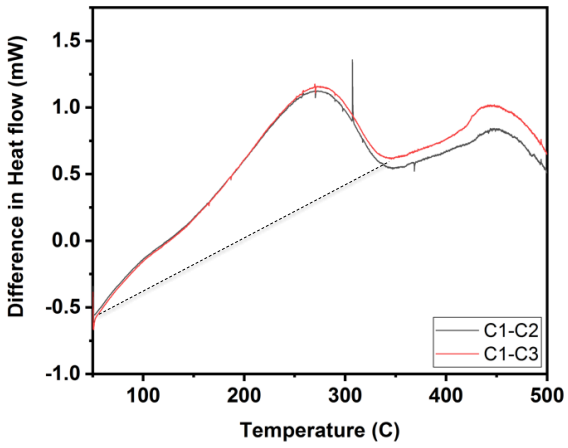

Figure 37. DSC analysis of additively manufactured 316L stainless steel. Samples were processed at VED = 70 J/mm^3.

An initial attempt on measuring the stored energy was performed using differential scanning calorimetry (DSC). Three cycles up to 550 ℃ were performed with a scan rate of 5 ℃/min. The first cycle was performed to evaluate the thermal signature. The second cycle was done to subtract the baseline (C1-C2), and the third cycle was a confirmation of the second cycle

(C1-C3). The results of the differential heat flow are shown below in Figure 37. Three distinct peaks were observed in the DSC curve with the third peak at 475 ℃ appearing to be incomplete. Stored energy was determined by calculating the area under the curve of the first two peaks. A similar analysis was performed on a few low-throughput samples (as listed in Table 9).

Dislocation densities measurements of the AM 316L SS were measured using neutron diffraction at Los Alamos National Laboratory. The processing parameters of these samples are listed in Table 9. The dependence of dislocation densities, dendritic arm spacing, stored energy, and transformation temperature calculated using DSC is shown in Figure 38.

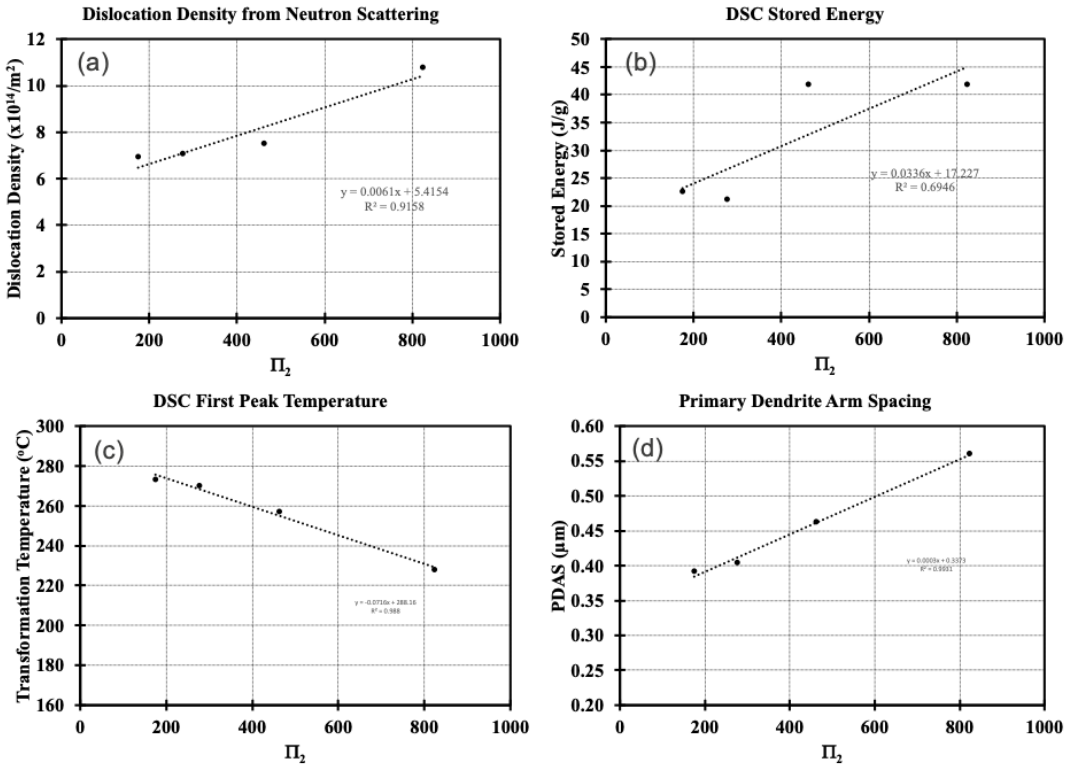

Figure 38. Variation of (a) dislocation densities (b) stored energy (c) transformation temperature of the major peak, and (d) primary dendritic arm spacing with dimensionless number for 316L stainless steel

Stored energy increases with the dimensionless number as shown in Figure 38b. This is consistent with a decrease in transformation peak temperature at a higher dimensionless number (Figure 38c) as at higher stored energy lower activation barrier would be required for dislocation annihilation. Also, dislocation densities increase with dimensionless numbers (Figure 38a). This suggests the dependence between dislocation density and stored energy. Also, a possibility to control residual stress in the LPBF components

Primary dendritic arm spacing increases with a dimensionless number (as shown in Figure 38d and similar to Figure 31). Interestingly, at a lower dimensionless number, finer dendritic arm spacing, higher cooling rate, and lower dislocation density were observed. Thus, there exists a potential competitive hardening mechanism associated with dislocation density and grain refinements. The data shown in Figure 38 represents a small subset within the processing window to make any conclusions. A detailed study on stored energy and dislocation density variation with processing parameters would be useful to understand the processing-structure-property-performance (PSPP) relationship in additive manufactured materials.

6.2 High throughput microstructural investigation

Most of the primary microstructural analysis undergoes a similar repetitive task. For example, metallographic practices, chemical etching, and imaging using optical or electron microscopy. Image analysis also requires similar repetitive measurements over multiple images gathered like spacing between the dendritic arm spacings and grain size calculations. It would be extremely useful if we can analyze multiple samples at once and would be an essential step toward autonomous materials research.

One of the potential ways to approach the problem is to machine out a small build plate of 6*6 inches and deposit multiple hex nut-shaped samples on them. Also, a smaller build plate will enable easy sample handlining, bulk sample polishing, and metallographic practices, and hold them within the optical and electron microscope without a need for sample cutting, machining, or mounting. In the LPBF process, high thermal stresses and cooling rates can warp the build plate if not properly clamped. Also, the tolerance limit for the distance between the build plate and recoater blade is extremely small. So, a flat polished and properly clamped build plate is essential.

A case example of a potential application of high throughput microstructural analysis is in the process design of Inconel 718. In718 are heat-treatable and precipitation-hardened alloys. In principle, HT microstructural analysis will enable to study of samples from a larger processing window and rapidly identify columnar-to-equiaxed transition regions. Generating solidification maps will help minimize the Laves phase concentration from the bulk sample. Also, the same build plate can be heat treated and analyzed again to optimize the heat treatment parameters and precipitates distribution. The data collected from the HT microstructural analysis can also be coupled with machine learning models to predict and design the microstructures.

References

[1] D. Herzog, V. Seyda, E. Wycisk, C. Emmelmann, Additive manufacturing of metals, Acta Mater. 117 (2016) 371–392. doi:10.1016/j.actamat.2016.07.019.

[2] W.E. Frazier, Metal additive manufacturing: A review, J. Mater. Eng. Perform. 23 (2014) 1917–1928. doi:10.1007/s11665-014-0958-z.

[3] W.J. Sames, F.A. List, S. Pannala, R.R. Dehoff, S.S. Babu, The metallurgy and processing science of metal additive manufacturing, Int. Mater. Rev. 61 (2016) 315–360. doi:10.1080/09506608.2015.1116649.

[4] C.Y. Yap, C.K. Chua, Z.L. Dong, Z.H. Liu, D.Q. Zhang, L.E. Loh, S.L. Sing, Review of selective laser melting: Materials and applications, Appl. Phys. Rev. 2 (2015) 041101. doi:10.1063/1.4935926.

[5] L.E. Murr, Metallurgy of additive manufacturing: Examples from electron beam melting, Addit. Manuf. 5 (2015) 40–53. doi:10.1016/j.addma.2014.12.002.

[6] S.M. Thompson, L. Bian, N. Shamsaei, A. Yadollahi, An overview of Direct Laser Deposition for additive manufacturing; Part I: Transport phenomena, modeling and diagnostics, Addit. Manuf. 8 (2015) 36–62. doi:10.1016/j.addma.2015.07.001.

[7] N. Shamsaei, A. Yadollahi, L. Bian, S.M. Thompson, An overview of Direct Laser Deposition for additive manufacturing; Part II: Mechanical behavior, process parameter optimization and control, Addit. Manuf. 8 (2015) 12–35. doi:10.1016/j.addma.2015.07.002.

[8] C. Zhang, F. Chen, Z. Huang, M. Jia, G. Chen, Y. Ye, Y. Lin, W. Liu, B. Chen, Q. Shen, L. Zhang, E.J. Lavernia, Additive manufacturing of functionally graded materials: A review, Mater. Sci. Eng. A. 764 (2019) 138209. doi:10.1016/j.msea.2019.138209.

[9] H. Fayazfar, M. Salarian, A. Rogalsky, D. Sarker, P. Russo, V. Paserin, E. Toyserkani, A critical review of powder-based additive manufacturing of ferrous alloys: Process parameters, microstructure and mechanical properties, Mater. Des. 144 (2018) 98–128. doi:10.1016/j.matdes.2018.02.018.

[10] https://www.eos.info/systems_solutions/software_data-preparation.

[11] C.-Y. Lin, T. Wirtz, F. LaMarca, S.J. Hollister, Structural and mechanical evaluations of a topology optimized titanium interbody fusion cage fabricated by selective laser melting process, J. Biomed. Mater. Res. A. 79 (2006) 963–73. doi:10.1002/jbm.a.30833.

[12] Y.M. Wang, T. Voisin, J.T. McKeown, J. Ye, N.P. Calta, Z. Li, Z. Zeng, Y. Zhang, W. Chen, T.T. Roehling, R.T. Ott, M.K. Santala, P.J. Depond, M.J. Matthews, A. V. Hamza, T. Zhu, Additively manufactured hierarchical stainless steels with high strength and ductility, Nat. Mater. 17 (2018) 63–70. doi:10.1038/NMAT5021.

[13] T. DebRoy, H.L. Wei, J.S. Zuback, T. Mukherjee, J.W. Elmer, J.O. Milewski, A.M. Beese, A. Wilson-Heid, A. De, W. Zhang, Additive manufacturing of metallic components – Process, structure and properties, Prog. Mater. Sci. 92 (2018) 112–224. doi:10.1016/j.pmatsci.2017.10.001.

[14] I. Wohlers Associates, Wohlers Report 2021 : 3D Printing and Additive Manufacturing Global State of the Industry, n.d.

[15] M. Seifi, A. Salem, J. Beuth, O. Harrysson, J.J. Lewandowski, Overview of Materials Qualification Needs for Metal Additive Manufacturing, Jom. 68 (2016) 747–764. doi:10.1007/s11837-015-1810-0.

[16] S.A. Khairallah, A.T. Anderson, A.M. Rubenchik, W.E. King, Laser powder-bed fusion additive manufacturing: Physics of complex melt flow and formation mechanisms of pores, spatter, and denudation zones, Addit. Manuf. Handb. Prod. Dev. Def. Ind. 108 (2017) 613–628. doi:10.1201/9781315119106.

[17] Y.S. Lee, W. Zhang, Modeling of heat transfer, fluid flow and solidification microstructure of nickel-base superalloy fabricated by laser powder bed fusion, Addit. Manuf. 12 (2016) 178–188. doi:10.1016/j.addma.2016.05.003.

[18] K.C. Mills, Recommended Values of Thermophysical Properties for Selected Commercial Alloys, 2002. doi:10.1533/9781845690144.

[19] Thermophysical Properties, in: Casting, ASM International, 2008: pp. 468–481. doi:10.31399/asm.hb.v15.a0005240.

[20] Properties of Metals, in: Met. Handb. Desk Ed., ASM International, 1998: pp. 114–121. doi:10.31399/asm.hb.mhde2.a0003086.

[21] R. Guschlbauer, S. Momeni, F. Osmanlic, C. Körner, Process development of 99.95% pure copper processed via selective electron beam melting and its mechanical and physical properties, Mater. Charact. 143 (2018) 163–170. doi:10.1016/j.matchar.2018.04.009.

[22] H.L. Wei, T. Mukherjee, W. Zhang, J.S. Zuback, G.L. Knapp, A. De, T. DebRoy, Mechanistic models for additive manufacturing of metallic components, Prog. Mater. Sci. 116 (2020). doi:10.1016/j.pmatsci.2020.100703.

[23] W.J. Boettinger, U.R. Kattner, K.-W. Moon, J.H. Perepezko, Dta and Heat-Flux Dsc Measurements of Alloy Melting and Freezing, Elsevier Ltd, 2007. doi:10.1016/b978-008044629-5/50005-7.

[24] H. Capacity, Flash Method of Determining Thermal Diffusivity, Encycl. Therm. Stress. 1679 (2014) 1683–1683. doi:10.1007/978-94-007-2739-7_100240.

[25] J. Trapp, A.M. Rubenchik, G. Guss, M.J. Matthews, In situ absorptivity measurements of metallic powders during laser powder-bed fusion additive manufacturing, Appl. Mater.

Today. 9 (2017) 341–349. doi:10.1016/j.apmt.2017.08.006.

[26] T. Maeji, K. Ibano, S. Yoshikawa, D. Inoue, S. Kuroyanagi, K. Mori, E. Hoashi, K. Yamanoi, N. Sarukura, Y. Ueda, Laser energy absorption coefficient and in-situ temperature measurement of laser-melted tungsten, Fusion Eng. Des. 124 (2017) 287–291. doi:10.1016/j.fusengdes.2017.04.025.

[27] J.J. Lewandowski, M. Seifi, Metal Additive Manufacturing: A Review of Mechanical Properties, Annu. Rev. Mater. Res. 46 (2016) 151–186. doi:10.1146/annurev-matsci-070115-032024.

[28] M.J. Bermingham, D.H. StJohn, J. Krynen, S. Tedman-Jones, M.S. Dargusch, Promoting the columnar to equiaxed transition and grain refinement of titanium alloys during additive manufacturing, Acta Mater. 168 (2019) 261–274. doi:10.1016/j.actamat.2019.02.020.

[29] H. Li, Y. Huang, S. Jiang, Y. Lu, X. Gao, X. Lu, Z. Ning, J. Sun, Columnar to equiaxed transition in additively manufactured CoCrFeMnNi high entropy alloy, Mater. Des. 197 (2021) 109262. doi:10.1016/j.matdes.2020.109262.

[30] Y. He, M. Zhong, N. Jones, J. Beuth, B. Webler, The Columnar-to-Equiaxed Transition in Melt Pools During Laser Powder Bed Fusion of M2 Steel, Metall. Mater. Trans. A. (2021). doi:10.1007/s11661-021-06380-9.

[31] T.U. Tumkur, T. Voisin, R. Shi, P.J. Depond, T.T. Roehling, S. Wu, M.F. Crumb, J.D. Roehling, G. Guss, S.A. Khairallah, M.J. Matthews, Nondiffractive beam shaping for enhanced optothermal control in metal additive manufacturing, Sci. Adv. 7 (2021) 1–12. doi:10.1126/sciadv.abg9358.

[32] T.T. Roehling, R. Shi, S.A. Khairallah, J.D. Roehling, G.M. Guss, J.T. McKeown, M.J. Matthews, Controlling grain nucleation and morphology by laser beam shaping in metal additive manufacturing, Mater. Des. 195 (2020) 109071. doi:10.1016/j.matdes.2020.109071.

[33] J.L. Bartlett, X. Li, An overview of residual stresses in metal powder bed fusion, Addit. Manuf. 27 (2019) 131–149. doi:10.1016/j.addma.2019.02.020.

[34] B. Cheng, S. Shrestha, K. Chou, Stress and deformation evaluations of scanning strategy effect in selective laser melting, Addit. Manuf. 12 (2016) 240–251. doi:10.1016/j.addma.2016.05.007.

[35] D. Buchbinder, W. Meiners, N. Pirch, K. Wissenbach, J. Schrage, Investigation on reducing distortion by preheating during manufacture of aluminum components using selective laser melting, J. Laser Appl. 26 (2014) 012004. doi:10.2351/1.4828755.

[36] J. Metelkova, Y. Kinds, K. Kempen, C. de Formanoir, A. Witvrouw, B. Van Hooreweder, On the influence of laser defocusing in Selective Laser Melting of 316L, Addit. Manuf. 23 (2018) 161–169. doi:10.1016/j.addma.2018.08.006.

[37] T.M. Pollock, A.J. Clarke, S.S. Babu, Design and Tailoring of Alloys for Additive Manufacturing, Metall. Mater. Trans. A Phys. Metall. Mater. Sci. 51 (2020) 6000–6019. doi:10.1007/s11661-020-06009-3.

[38] A.I. Saville, S.C. Vogel, A. Creuziger, J.T. Benzing, A.L. Pilchak, P. Nandwana, J. Klemm-Toole, K.D. Clarke, S.L. Semiatin, A.J. Clarke, Texture evolution as a function of scan strategy and build height in electron beam melted Ti-6Al-4V, Addit. Manuf. 46 (2021) 102118. doi:10.1016/j.addma.2021.102118.

[39] L.N. Carter, C. Martin, P.J. Withers, M.M. Attallah, The influence of the laser scan strategy on grain structure and cracking behaviour in SLM powder-bed fabricated nickel superalloy, J. Alloys Compd. 615 (2014) 338–347. doi:10.1016/j.jallcom.2014.06.172.

[40] M. Strantza, R.K. Ganeriwala, B. Clausen, T.Q. Phan, L.E. Levine, D.C. Pagan, C. Ruff, W.E. King, N.S. Johnson, R.M. Martinez, V. Anghel, G. Rafailov, D.W. Brown, Effect of the scanning strategy on the formation of residual stresses in additively manufactured Ti-6Al-4V, Addit. Manuf. 45 (2021) 102003. doi:10.1016/j.addma.2021.102003.

[41] A. du Plessis, I. Yadroitsava, I. Yadroitsev, Effects of defects on mechanical properties in metal additive manufacturing: A review focusing on X-ray tomography insights, Mater. Des. 187 (2020) 108385. doi:10.1016/j.matdes.2019.108385.

[42] K. Huang, C. Kain, N. Diaz-Vallejo, Y. Sohn, L. Zhou, High throughput mechanical testing platform and application in metal additive manufacturing and process optimization, J. Manuf. Process. 66 (2021) 494–505. doi:10.1016/j.jmapro.2021.04.027.

[43] A. Mostafaei, C. Zhao, Y. He, S. Reza Ghiaasiaan, B. Shi, S. Shao, N. Shamsaei, Z. Wu, N. Kouraytem, T. Sun, J. Pauza, J. V. Gordon, B. Webler, N.D. Parab, M. Asherloo, Q. Guo, L. Chen, A.D. Rollett, Defects and anomalies in powder bed fusion metal additive manufacturing, Curr. Opin. Solid State Mater. Sci. 26 (2022) 100974. doi:10.1016/j.cossms.2021.100974.

[44] J. V. Gordon, S.P. Narra, R.W. Cunningham, H. Liu, H. Chen, R.M. Suter, J.L. Beuth, A.D. Rollett, Defect structure process maps for laser powder bed fusion additive manufacturing, Addit. Manuf. 36 (2020) 101552. doi:10.1016/j.addma.2020.101552.

[45] S.M.H. Hojjatzadeh, N.D. Parab, W. Yan, Q. Guo, L. Xiong, C. Zhao, M. Qu, L.I. Escano, X. Xiao, K. Fezzaa, W. Everhart, T. Sun, L. Chen, Pore elimination mechanisms during 3D printing of metals, Nat. Commun. 10 (2019) 1–8. doi:10.1038/s41467-019-10973-9.

[46] H.D. Carlton, A. Haboub, G.F. Gallegos, D.Y. Parkinson, A.A. MacDowell, Damage evolution and failure mechanisms in additively manufactured stainless steel, Mater. Sci. Eng. A. 651 (2016) 406–414. doi:10.1016/j.msea.2015.10.073.

[47] T.R. Smith, J.D. Sugar, J.M. Schoenung, C. San Marchi, Relationship between manufacturing defects and fatigue properties of additive manufactured austenitic stainless

steel, Mater. Sci. Eng. A. 765 (2019) 138268. doi:10.1016/j.msea.2019.138268.

[48] M. Laleh, A.E. Hughes, S. Yang, J. Wang, J. Li, A.M. Glenn, W. Xu, M.Y. Tan, A critical insight into lack-of-fusion pore structures in additively manufactured stainless steel, Addit. Manuf. 38 (2021) 101762. doi:10.1016/j.addma.2020.101762.

[49] T. Mukherjee, T. DebRoy, Mitigation of lack of fusion defects in powder bed fusion additive manufacturing, J. Manuf. Process. 36 (2018) 442–449. doi:10.1016/j.jmapro.2018.10.028.

[50] T. Mukherjee, V. Manvatkar, A. De, T. DebRoy, Dimensionless numbers in additive manufacturing, J. Appl. Phys. 121 (2017) 064904. doi:10.1063/1.4976006.

[51] W.J. Sames, F. Medina, W.H. Peter, S.S. Babu, R.R. Dehoff, Effect of process control and powder quality on inconel 718 produced using electron beam melting, 8th Int. Symp. Superalloy 718 Deriv. 2014. (2014) 409–423. doi:10.1002/9781119016854.ch32.

[52] R. Li, J. Liu, Y. Shi, L. Wang, W. Jiang, Balling behavior of stainless steel and nickel powder during selective laser melting process, Int. J. Adv. Manuf. Technol. 59 (2012) 1025–1035. doi:10.1007/s00170-011-3566-1.

[53] W.E. King, H.D. Barth, V.M. Castillo, G.F. Gallegos, J.W. Gibbs, D.E. Hahn, C. Kamath, A.M. Rubenchik, Observation of keyhole-mode laser melting in laser powder-bed fusion additive manufacturing, J. Mater. Process. Technol. 214 (2014) 2915–2925. doi:10.1016/j.jmatprotec.2014.06.005.

[54] X. Yan, C. Chang, D. Dong, S. Gao, W. Ma, M. Liu, H. Liao, S. Yin, Microstructure and mechanical properties of pure copper manufactured by selective laser melting, Mater. Sci. Eng. A. 789 (2020) 139615. doi:10.1016/j.msea.2020.139615.

[55] I. Yadroitsev, A. Gusarov, I. Yadroitsava, I. Smurov, Single track formation in selective laser melting of metal powders, J. Mater. Process. Technol. 210 (2010) 1624–1631. doi:10.1016/j.jmatprotec.2010.05.010.

[56] I. Yadroitsev, P. Krakhmalev, I. Yadroitsava, S. Johansson, I. Smurov, Energy input effect on morphology and microstructure of selective laser melting single track from metallic powder, J. Mater. Process. Technol. 213 (2013) 606–613. doi:10.1016/j.jmatprotec.2012.11.014.

[57] W.E. King, A.T. Anderson, R.M. Ferencz, N.E. Hodge, C. Kamath, S.A. Khairallah, A.M. Rubenchik, Laser powder bed fusion additive manufacturing of metals; physics, computational, and materials challenges APPLIED PHYSICS REVIEWS Laser powder bed fusion additive manufacturing of metals; physics, computational, and materials challenges, Cit. Appl. Phys. Rev. 2 (2015) 41304. doi:10.1063/1.4937809.

[58] R. Cunningham, C. Zhao, N. Parab, C. Kantzos, J. Pauza, K. Fezzaa, T. Sun, A.D. Rollett, Keyhole threshold and morphology in laser melting revealed by ultrahigh-speed x-ray

imaging, Science (80-.). 363 (2019) 849–852. doi:10.1126/science.aav4687.

[59] U. Scipioni Bertoli, B.E. MacDonald, J.M. Schoenung, Stability of cellular microstructure in laser powder bed fusion of 316L stainless steel, Mater. Sci. Eng. A. 739 (2019) 109–117. doi:10.1016/j.msea.2018.10.051.

[60] L. Liu, Q. Ding, Y. Zhong, J. Zou, J. Wu, Y.-L. Chiu, J. Li, Z. Zhang, Q. Yu, Z. Shen, Dislocation network in additive manufactured steel breaks strength–ductility trade-off, Mater. Today. 21 (2018) 354–361. doi:10.1016/j.mattod.2017.11.004.

[61] K.M. Bertsch, G. Meric de Bellefon, B. Kuehl, D.J. Thoma, Origin of dislocation structures in an additively manufactured austenitic stainless steel 316L, Acta Mater. 199 (2020) 19–33. doi:10.1016/j.actamat.2020.07.063.

[62] T.R. Smith, J.D. Sugar, C. San Marchi, J.M. Schoenung, Strengthening mechanisms in directed energy deposited austenitic stainless steel, Acta Mater. 164 (2019) 728–740. doi:10.1016/j.actamat.2018.11.021.

[63] O. Andreau, I. Koutiri, P. Peyre, J.-D. Penot, N. Saintier, E. Pessard, T. De Terris, C. Dupuy, T. Baudin, Texture control of 316L parts by modulation of the melt pool morphology in selective laser melting, J. Mater. Process. Technol. 264 (2019) 21–31. doi:10.1016/j.jmatprotec.2018.08.049.

[64] M. Moorehead, K. Bertsch, M. Niezgoda, C. Parkin, M. Elbakhshwan, K. Sridharan, C. Zhang, D. Thoma, A. Couet, High-throughput synthesis of Mo-Nb-Ta-W high-entropy alloys via additive manufacturing, Mater. Des. 187 (2020) 108358. doi:10.1016/j.matdes.2019.108358.

[65] F. Ren, L. Ward, T. Williams, K.J. Laws, C. Wolverton, J. Hattrick-Simpers, A. Mehta, Accelerated discovery of metallic glasses through iteration of machine learning and high-throughput experiments, Sci. Adv. 4 (2018) 1566. doi:10.1126/sciadv.aaq1566.

[66] T.T. Ikeshoji, K. Nakamura, M. Yonehara, K. Imai, H. Kyogoku, Selective Laser Melting of Pure Copper, Jom. 70 (2018) 396–400. doi:10.1007/s11837-017-2695-x.

[67] V. Livescu, C.M. Knapp, G.T. Gray, R.M. Martinez, B.M. Morrow, B.G. Ndefru, Additively manufactured tantalum microstructures, Materialia. 1 (2018) 15–24. doi:10.1016/j.mtla.2018.06.007.

[68] I.E. Anderson, E.M.H. White, R. Dehoff, Feedstock powder processing research needs for additive manufacturing development, Curr. Opin. Solid State Mater. Sci. 22 (2018) 8–15. doi:10.1016/j.cossms.2018.01.002.

[69] B. Rankouhi, K.M. Bertsch, G. Meric de Bellefon, M. Thevamaran, D.J. Thoma, K. Suresh, Experimental validation and microstructure characterization of topology optimized, additively manufactured SS316L components, Mater. Sci. Eng. A. 776 (2020) 139050. doi:10.1016/j.msea.2020.139050.

[70] R. Seede, D. Shoukr, B. Zhang, A. Whitt, S. Gibbons, P. Flater, A. Elwany, R. Arroyave, I. Karaman, An ultra-high strength martensitic steel fabricated using selective laser melting additive manufacturing: Densification, microstructure, and mechanical properties, Acta Mater. 186 (2020) 199–214. doi:10.1016/j.actamat.2019.12.037.

[71] M. Shamsujjoha, S.R. Agnew, J.M. Fitz-Gerald, W.R. Moore, T.A. Newman, High Strength and Ductility of Additively Manufactured 316L Stainless Steel Explained, Metall. Mater. Trans. A Phys. Metall. Mater. Sci. 49 (2018) 3011–3027. doi:10.1007/s11661-018-4607-2.

[72] Z. Li, B. He, Q. Guo, Strengthening and hardening mechanisms of additively manufactured stainless steels: The role of cell sizes, Scr. Mater. 177 (2020) 17–21. doi:10.1016/j.scriptamat.2019.10.005.

[73] M.S. Pham, B. Dovgyy, P.A. Hooper, Twinning induced plasticity in austenitic stainless steel 316L made by additive manufacturing, Mater. Sci. Eng. A. 704 (2017) 102–111. doi:10.1016/j.msea.2017.07.082.

[74] A. Riemer, S. Leuders, M. Thöne, H.A. Richard, T. Tröster, T. Niendorf, On the fatigue crack growth behavior in 316L stainless steel manufactured by selective laser melting, Eng. Fract. Mech. 120 (2014) 15–25. doi:10.1016/j.engfracmech.2014.03.008.

[75] Y.J. Yin, J.Q. Sun, J. Guo, X.F. Kan, D.C. Yang, Mechanism of high yield strength and yield ratio of 316 L stainless steel by additive manufacturing, Mater. Sci. Eng. A. 744 (2019) 773–777. doi:10.1016/j.msea.2018.12.092.

[76] Z. Wang, T.A. Palmer, A.M. Beese, Effect of processing parameters on microstructure and tensile properties of austenitic stainless steel 304L made by directed energy deposition additive manufacturing, Acta Mater. 110 (2016) 226–235. doi:10.1016/j.actamat.2016.03.019.

[77] C. Zhao, K. Fezzaa, R.W. Cunningham, H. Wen, F. De Carlo, L. Chen, A.D. Rollett, T. Sun, Real-time monitoring of laser powder bed fusion process using high-speed X-ray imaging and diffraction, Sci. Rep. 7 (2017) 1–11. doi:10.1038/s41598-017-03761-2.

[78] T. Sun, W. Tan, L. Chen, A. Rollett, In situ/operando synchrotron x-ray studies of metal additive manufacturing, MRS Bull. 45 (2020) 927–933. doi:10.1557/mrs.2020.275.

[79] A.A. Martin, N.P. Calta, S.A. Khairallah, J. Wang, P.J. Depond, A.Y. Fong, V. Thampy, G.M. Guss, A.M. Kiss, K.H. Stone, C.J. Tassone, J. Nelson Weker, M.F. Toney, T. van Buuren, M.J. Matthews, Dynamics of pore formation during laser powder bed fusion additive manufacturing, Nat. Commun. 10 (2019) 1987. doi:10.1038/s41467-019-10009-2.

[80] Z.A. Young, Q. Guo, N.D. Parab, C. Zhao, M. Qu, L.I. Escano, K. Fezzaa, W. Everhart, T. Sun, L. Chen, Types of spatter and their features and formation mechanisms in laser powder bed fusion additive manufacturing process, Addit. Manuf. 36 (2020) 101438. doi:10.1016/j.addma.2020.101438.

[81] Q. Guo, C. Zhao, M. Qu, L. Xiong, L.I. Escano, S.M.H. Hojjatzadeh, N.D. Parab, K. Fezzaa, W. Everhart, T. Sun, L. Chen, In-situ characterization and quantification of melt pool variation under constant input energy density in laser powder bed fusion additive manufacturing process, Addit. Manuf. 28 (2019) 600–609. doi:10.1016/j.addma.2019.04.021.

[82] L. Zheng, Q. Zhang, H. Cao, W. Wu, H. Ma, X. Ding, J. Yang, X. Duan, S. Fan, Melt pool boundary extraction and its width prediction from infrared images in selective laser melting, Mater. Des. 183 (2019) 108110. doi:10.1016/j.matdes.2019.108110.

[83] Z. jue Tang, W. wei Liu, Y. wen Wang, K.M. Saleheen, Z. chao Liu, S. tong Peng, Z. Zhang, H. chao Zhang, A review on in situ monitoring technology for directed energy deposition of metals, Int. J. Adv. Manuf. Technol. 108 (2020) 3437–3463. doi:10.1007/s00170-020-05569-3.

[84] T. Mukherjee, H.L. Wei, A. De, T. DebRoy, Heat and fluid flow in additive manufacturing – Part II: Powder bed fusion of stainless steel, and titanium, nickel and aluminum base alloys, Comput. Mater. Sci. 150 (2018) 369–380. doi:10.1016/j.commatsci.2018.04.027.

[85] T. DebRoy, T. Mukherjee, H.L. Wei, J.W. Elmer, J.O. Milewski, Metallurgy, mechanistic models and machine learning in metal printing, Nat. Rev. Mater. (2020). doi:10.1038/s41578-020-00236-1.

[86] T. Mukherjee, J.S. Zuback, A. De, T. DebRoy, Printability of alloys for additive manufacturing, Sci. Rep. 6 (2016) 1–8. doi:10.1038/srep19717.

[87] A.M. Rubenchik, W.E. King, S.S. Wu, Scaling laws for the additive manufacturing, J. Mater. Process. Technol. 257 (2018) 234–243. doi:10.1016/j.jmatprotec.2018.02.034.

[88] B. Cheng, J. Lydon, K. Cooper, V. Cole, P. Northrop, K. Chou, Melt pool sensing and size analysis in laser powder-bed metal additive manufacturing, J. Manuf. Process. 32 (2018) 744–753. doi:10.1016/j.jmapro.2018.04.002.

[89] D.R. Clymer, J. Cagan, J. Beuth, Power–Velocity Process Design Charts for Powder Bed Additive Manufacturing, J. Mech. Des. 139 (2017) 100907. doi:10.1115/1.4037302.

[90] M. Thomas, G.J. Baxter, I. Todd, Normalised model-based processing diagrams for additive layer manufacture of engineering alloys, Acta Mater. 108 (2016) 26–35. doi:10.1016/j.actamat.2016.02.025.

[91] L. Johnson, M. Mahmoudi, B. Zhang, R. Seede, X. Huang, J.T. Maier, H.J. Maier, I. Karaman, A. Elwany, R. Arróyave, Assessing printability maps in additive manufacturing of metal alloys, Acta Mater. 176 (2019) 199–210. doi:10.1016/j.actamat.2019.07.005.

[92] R.P. Hertzberg, A.J. Pope, High-throughput screening: New technology for the 21st century, Curr. Opin. Chem. Biol. 4 (2000) 445–451. doi:10.1016/S1367-5931(00)00110-1.

[93] W.W. Soon, M. Hariharan, M.P. Snyder, High-throughput sequencing for biology and medicine, Mol. Syst. Biol. 9 (2013) 1–14. doi:10.1038/msb.2012.61.

[94] M. Kircher, J. Kelso, High-throughput DNA sequencing - Concepts and limitations, BioEssays. 32 (2010) 524–536. doi:10.1002/bies.200900181.

[95] M.L. Green, C.L. Choi, J.R. Hattrick-Simpers, A.M. Joshi, I. Takeuchi, S.C. Barron, E. Campo, T. Chiang, S. Empedocles, J.M. Gregoire, A.G. Kusne, J. Martin, A. Mehta, K. Persson, Z. Trautt, J. Van Duren, A. Zakutayev, Fulfilling the promise of the materials genome initiative with high-throughput experimental methodologies, Appl. Phys. Rev. 4 (2017) 011105. doi:10.1063/1.4977487.

[96] J.R. Hattrick-Simpers, J.M. Gregoire, A.G. Kusne, Perspective: Composition-structure-property mapping in high-throughput experiments: Turning data into knowledge, APL Mater. 4 (2016) 053211. doi:10.1063/1.4950995.

[97] D.B. Miracle, M. Li, Z. Zhang, R. Mishra, K.M. Flores, Emerging Capabilities for the High-Throughput Characterization of Structural Materials, Annu. Rev. Mater. Res. 51 (2021) 131–164. doi:10.1146/annurev-matsci-080619-022100.

[98] O.F. Dippo, K.R. Kaufmann, K.S. Vecchio, High-Throughput Rapid Experimental Alloy Development (HT-READ), Acta Mater. 221 (2021) 117352. doi:10.1016/j.actamat.2021.117352.

[99] R. Liu, A. Kumar, Z. Chen, A. Agrawal, V. Sundararaghavan, A. Choudhary, A predictive machine learning approach for microstructure optimization and materials design, Sci. Rep. 5 (2015) 1–12. doi:10.1038/srep11551.

[100] R. Ramprasad, R. Batra, G. Pilania, A. Mannodi-Kanakkithodi, C. Kim, Machine learning in materials informatics: Recent applications and prospects, Npj Comput. Mater. 3 (2017) 54. doi:10.1038/s41524-017-0056-5.

[101] Z. Islam, P. Nelaturu, D.J. Thoma, A dimensionless number for high-throughput design of multi-principal element alloys in directed energy deposition, Appl. Phys. Lett. 119 (2021) 231901. doi:10.1063/5.0069384.

[102] M. Moorehead, P. Nelaturu, M. Elbakhshwan, C. Parkin, C. Zhang, K. Sridharan, D.J. Thoma, A. Couet, High-throughput ion irradiation of additively manufactured compositionally complex alloys, J. Nucl. Mater. 547 (2021) 152782. doi:10.1016/j.jnucmat.2021.152782.

[103] M.A. Melia, S.R. Whetten, R. Puckett, M. Jones, M.J. Heiden, N. Argibay, A.B. Kustas, High-throughput additive manufacturing and characterization of refractory high entropy alloys, Appl. Mater. Today. 19 (2020) 100560. doi:10.1016/j.apmt.2020.100560.

[104] N.M. Heckman, T.A. Ivanoff, A.M. Roach, B.H. Jared, D.J. Tung, H.J. Brown-Shaklee, T. Huber, D.J. Saiz, J.R. Koepke, J.M. Rodelas, J.D. Madison, B.C. Salzbrenner, L.P. Swiler,

R.E. Jones, B.L. Boyce, Automated high-throughput tensile testing reveals stochastic process parameter sensitivity, Mater. Sci. Eng. A. 772 (2020) 138632. doi:10.1016/j.msea.2019.138632.

[105] B.C. Salzbrenner, J.M. Rodelas, J.D. Madison, B.H. Jared, L.P. Swiler, Y.L. Shen, B.L. Boyce, High-throughput stochastic tensile performance of additively manufactured stainless steel, J. Mater. Process. Technol. 241 (2017) 1–12. doi:10.1016/j.jmatprotec.2016.10.023.

[106] R. Jafari-Marandi, M. Khanzadeh, W. Tian, B. Smith, L. Bian, From in-situ monitoring toward high-throughput process control: cost-driven decision-making framework for laser-based additive manufacturing, J. Manuf. Syst. 51 (2019) 29–41. doi:10.1016/j.jmsy.2019.02.005.

[107] S.W. Hughes, Archimedes revisited: A faster, better, cheaper method of accurately measuring the volume of small objects, Phys. Educ. 40 (2005) 468–474. doi:10.1088/0031-9120/40/5/008.

[108] ASTM International, Standard Test Methods for Density of Compacted or Sintered Powder Metallurgy (PM) Products Using Archimedes' Principle, Astm B962-17. (2013) 1–7. doi:10.1520/B0962-17.

[109] U. Scipioni Bertoli, A.J. Wolfer, M.J. Matthews, J.P.R. Delplanque, J.M. Schoenung, On the limitations of Volumetric Energy Density as a design parameter for Selective Laser Melting, Mater. Des. 113 (2017) 331–340. doi:10.1016/j.matdes.2016.10.037.

[110] K.G. Prashanth, S. Scudino, T. Maity, J. Das, J. Eckert, Is the energy density a reliable parameter for materials synthesis by selective laser melting?, Mater. Res. Lett. 5 (2017) 386–390. doi:10.1080/21663831.2017.1299808.

[111] E. Buckingham, On physically similar systems; Illustrations of the use of dimensional equations, Phys. Rev. 4 (1914) 345–376. doi:10.1103/PhysRev.4.345.

[112] Z. Wang, M. Liu, Dimensionless analysis on selective laser melting to predict porosity and track morphology, J. Mater. Process. Tech. 273 (2019) 116238. doi:10.1016/j.jmatprotec.2019.05.019.

[113] M. Van Elsen, F. Al-Bender, J.P. Kruth, Application of dimensional analysis to selective laser melting, Rapid Prototyp. J. 14 (2008) 15–22. doi:10.1108/13552540810841526.

[114] B. Rankouhi, A.K. Agrawal, F.E. Pfefferkorn, D.J. Thoma, A dimensionless number for predicting universal processing parameter boundaries in metal powder bed additive manufacturing, Manuf. Lett. 27 (2021) 13–17. doi:10.1016/j.mfglet.2020.12.002.

[115] R. Fabbro, Scaling laws for the laser welding process in keyhole mode, J. Mater. Process. Technol. 264 (2019) 346–351. doi:10.1016/j.jmatprotec.2018.09.027.

[116] M. Qu, Q. Guo, L.I. Escano, A. Nabaa, S.M.H. Hojjatzadeh, Z.A. Young, L. Chen, Controlling process instability for defect lean metal additive manufacturing, Nat. Commun. 13 (2022) 1–8. doi:10.1038/s41467-022-28649-2.

[117] R. Sheshadri, M. Nagaraj, A. Lakshmikanthan, M.P. Gowdru Chandrashekarappa, D.Y. Pimenov, K. Giasin, P. Raghupatruni, S. Wojciechowski, Experimental Investigation of Selective Laser Melting Parameters for Higher Surface Quality and Microhardness Properties: Taguchi and Super Ranking Concept Approaches, J. Mater. Res. Technol. 14 (2021) 2586–2600. doi:10.1016/j.jmrt.2021.07.144.

[118] M. Yonehara, C. Kato, T.T. Ikeshoji, K. Takeshita, Correlation between surface texture and internal defects in laser powder - bed fusion additive manufacturing, Sci. Rep. (2021) 1–10. doi:10.1038/s41598-021-02240-z.

[119] U. Ali, R. Esmaeilizadeh, F. Ahmed, D. Sarker, W. Muhammad, A. Keshavarzkermani, Y. Mahmoodkhani, E. Marzbanrad, E. Toyserkani, Identification and characterization of spatter particles and their effect on surface roughness, density and mechanical response of 17-4 PH stainless steel laser powder-bed fusion parts, Mater. Sci. Eng. A. 756 (2019) 98–107. doi:10.1016/j.msea.2019.04.026.

[120] C. Kantzos, J. Lao, A. Rollett, Design of an interpretable Convolutional Neural Network for stress concentration prediction in rough surfaces, Mater. Charact. 158 (2019) 109961. doi:10.1016/j.matchar.2019.109961.

[121] H. Zhang, M. Xu, Z. Liu, C. Li, P. Kumar, Z. Liu, Y. Zhang, Microstructure, surface quality, residual stress, fatigue behavior and damage mechanisms of selective laser melted 304L stainless steel considering building direction, Addit. Manuf. 46 (2021) 102147. doi:10.1016/j.addma.2021.102147.

[122] L. Chen, B. Richter, X. Zhang, K.B. Bertsch, D.J. Thoma, F.E. Pfefferkorn, Effect of laser polishing on the microstructure and mechanical properties of stainless steel 316L fabricated by laser powder bed fusion, Mater. Sci. Eng. A. 802 (2020) 140579. doi:10.1016/j.msea.2020.140579.

[123] D. Wang, Y. Liu, Y. Yang, D. Xiao, Theoretical and experimental study on surface roughness of 316L stainless steel metal parts obtained through selective laser melting, Rapid Prototyp. J. 22 (2016) 706–716. doi:10.1108/RPJ-06-2015-0078.

[124] A.K. Agrawal, G. Meric de Bellefon, D. Thoma, High-throughput experimentation for microstructural design in additively manufactured 316L stainless steel, Mater. Sci. Eng. A. 793 (2020) 139841. doi:10.1016/j.msea.2020.139841.

[125] ASTM International, Standard Test Methods for Tension Testing of Metallic Materials, ASTM E8 / E8M-08. (2013) 1–25. doi:10.1520/E0008_E0008M.

[126] Z. Islam, A.K. Agrawal, B. Rankouhi, C. Magnin, M.H. Anderson, F.E. Pfefferkorn, D.J.

Thoma, A High-Throughput Method to Define Additive Manufacturing Process Parameters: Application to Haynes 282, Metall. Mater. Trans. A. 53 (2022) 250–263. doi:10.1007/s11661-021-06517-w.

[127] T. DebRoy, T. Mukherjee, H.L. Wei, J.W. Elmer, J.O. Milewski, Metallurgy, mechanistic models and machine learning in metal printing, Nat. Rev. Mater. 6 (2021) 48–68. doi:10.1038/s41578-020-00236-1.

[128] A.K. Agrawal, B. Rankouhi, D.J. Thoma, Predictive process mapping for laser powder bed fusion: A review of existing analytical solutions, Curr. Opin. Solid State Mater. Sci. 26 (2022) 101024. doi:10.1016/j.cossms.2022.101024.

[129] L. Scime, J. Beuth, Melt pool geometry and morphology variability for the Inconel 718 alloy in a laser powder bed fusion additive manufacturing process, Addit. Manuf. 29 (2019) 100830. doi:10.1016/j.addma.2019.100830.

[130] H. Choo, K.L. Sham, J. Bohling, A. Ngo, X. Xiao, Y. Ren, P.J. Depond, M.J. Matthews, E. Garlea, Effect of laser power on defect, texture, and microstructure of a laser powder bed fusion processed 316L stainless steel, Mater. Des. 164 (2019) 107534. doi:10.1016/j.matdes.2018.12.006.

[131] T. Kurzynowski, K. Gruber, W. Stopyra, B. Kuźnicka, E. Chlebus, Correlation between process parameters, microstructure and properties of 316 L stainless steel processed by selective laser melting, Mater. Sci. Eng. A. 718 (2018) 64–73. doi:10.1016/j.msea.2018.01.103.

[132] S.C. Jensen, J.R. Koepke, D.J. Saiz, M. Heiden, J.D. Carroll, B.L. Boyce, B.H. Jared, Optimization of Stochastic Feature Properties in Laser Powder Bed Fusion, Addit. Manuf. 56 (2022) 102943. doi:10.1016/j.addma.2022.102943.

[133] H.E. Sabzi, E. Hernandez-Nava, X.-H. Li, H. Fu, D. San-Martín, P.E.J. Rivera-Díaz-del-Castillo, Strengthening control in laser powder bed fusion of austenitic stainless steels via grain boundary engineering, Mater. Des. 212 (2021) 110246. doi:10.1016/j.matdes.2021.110246.

[134] M.W. McDonald, W.S. Gora, S.G. Stevenson, N.J. Weston, D.P. Hand, Practical implementation of laser polishing on additively manufactured metallic components, J. Laser Appl. 32 (2020) 042019. doi:10.2351/7.0000222.

[135] R. Ostholt, E. Willenborg, K. Wissenbach, Laser polishing of metallic freeform surfaces, 29th Int. Congr. Appl. Lasers Electro-Optics, ICALEO 2010 - Congr. Proc. 103 (2010) 597–603. doi:10.2351/1.5062086.

[136] B. Liu, B.Q. Li, Z. Li, Selective laser remelting of an additive layer manufacturing process on AlSi10Mg, Results Phys. 12 (2019) 982–988. doi:10.1016/j.rinp.2018.12.018.

[137] Y. Tian, W.S. Gora, A.P. Cabo, L.L. Parimi, D.P. Hand, S. Tammas-Williams, P.B.

Prangnell, Material interactions in laser polishing powder bed additive manufactured Ti6Al4V components, Addit. Manuf. 20 (2018) 11–22. doi:10.1016/j.addma.2017.12.010.

[138] P.J. Faue, L.H. Beste, B. Richter, A. Agrawal, K. Klingbeil, D. Thoma, T. Radel, F.E. Pfefferkorn, Influence of laser polishing on fatigue life of conventionally machined and laser powder bed fusion 316L stainless steel, Manuf. Lett. 33 (2022) 670–677. doi:10.1016/j.mfglet.2022.07.083.

[139] H. Ghasemi-Tabasi, J. Jhabvala, E. Boillat, T. Ivas, R. Drissi-Daoudi, R.E. Logé, An effective rule for translating optimal selective laser melting processing parameters from one material to another, Addit. Manuf. 36 (2020) 101496. doi:10.1016/j.addma.2020.101496.

[140] V. Semak, A. Matsunawa, The role of recoil pressure in energy balance during laser materials processing, J. Phys. D. Appl. Phys. 30 (1997) 2541–2552. doi:10.1088/0022-3727/30/18/008.

[141] B.J. Keene, Review of data for the surface tension of pure metals, Int. Mater. Rev. 38 (1993) 157–192. doi:10.1179/imr.1993.38.4.157.

[142] T. Debroy, S.A. David, Physical processes in fusion welding, Rev. Mod. Phys. 67 (1995) 85–112. doi:10.1103/RevModPhys.67.85.

[143] D. Rosenthal, Mathematical Theory of Heat Distribution during Welding and Cutting, Weld. J. 20 (1941).

[144] R. Fabbro, M. Dal, P. Peyre, F. Coste, M. Schneider, V. Gunenthiram, Analysis and possible estimation of keyhole depths evolution, using laser operating parameters and material properties, J. Laser Appl. 30 (2018) 032410. doi:10.2351/1.5040624.

[145] S.D. Jadhav, L.R. Goossens, Y. Kinds, B. Van Hooreweder, K. Vanmeensel, Laser-based powder bed fusion additive manufacturing of pure copper, Addit. Manuf. 42 (2021). doi:10.1016/j.addma.2021.101990.

[146] M. Tang, P.C. Pistorius, J.L. Beuth, Prediction of lack-of-fusion porosity for powder bed fusion, Addit. Manuf. 14 (2017) 39–48. doi:10.1016/j.addma.2016.12.001.

[147] M. Tang, P.C. Pistorius, J. Beuth, Geometric model to predict porosity of part produced in powder bed system, Mater. Sci. Technol. Proc. (2015) 129–136.

[148] A. Kumar, T. Debroy, Toward a unified model to prevent humping defects in gas tungsten arc welding, Weld. J. (Miami, Fla). 85 (2006).

[149] X. Meng, G. Qin, Z. Zou, Characterization of molten pool behavior and humping formation tendency in high-speed gas tungsten arc welding, Int. J. Heat Mass Transf. 117 (2018) 508–516. doi:10.1016/j.ijheatmasstransfer.2017.09.124.

[150] A.M. Kiss, A.Y. Fong, N.P. Calta, V. Thampy, A.A. Martin, P.J. Depond, J. Wang, M.J.

Matthews, R.T. Ott, C.J. Tassone, K.H. Stone, M.J. Kramer, A. van Buuren, M.F. Toney, J. Nelson Weker, Laser-Induced Keyhole Defect Dynamics during Metal Additive Manufacturing, Adv. Eng. Mater. 1900455 (2019) 1900455. doi:10.1002/adem.201900455.

[151] Z.C. Fang, Z.L. Wu, C.G. Huang, C.W. Wu, Review on residual stress in selective laser melting additive manufacturing of alloy parts, Opt. Laser Technol. 129 (2020) 106283. doi:10.1016/j.optlastec.2020.106283.

[152] J. Plocher, A. Panesar, Review on design and structural optimisation in additive manufacturing: Towards next-generation lightweight structures, Mater. Des. 183 (2019). doi:10.1016/j.matdes.2019.108164.

[153] W. Chen, T. Voisin, Y. Zhang, J.B. Florien, C.M. Spadaccini, D.L. McDowell, T. Zhu, Y.M. Wang, Microscale residual stresses in additively manufactured stainless steel, Nat. Commun. 10 (2019) 1–12. doi:10.1038/s41467-019-12265-8.

[154] W.L. Smith, J.D. Roehling, M. Strantza, R.K. Ganeriwala, A.S. Ashby, B. Vrancken, G.M. Guss, D.W. Brown, J.T. Mckeown, M.R. Hill, M.J. Matthews, Residual stress analysis of in situ surface layer heating effects on laser powder bed fusion of 316L stainless steel, 47 (2021). doi:10.1016/j.addma.2021.102252.

[155] A.S. Wu, D.W. Brown, M. Kumar, G.F. Gallegos, W.E. King, An Experimental Investigation into Additive Manufacturing-Induced Residual Stresses in 316L Stainless Steel, Metall. Mater. Trans. A Phys. Metall. Mater. Sci. 45 (2014) 6260–6270. doi:10.1007/s11661-014-2549-x.

[156] Z. Gan, O.L. Kafka, N. Parab, C. Zhao, O. Heinonen, T. Sun, W. Liu, Universal low-dimensional scaling laws in 3D printing of metals, 2020.

[157] S. Kou, A criterion for cracking during solidification, Acta Mater. 88 (2015) 366–374. doi:10.1016/j.actamat.2015.01.034.

[158] S. Kou, A simple index for predicting the susceptibility to solidification cracking, Weld. J. 94 (2015) 374s-388s.

[159] G. Tang, B.J. Gould, A. Ngowe, A.D. Rollett, An Updated Index Including Toughness for Hot-Cracking Susceptibility, Metall. Mater. Trans. A Phys. Metall. Mater. Sci. 53 (2022) 1486–1498. doi:10.1007/s11661-022-06612-6.

[160] M. Tang, P.C. Pistorius, S. Narra, J.L. Beuth, Rapid Solidification: Selective Laser Melting of AlSi10Mg, JOM. 68 (2016) 960–966. doi:10.1007/s11837-015-1763-3.

[161] U. Scipioni Bertoli, G. Guss, S. Wu, M.J. Matthews, J.M. Schoenung, In-situ characterization of laser-powder interaction and cooling rates through high-speed imaging of powder bed fusion additive manufacturing, Mater. Des. 135 (2017) 385–396. doi:10.1016/j.matdes.2017.09.044.

[162] M.C. Flemings, Solidification processing, Metall. Trans. 5 (1974) 2121–2134. doi:10.1007/BF02643923.

[163] T.J. Watt, E.M. Taleff, F. Lopez, J. Beaman, R. Williamson, Solidification Mapping of a Nickel Alloy 718 Laboratory VAR Ingot, Proc. 2013 Int. Symp. Liq. Met. Process. Cast. (2016) 261–270. doi:10.1007/978-3-319-48102-9_38.

[164] J.W. Elmer, The Influence Of Cooling Rate On The Microstructure Of Stainless Steel Alloys, 1989.

[165] D.J. Thoma, C. Charbon, G.K. Lewis, R.B. Nemec, Directed light fabrication of iron-based materials, Mater. Res. Soc. Symp. - Proc. 397 (1996) 341–346.

[166] J.W. Elmer, S.M. Allen, T.W. Eagar, Microstructural development during solidification of stainless steel alloys, Metall. Trans. A. 20 (1989) 2117–2131. doi:10.1007/BF02650298.

[167] G.E. Dieter, Mechanical metallurgy, 1986. doi:10.1016/s0016-0032(62)91145-6.

[168] S.J. Raab, R. Guschlbauer, M.A. Lodes, C. Körner, Thermal and Electrical Conductivity of 99.9% Pure Copper Processed via Selective Electron Beam Melting, Adv. Eng. Mater. 18 (2016) 1661–1666. doi:10.1002/adem.201600078.

[169] M. Higashi, T. Ozaki, Selective laser melting of pure molybdenum: Evolution of defect and crystallographic texture with process parameters, Mater. Des. 191 (2020) 108588. doi:10.1016/j.matdes.2020.108588.

[170] B. Dovgyy, A. Piglione, P. Hooper, M.-S. Pham, Comprehensive assessment of the printability of CoNiCrFeMn in Laser Powder Bed Fusion, Mater. Des. 194 (2020) 108845. doi:10.1016/j.matdes.2020.108845.

[171] C. Tan, K. Zhou, W. Ma, B. Attard, P. Zhang, T. Kuang, Selective laser melting of high-performance pure tungsten: parameter design, densification behavior and mechanical properties, Sci. Technol. Adv. Mater. 19 (2018) 370–380. doi:10.1080/14686996.2018.1455154.

[172] L.E. Rännar, A. Koptyug, J. Olsén, K. Saeidi, Z. Shen, Hierarchical structures of stainless steel 316L manufactured by Electron Beam Melting, Addit. Manuf. 17 (2017) 106–112. doi:10.1016/j.addma.2017.07.003.

[173] R. Pokharel, L. Balogh, D.W. Brown, B. Clausen, G.T. Gray, V. Livescu, S.C. Vogel, S. Takajo, Signatures of the unique microstructure of additively manufactured steel observed via diffraction, Scr. Mater. 155 (2018) 16–20. doi:10.1016/j.scriptamat.2018.06.008.

[174] A.T. Polonsky, W.C. Lenthe, M.P. Echlin, V. Livescu, G.T. Gray, T.M. Pollock, Solidification-driven Orientation Gradients in Additively Manufactured Stainless Steel, Acta Mater. 183 (2019) 249–260. doi:10.1016/j.actamat.2019.10.047.

[175] C.A. Bronkhorst, J.R. Mayeur, V. Livescu, R. Pokharel, D.W. Brown, G.T. Gray, Structural representation of additively manufactured 316L austenitic stainless steel, Int. J. Plast. 118 (2019) 70–86. doi:10.1016/j.ijplas.2019.01.012.

[176] M. Laleh, A.E. Hughes, M.Y. Tan, G.S. Rohrer, S. Primig, N. Haghdadi, Grain boundary character distribution in an additively manufactured austenitic stainless steel, Scr. Mater. 192 (2021) 115–119. doi:10.1016/j.scriptamat.2020.10.018.

[177] P. Agrawal, S. Thapliyal, S.S. Nene, R.S. Mishra, B.A. McWilliams, K.C. Cho, Excellent strength-ductility synergy in metastable high entropy alloy by laser powder bed additive manufacturing, Addit. Manuf. 32 (2020) 101098. doi:10.1016/j.addma.2020.101098.

[178] Z. Zhu, W. Li, Q.B. Nguyen, X. An, W. Lu, Z. Li, F.L. Ng, S.M. Ling Nai, J. Wei, Enhanced strength–ductility synergy and transformation-induced plasticity of the selective laser melting fabricated 304 L stainless steel, Addit. Manuf. 35 (2020) 101300. doi:10.1016/j.addma.2020.101300.

[179] Y. Zhong, L. Liu, S. Wikman, D. Cui, Z. Shen, Intragranular cellular segregation network structure strengthening 316L stainless steel prepared by selective laser melting, J. Nucl. Mater. 470 (2016) 170–178. doi:10.1016/j.jnucmat.2015.12.034.

[180] T. Voisin, J. Forien, A. Perron, S. Aubry, N. Bertin, A. Samanta, A. Baker, Y.M. Wang, New insights on cellular structures strengthening mechanisms and thermal stability of an austenitic stainless steel fabricated by laser powder-bed-fusion, Acta Mater. 203 (2021) 116476. doi:10.1016/j.actamat.2020.11.018.

[181] J.M. Kim, H.H. Jin, J. Kwon, S.H. Kang, B.S. Lee, Effects of cellular segregation for high strength and ductility of additively manufactured 304L stainless steel, Mater. Charact. 194 (2022) 112364. doi:10.1016/j.matchar.2022.112364.

[182] M. He, H. Cao, Q. Liu, J. Yi, Y. Ni, S. Wang, Evolution of dislocation cellular pattern in Inconel 718 alloy fabricated by laser powder-bed fusion, Addit. Manuf. 55 (2022) 102839. doi:10.1016/j.addma.2022.102839.

[183] L. Cui, F. Jiang, D. Deng, T. Xin, X. Sun, R.T. Mousavian, R.L. Peng, Z. Yang, J. Moverare, Cyclic response of additive manufactured 316L stainless steel: The role of cell structures, Scr. Mater. 205 (2021) 114190. doi:10.1016/j.scriptamat.2021.114190.

[184] A.J. Birnbaum, J.C. Steuben, E.J. Barrick, A.P. Iliopoulos, J.G. Michopoulos, Intrinsic strain aging, Σ3 boundaries, and origins of cellular substructure in additively manufactured 316L, Addit. Manuf. 29 (2019) 100784. doi:10.1016/j.addma.2019.100784.

[185] B. Barkia, P. Aubry, P. HAGHI-Ashtiani, T. Auger, L. Gosmain, F. Schuster, H. Maskrot, On the origin of the high tensile strength and ductility of additively manufactured 316L stainless steel: multiscale investigation, J. Mater. Sci. Technol. 41 (2019) 209–218. doi:10.1016/j.jmst.2019.09.017.

[186] Z. Sun, X. Tan, S.B. Tor, C.K. Chua, Simultaneously enhanced strength and ductility for 3D-printed stainless steel 316L by selective laser melting, NPG Asia Mater. 10 (2018) 127–136. doi:10.1038/s41427-018-0018-5.

[187] A. Charmi, R. Falkenberg, L. Ávila, G. Mohr, K. Sommer, A. Ulbricht, M. Sprengel, R. Saliwan Neumann, B. Skrotzki, A. Evans, Mechanical anisotropy of additively manufactured stainless steel 316L: An experimental and numerical study, Mater. Sci. Eng. A. 799 (2021) 140154. doi:10.1016/j.msea.2020.140154.

[188] S. Bahl, S. Mishra, K.U. Yazar, I.R. Kola, K. Chatterjee, S. Suwas, Non-equilibrium microstructure, crystallographic texture and morphological texture synergistically result in unusual mechanical properties of 3D printed 316L stainless steel, Addit. Manuf. 28 (2019) 65–77. doi:10.1016/j.addma.2019.04.016.

[189] Qu, Li, F. Zhang, JiamingBai, Anisotropic cellular structure and texture microstructure of 316L stainless steel fabricated by selective laser melting via rotation scanning strategy, Mater. Des. 215 (2022) 110454. doi:10.1016/j.matdes.2022.110454.

[190] T. Niendorf, S. Leuders, A. Riemer, H.A. Richard, T. Tröster, D. Schwarze, Highly anisotropic steel processed by selective laser melting, Metall. Mater. Trans. B Process Metall. Mater. Process. Sci. 44 (2013) 794–796. doi:10.1007/s11663-013-9875-z.

[191] X. Wang, J.A. Muñiz-Lerma, M. Attarian Shandiz, O. Sanchez-Mata, M. Brochu, Crystallographic-orientation-dependent tensile behaviours of stainless steel 316L fabricated by laser powder bed fusion, Mater. Sci. Eng. A. 766 (2019) 138395. doi:10.1016/j.msea.2019.138395.

[192] M. Calandri, S. Yin, B. Aldwell, F. Calignano, R. Lupoi, D. Ugues, Texture and microstructural features at different length scales in Inconel 718 produced by selective laser melting, Materials (Basel). 12 (2019) 1293. doi:10.3390/ma12081293.

[193] W. Kurz, Solidification microstructure-processing maps: Theory and application, Adv. Eng. Mater. 3 (2001) 443–452. doi:10.1002/1527-2648(200107)3:7<443::AID-ADEM443>3.0.CO;2-W.

[194] E. Strumza, O. Yeheskel, S. Hayun, The effect of texture on the anisotropy of thermophysical properties of additively manufactured AlSi10Mg, Addit. Manuf. 29 (2019) 100762. doi:10.1016/j.addma.2019.06.013.

[195] V. Manvatkar, A. De, T. DebRoy, Spatial variation of melt pool geometry, peak temperature and solidification parameters during laser assisted additive manufacturing process, Mater. Sci. Technol. (United Kingdom). 31 (2015) 924–930. doi:10.1179/1743284714Y.0000000701.

[196] Z. Li, T. Voisin, J.T. McKeown, J. Ye, T. Braun, C. Kamath, W.E. King, Y.M. Wang, Tensile properties, strain rate sensitivity, and activation volume of additively manufactured

316L stainless steels, Int. J. Plast. 120 (2019) 395–410. doi:10.1016/j.ijplas.2019.05.009.

[197] K. Koube, G. Kennedy, K. Bertsch, J. Kacher, D.J. Thoma, N.N. Thadhani, Spall Damage Mechanisms in Laser Powder Bed Fabricated Stainless Steel 316l, SSRN Electron. J. 851 (2022) 143622. doi:10.2139/ssrn.4098760.

[198] G.T. Gray, V. Livescu, P.A. Rigg, C.P. Trujillo, C.M. Cady, S.R. Chen, J.S. Carpenter, T.J. Lienert, S.J. Fensin, Structure/property (constitutive and spallation response) of additively manufactured 316L stainless steel, Acta Mater. 138 (2017) 140–149. doi:10.1016/j.actamat.2017.07.045.

[199] G.T. Gray, V. Livescu, P.A. Rigg, C.P. Trujillo, C.M. Cady, S.R. Chen, J.S. Carpenter, T.J. Lienert, S.J. Fensin, Structure/property (constitutive and spallation response) of additively manufactured 316L stainless steel, Acta Mater. 138 (2017) 140–149. doi:10.1016/j.actamat.2017.07.045.

[200] S.J. Fensin, J.P. Escobedo-Diaz, C. Brandl, E.K. Cerreta, G.T. Gray, T.C. Germann, S.M. Valone, Effect of loading direction on grain boundary failure under shock loading, Acta Mater. 64 (2014) 113–122. doi:10.1016/j.actamat.2013.11.026.

[201] S.J. Fensin, S.M. Valone, E.K. Cerreta, G.T. Gray, Influence of grain boundary properties on spall strength: Grain boundary energy and excess volume, J. Appl. Phys. 112 (2012). doi:10.1063/1.4761816.

[202] G.A. Knorovsky, M.J. Cieslak, T.J. Headley, A.D. Romig, W.F. Hammetter, INCONEL 718: A solidification diagram, Metall. Trans. A. 20 (1989) 2149–2158. doi:10.1007/BF02650300.

[203] R. Jiang, A. Mostafaei, J. Pauza, C. Kantzos, A.D. Rollett, Varied heat treatments and properties of laser powder bed printed Inconel 718, Mater. Sci. Eng. A. 755 (2019) 170–180. doi:10.1016/j.msea.2019.03.103.

[204] L.L. Parimi, G. Ravi, D. Clark, M.M. Attallah, Microstructural and texture development in direct laser fabricated IN718, Mater. Charact. 89 (2014) 102–111. doi:10.1016/j.matchar.2013.12.012.

[205] P. Nie, O.A. Ojo, Z. Li, Numerical modeling of microstructure evolution during laser additive manufacturing of a nickel-based superalloy, Acta Mater. 77 (2014) 85–95. doi:10.1016/j.actamat.2014.05.039.

[206] F. Liu, F. Lyu, F. Liu, X. Lin, C. Huang, Laves phase control of inconel 718 superalloy fabricated by laser direct energy deposition via δ aging and solution treatment, J. Mater. Res. Technol. 9 (2020) 9753–9765. doi:10.1016/j.jmrt.2020.06.061.

Appendix 1: Tensile and fatigue samples

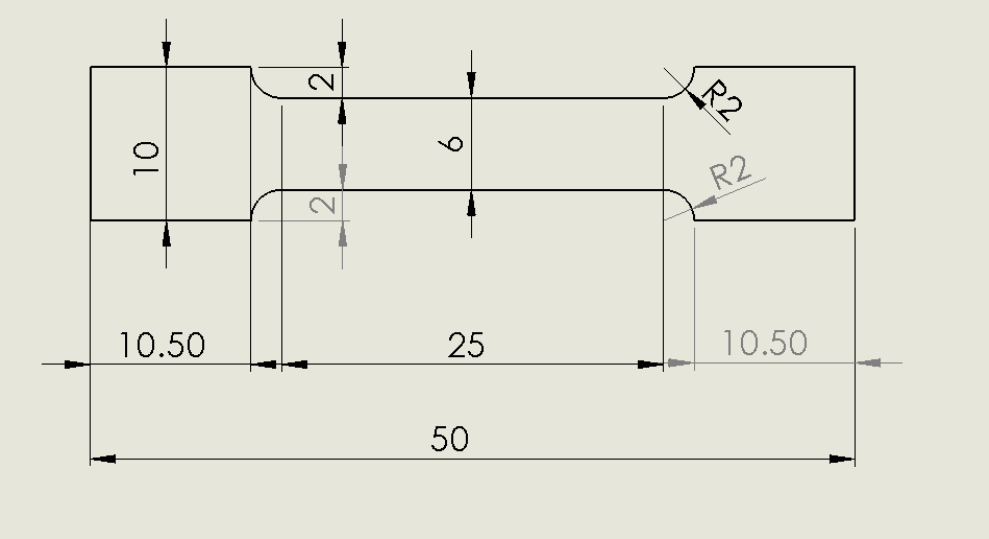

Figure 39. Schematic drawing of flat dog bone shape tensile specimens.

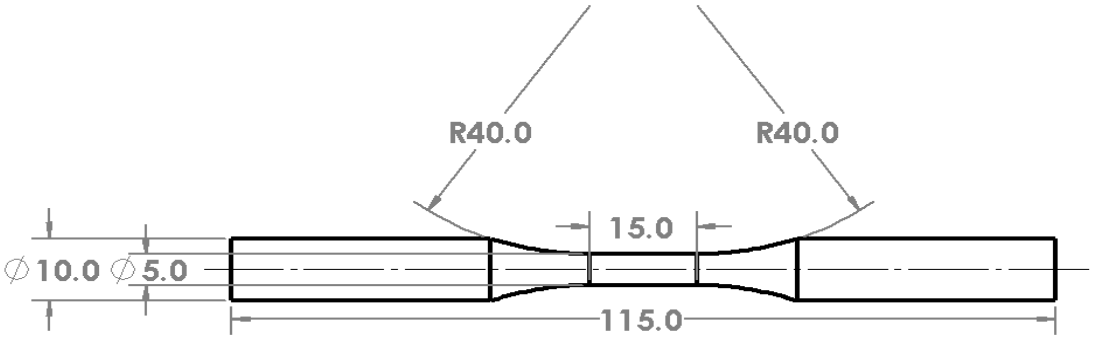

Figure 40. Schematic drawing of cylindrical dog bone shape fatigue specimens.

Appendix 2: Grain size measurements

1) EBSD Mapping (with area size of 1mm x 1 mm and step size = 1 microns) to ensure enough grains indexing for statistical averaging.
2) Grain boundaries (having a misorientation greater than 5 degrees) were mapped.

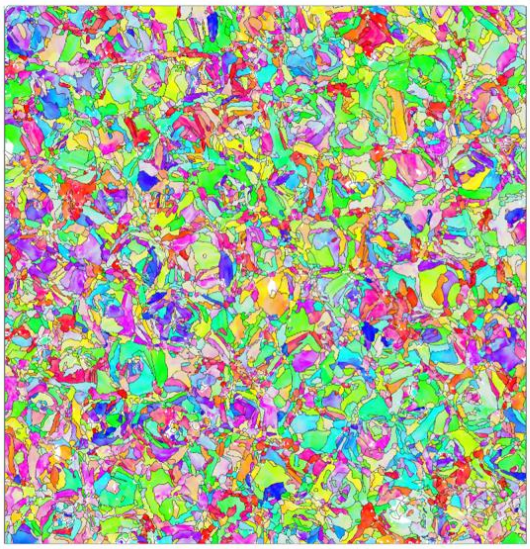

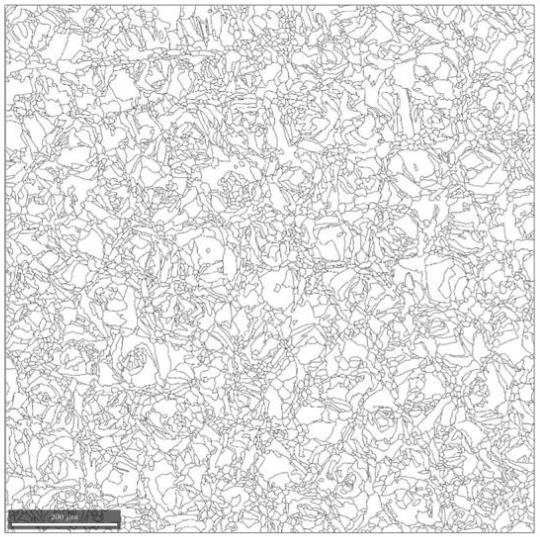

3) Set the minimum grain size criteria and all the grains with area <20 μm^2 was removed from the analysis (As per ASTM E2627). For example, in the zoomed area → grains of 10 pixels or less inside the bigger grains can be observed (which are due to experimental).

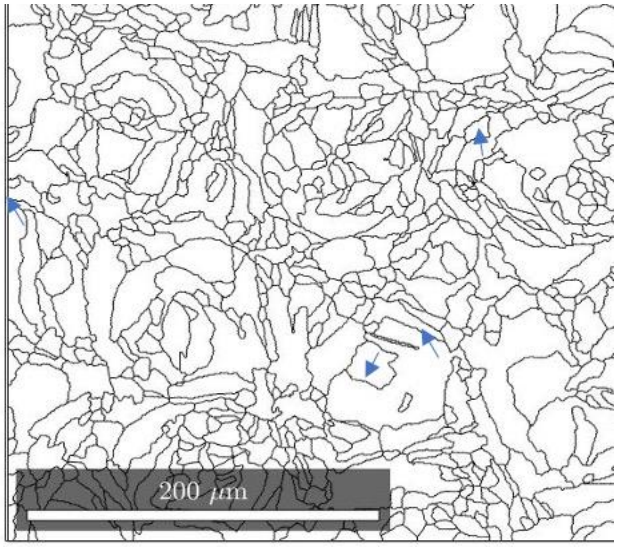

4) The grain size was calculated by measuring the largest distance (in pixels) within each grain and converting the pixels into microns. Non-weighted number average provided the average grain size value.